CONVERSION OF SHALE GAS WITH SUPPORTED METAL CATALYSTS

A Dissertation

Submitted to the Faculty

of

Purdue University

by

Johnny Zhuchen

In Partial Fulfillment of the

Requirements for the Degree

of

Doctor of Philosophy

August 2020

Purdue University

West Lafayette, Indiana

THE PURDUE UNIVERSITY GRADUATE SCHOOL
STATEMENT OF DISSERTATION APPROVAL

Dr. Jeffrey T. Miller, Chair

Davidson School of Chemical Engineering

Dr. Jeffrey Greeley

Davidson School of Chemical Engineering

Dr. Abhaya K. Datye

Department of Chemical and Biological Engineering, University of New Mexico

Michael Harris

Davidson School of Chemical Engineering

Approved by:

Dr. John Morgan

Head of the School Graduate Program

For my Family

ACKNOWLEDGMENTS

My Ph.D. experience has been such an amazing experience, in which I have learned so many skills and meet so many great people. I would like to thank these people who have helped and supported me during these four years.

First of all, I would like to express my sincere gratitude to my advisor, Professor Jeffrey Miller, for his guidance and support throughout my graduate school. He helped me analyzing experimental data in person and guided me with lots of his own research experience. He not only taught me the technical details in catalysis, but also the approaches to research. He was always thinking about how to help me in the technical writing and presentations, which helped me improve a lot as a researcher. He also provided me with lots of academic connections, which is very helpful for my career development. I still remember when he went through each slide with me for the preparation of the qualify exam. Jeff also cares about my life after grad school and helped me making plans after graduation.

I also would like to acknowledge the colleagues who have provided so much of help during my time at Purdue and contributed to my dissertation. I have been fortunate to work with Dr. Guanghui Zhang for two years. His chemistry knowledge has enormously helped me think critically about material structures. Moreover, he taught me X-ray absorption spectroscopy analysis and academic writing. I am also thankful for the working experience with Nicole Libretto. She has always been willing to discuss about research and teaching me about lab equipments. I also would like to thank Abhijit Talpade and Griffin Canning for the collaboration on the Pt/CeO_2 project. Xin Yang made major contribution on the Pt-Ti/SiO_2 and Jiajing Kou lead the Pt-P/SiO_2 project.

I would also like to thank all other Miller group members: Dr. Zhenwei Wu, Dr. Evan Wegener, Dr. Stephen Purdy, Dr. Laryssa Cesar, Seulgi Choi, Matthew Conrad,

Junxian Gao, Rui Ma, Xianli Wu,Chunlei Peng, Christopher Russell, Che-Wei Chang, Wenqing Zhang, Christian Breckner and David Dean. I would also like to acknowledge the others who have played major roles in the works outline in this dissertation: Paige Probus, Dr. Yang Ren, Dr. Jeremy Kropf, Dr. Dmitry Zemlyanov, Dr. James Harris, Dr. Jeffrey Greeley, Dr. Fabio Ribeiro, Dr. Christina Li, Dr. Yang Xiao, Dr. Arvind Varma, Dr. Abhaya Datye, Dr. Wei Liu and Xiaoben Zhang.

Finally, I would like to acknowledge my friends and family who have been so supportive throughout my Ph.D. career. I have met so many great people in Purdue University, who have helped me adapt the life in the US. Thank you to my family, especially my parents for supporting me throughout my life.

TABLE OF CONTENTS

Page

Page

Page

Page

LIST OF TABLES

LIST OF FIGURES

Figure Page

Figure Page

Figure Page

ABSTRACT

Zhuchen, Johnny Ph.D., Purdue University, August 2020. Conversion of Shale Gas with Supported Metal Catalysts. Major Professor: Jeffrey T. Miller.

As shale gas exploitation has been developed, production of shale gas in the US has rapidly increased during the last decade. This has motivated the development of techniques to covert shale gas components (mainly C_1 to C_3) to liquid fuels by catalytic conversion. The main goal of the dissertation is to study the geometric and electronic structures of the metal catalysts, which are crucial for understanding the structure-property relationship.

The first project studies bimetallic Pt-Bi catalyst for non-oxidative coupling of methane. In a recent publication published in ACS catalysis, Pt-Bi/ZSM-5 catalyst has been shown to stably convert methane into C_2 for 8 hours under non-oxidative conditions. In this manuscript, structure of the Pt-Bi/ZSM-5 was shown with HAADF imaging, synchrotron XAS and XRD. A new surface cubic Pt_3Bi phase on Pt nanoparticles with Pt-Bi bond distance of 2.80 Å was formed. Formation of noble metal intermetallic alloys such as Pt_3M may be the clue for non-oxidative conversion of methane.

The second and third project highlight strong metal-support interaction catalysts for propane dehydrogenation. Chemisorption showed partial coverage of the SMSI oxides on the surface of the nanoparticles. *In situ* X-ray absorption near edge (XANES), resonant inelastic X-ray scattering (RIXS), X-ray photoelectron spectroscopy (XPS) have shown that little electronic effect on the metal nanoparticles. The catalyst activity per mol of metal decreased due to the partial coverage of the SMSI oxides on the surface of the catalysts. The catalysts, however, had higher selectivity due to smaller ensembles inhibiting hydrogenolysis.

In the fourth project Pt-P catalyst was investigated to understand the promoting effect of P.Pt-P catalysts had much higher selectivity for propane dehydrogenation (>95%). These give two types of catalysts, a PtP_2-rich surface on Pt core and full PtP_2 ordered structure, which were confirmed by scanning transmission electron microscopy (STEM), and *in situ* methods of EXAFS, synchrotron XRD, XPS, and Resonant Inelastic X-ray Spectroscopy (RIXS). The PtP_2 structure has isolated Pt atoms separated by P_2 atoms. In addition XANES, XPS and RIXS indicate a strong electronic modification in the energy of the valence orbitals.

It can be concluded from the Pt-Bi catalyst that intermetallic alloys might be selective for NOCM. Therefore, promoters with higher reduction temperature, such as Mn and Cr, should be used to have stable catalysts at high temperature. Moreover, both Pt-Bi and Pt/CeO_2 suggest that selective catalysts for propane dehydrogenation and NOCM may have some correlation. Further studies would be conducted to understand the correlation between the two reactions.

1. INTRODUCTION

1.1 Shale gas revolution

Shale gas has been widely exploited in the United States, and catalytic conversion of shale gas has received increasing attention in the past decade. [1,2] Figure 1.1 shows the rapid increase of the shale gas production in the United States. [3] Shale gas is a type of unconventional natural gas from shale deposits. Various different types of techniques including horizontal drilling microseismic monitoring have been applied for the exploitation of shale gas. Main components of shale gas include methane, ethane and propane. [4]

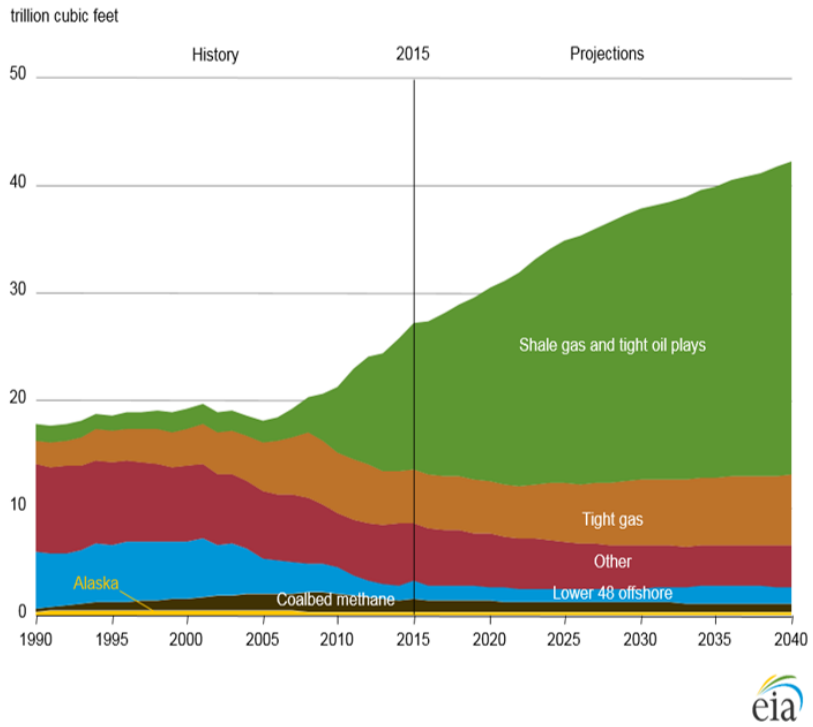

Fig. 1.1. US dry natural gas production by type

Recently, lots of research has been conducted in both industry and academia. [3, 5] Shale gas is mainly distributed in remote locations (Figure 1.2), therefore it is preferred to convert shale gas into liquid fuels on site. An engineering research center named Innovative and Strategic Transformation of Alkane Resources (CISTAR) was recently funded by the National Science Foundation for this purpose. The main strategy of CISTAR is to convert methane into C_2 hydrocarbons and dehydronate light alkanes in the first step, and converting the olefins by oligomarization to fuel products. This thesis work is conducted mainly under the CISTAR research center and focuses on non-oxidative coupling of methane and propane dehydrogenation.

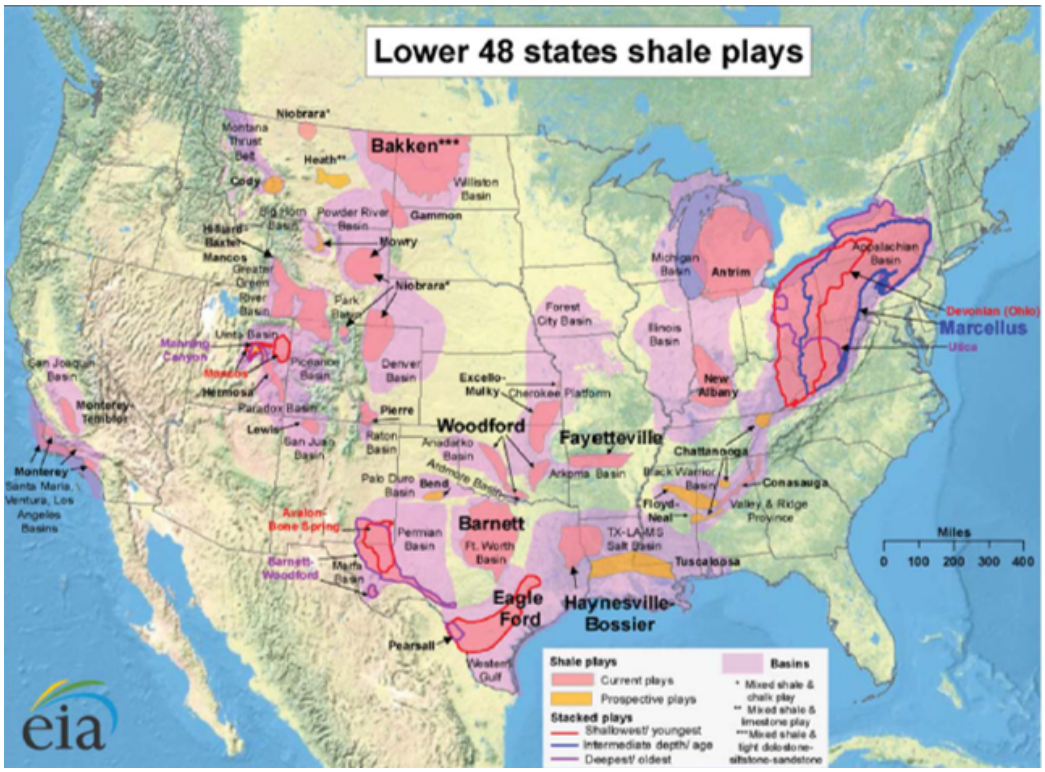

Fig. 1.2. US dry natural gas production by type

1.2 Methane conversion

1.2.1 Overview

Methane is a stable molecule with a high C-H bond strength (434 kJ/ mol) [6]. High temperature (e.g. 900-1000 K) are required for breaking C-H bond. Additionally, in order to make high molecular weight molecules, C-C bonds should be made. Therefore, it is challenging to activate and convert methane into higher value chemicals [7].

One option to convert methane into ethane and ethylene is oxidative methane coupling (OCM), for which alkaline earth metal oxides and rare earth metal oxides have been mainly utilized [8–10]. The OCM reaction, however, often leads to overoxidation to produce CO and CO2 giving low selectivity toward ethane and ethylene [9]. Ethane and ethylene are important industrial intermediate products and can be further converted to large molecules by, for example, oligomerization. A commercial process for ethylene oligomerization is an industrial process was developed by Shell [11].

Conversion of methane under non-oxidative conditions could potentially have high selectivity towards ethane and ethylene and has recently been studied by Gerceker et al. over PtSn catalysts [11]. The conversion, however, was lower than 0.3%. The main limitation of the reaction is the thermodynamic equilibrium. As reaction is endothermic, the equilibrium conversion becomes higher with increasing temperature. At 1250 K, the thermodynamic equilibrium is 30% to ethane. High temperature, however, leads to greater coke deposition and low catalyst stability. Thus, developing a catalyst with high selectivity towards target products and relatively high methane conversion is important, since the main energy consumption in the chemical industry is for separation. If high selectivity towards target product is reached, energy consumption for the process would be significantly reduced. Therefore, the first goal of the research is to:

1. Develop a catalyst to convert methane with high C_2 selectivity (e.g. ethane, ethylene)

On the other hand, methane conversion under non-oxidative conditions to ethane, ethylene and aromatics has also been investigated but is less well known. Since Wang et al. in 1993 [12] reported 7.2% conversion over Mo/ZSM-5 forming benzene, Mo/ZSM-5 has been widely studied for methane dehydroaromatization. The reaction, however, has a high coke selectivity (50%) at ca. 973 K [13]. Coke production also leads to catalyst deactivation [14]. It was shown that the main reason for coke deposit was the formation of a carbonaceous layer at the external zeolite surface, which decreased the accessibility of Brønsted acid sites in the micropores [14]. Therefore, the second goal of the research is to:

2. Develop a catalyst with low coke formation and high stability

1.2.2 Conversion of methane over Mo/ZSM-5 catalyst

As mentioned above, Mo/ZSM-5 has been the most effective catalyst for methane dehydroaromatization reaction. The methane conversion at 700 C during the initial period is 6-15% [15,16]. The selectivity to benzene is 60-85%. It has been shown that Mo loaded on different supports can change the product distribution [16,17]. Fig.1.3 shows various distributions of hydrocarbon products with Mo loaded on different supports. It was shown that Mo/HSZM-5 has the highest benzene selectivity among all the products.

Several different mechanisms were proposed for the methane dehydroaromatization reaction. Most studies agree with the bifunctional mechanism [14, 15], which involves two different active sites: MoC_x or MoC_xO_y and Brønsted acid sites. Molybdenum carbide or oxycarbide activates C-H bond in methane and converts it into ethylene as an intermediate product. Then ethylene is oligomerized into benzene and other aromatic products on Brønsted acid sites within the ZSM-5 micropores [18]. There is still a debate about the mechanism, and other bifunctional mechanisms [19] and monofunctional mechanisms have also been proposed [17].

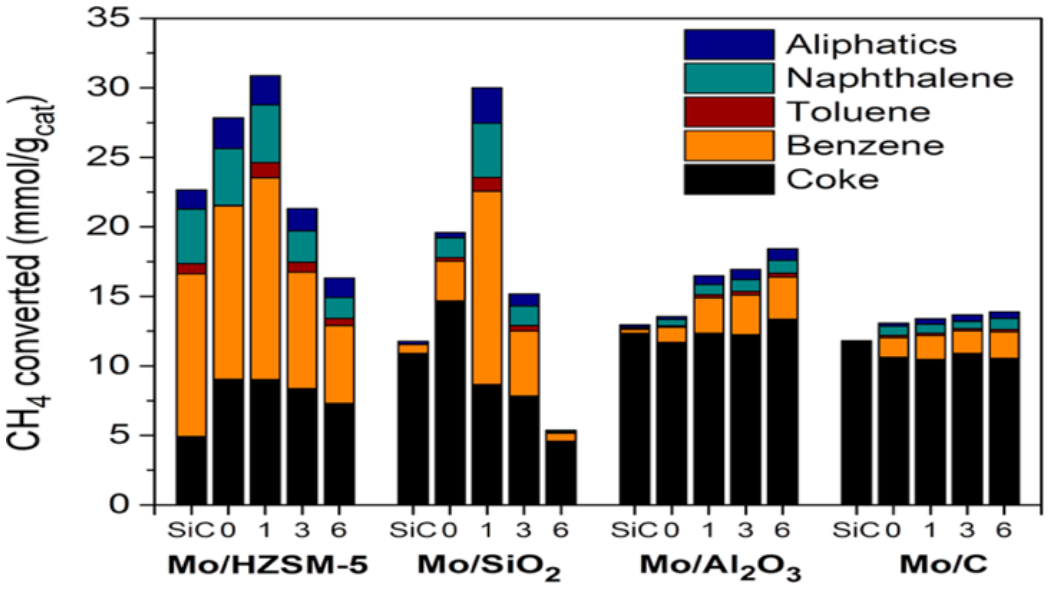

Fig. 1.3. Distribution of hydrocarbon products and coke obtained after 16 h MDA runs. Conditions: 700 °C, atmospheric pressure, 0.3 g of catalyst mixture (1:1), WHSV 2.0 h^1, 16 h.

One of the most important problems for this reaction is catalyst stability. The poor catalyst stability is caused by the coke formation. It has been shown that the average coke selectivity was 30% for Mo/ZSM-5 at 973 K [13]. Promoters such as W [20], Ru [21], Pt [22], In [13], Fe [23], Zn [24] have been shown to lower coke selectivity. Despite research done on reducing the coke formation, catalyst stability still remains poor.

1.2.3 High selectivity to C_2 with Pt-based catalyst

Conversion of methane over Pt catalyst under non-oxidative conditions

Belgued et al. [25] used a commercial Pt/SiO_2 catalyst (EUROPLOT-1) to convert methane into hydrocarbons. As reported in their work, Fig. 1.4 shows the Pt/SiO_2 catalyst converted methane into ethane under non-oxidative conditions. The stability, however, was poor. The ethane yield reached maximum at 2 min and deactivated

within 10 min. The hydrogen production was an order of ethane, suggesting that the carbonaceous residues were accumulated on the Pt surface and eventually converted into a carbon film leading to the deactivation of the catalyst.

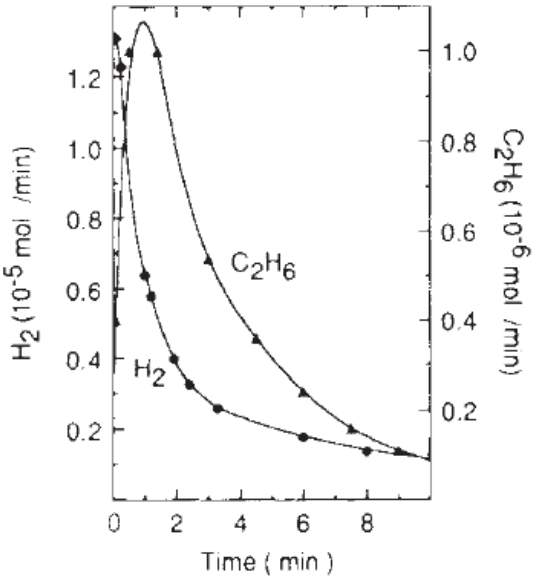

Fig. 1.4. Molar flow rates of H_2 and C_2H_6 for CH_4 methane conversion on EUROPT-1 catalyst. Flow rate of CH_4: 400 ml/min under ordinary pressure, 250°C

Vines et al. [26] conducted DFT calculations for dehydrogenation of methane over Pt catalyst. The energy barriers over Pt (111) surface to form CH3, CH2 and CH are ca. 90 kJ/mol, 72 kJ/mol and 16 kJ/mol respectively, which are not difficult to overcome at high temperatures (¿800 K). For the $Pt_7$9 model, energy barriers are lower than Pt (111) and the formation of CH_3, CH_2 and CH is even more exothermic. Therefore, it is concluded that activating methane is not the biggest obstacle over noble metals (e.g. Pt), but the desorption of carbon species on the surface is.

Conversion of methane with Pt-based bimetallic catalysts under non-oxidative conditions

Gerceker et al. [11] recently reported that addition of Sn to Pt/SiO_2 could improve activity of the catalyst forming more ethylene. In addition, PtSn catalyst over ZSM-5 showed higher ethylene selectivity than on SiO_2. The selectivity could reach over 90%, while the highest conversion was only 0.30% even for the best catalyst, PtSn (1:2)/ZSM-5 (SiO_2:Al_2O_3=50).

Xiao and Varma [27] found that methane could deoxygenate guaiacol over a Pt-Bi bimetallic catalyst. When using methane as a substitute for H_2 to deoxygenate guaiacol, one of the main products was ethane. They suggested that there could be two possible pathways for the formation of ethane. The first pathway is that methane decomposes over Pt and contributes one H atom for guaiacol deoxygenation, while the residual methyl combines with another methyl, forming ethane. The second pathway is same as the first one except that a methyl from methane combines with a methyl from guaiacol. The first pathway is similar to non-oxidative methane coupling, suggesting that Pt and Pt-Bi catalysts could be active for the non-oxidative methane coupling reaction. Pt, however, was unstable for guaiacol deoxygenation. Better stability was obtained by adding a Bi promotor, although the conversion was slightly lower [27]. Based on these results we hypothesize the Pt-Bi on HZSM-5 could convert methane under non-oxidative conditions to C_2^+ hydrocarbons.

1.3 Propane Dehydrogenation

Propylene serves as a key basic feedstock for the manufacture of various products such as polypropylene, propylene oxide, and acrylonitrile. [28, 29]Because of the growing demand for propylene and the vast amount of propane in shale gas deposits, propane dehydrogenation (PDH) becomes increasingly important as a propylene on-purpose production technology. Since C-H bond cleavage is thermodynamically limited and highly endothermic, PDH requires high temperature reaction condition (550-

750 °C), which is also optimal condition for the hydrogenolysis reaction and formation of coke. [5, 30–32] Fortunately, these pathways in PDH process happen over distinct active sites, which means that high olefin yields can be obtained by careful catalyst design. Bimetallic nanoparticle (NP) catalysts can offer an effortless approach to fine-tune surface properties and catalytic selectivity via simply altering the components of the surface. Take Pt as an example, which is considered to be the champion metal in PDH due to its superior activation of paraffinic C-H bonds. [33] Despite the fact that supported Pt catalysts display very high activity, their intrinsic selectivity to alkenes and catalyst stability are not entirely satisfactory. Promoter addition, affording bimetallic and/or alloying systems such as Pt-Sn, Pt-Cr, Pt-Ga, Pt-Cu, and Pt-Co, [34–38] has been found to be one of the most effective strategy in improving alkene selectivity and suppressing coke formation by increasing Pt dispersion or diluting Pt ensembles, and changing the electronic environment of Pt atoms. [39–42]

1.4 Thesis Overview

The goal of the thesis is the better use of shale gas resources.For conversion of methane, non-oxidative of methane is a feasible direct way to convert methane on site to C_2 hydrocarbons allowing further conversion to fuels or chemicals.Light alkane dehydrogenation is also a promising first step of new processes coupling other chemical conversion steps.

Chapter two presents the studies of Pt-Bi bimetallic catalysts for non-oxidative coupling of methane. In this work, we synthesized 2-3 nm metal nanoparticles on silica.The nanoparticles' structure were determined by STEM imaging, synchrotron XRD and XAS, and the surface structure was further confirmed by the probe reaction, catalytic propane dehydrogenation. We propose a surface cubic Pt_3Bi phase, which is not known in the bulk composition, on Pt nanoparticles with Pt-Bi bond distance of 2.80 Å. This work highlights the understanding of the structure-property relationship of a surface layer of nanoparticle catalysts for non-oxidative coupling of methane, and

this understanding suggests that other noble metal intermetallic alloys such as Pt_3M may also be capable of non-oxidative conversion of methane.This work is published as "Structure Determination of Nanoscale Pt_3Bi Intermetallic Alloy Catalysts for Non-oxidative Coupling of Methane and Propane Dehydrogenation." and is reproduced here with permission.

Chapter three covers the studies on a series of strong metal-support interaction (SMSI) Pt-Ti and Pt-Nb catalysts.This study uses a variety of characterization techniques to demonstrate that there is little electronic effect while 80% of the surface Pt is covered by the SMSI oxides.The SMSI catalysts showed about 90% propylene selectivity for propane dehydrogenation, which is much higher than monometallic Pt, due to smaller surface Pt ensembles.

Chapter four introduces my work on Pt/CeO_2 for propane dehydrogenation. Previous work has shown that Pt is atomically dispersed within the CeO_2 lattice when Pt/CeO_2 is treated at 800 °C with air. [43, 44] Using *in situ* XAS and and TEM we have identified that after reduction at 975 °C, there is a SMSI oxide overlayer formed on the surface of the Pt nanoparticles. Catalytically, Pt/CeO_2 reduced at 550 °C displays similar catalysis as monometallic Pt; while rediction at 975 °C leads to high selectivity Pt nanoparticles, albeit with lower rates. The results suggest that for the SMSI Pt/CeO_2, the few exposed catalytic sites have smaller surface ensembles, suppressing hydrogenolysis (structure insensitive reaction) while keeping similar activity for dehydrogenation (structure sensitive reaction).

Chapter five contains a work by my colleagues and I (led by Jiajing Kou) on a Pt-P intermetallic catalysts compared to monometallic Pt nanoparticles.In this paper we describe two easily, scalable synthesis methods that give 2 nm PtP_2 NP's. These give two types of catalysts,a PtP_2-rich surface on Pt core and full PtP_2 ordered structure, which were confirmed by scanning transmission electron microscopy (STEM), and *in situ* methods of EXAFS, synchrotron XRD, XPS, and Resonant Inelastic X-ray Spectroscopy (RIXS). The PtP_2 structure has isolated Pt atoms separated by P_2 atoms. In addition XANES, XPS and RIXS indicate a strong electronic modification

in the energy of the valence orbitals. These changes leads to highly olefin selectivity, ca. $> 97\%$, propane dehydrogenation catalysts.

Chapter six is a summary and discussion about the scientific findings and findings for the thesis. The topics of interest are summarized here, discussing about: 1) intermetallic alloy catalysts for non-oxidative methane coupling and how to achieve high activity at high temperatures with alloys stable at high temperatures; 2) further understanding on SMSI coverage and the effects for propane dehydrogenation.

2. IDENTIFICATION OF THE STRUCTURE OF THE BI PROMOTED PT NON-OXIDATIVE COUPLING OF METHANE CATALYST: A NANOSCALE PT3BI INTERMETALLIC ALLOY

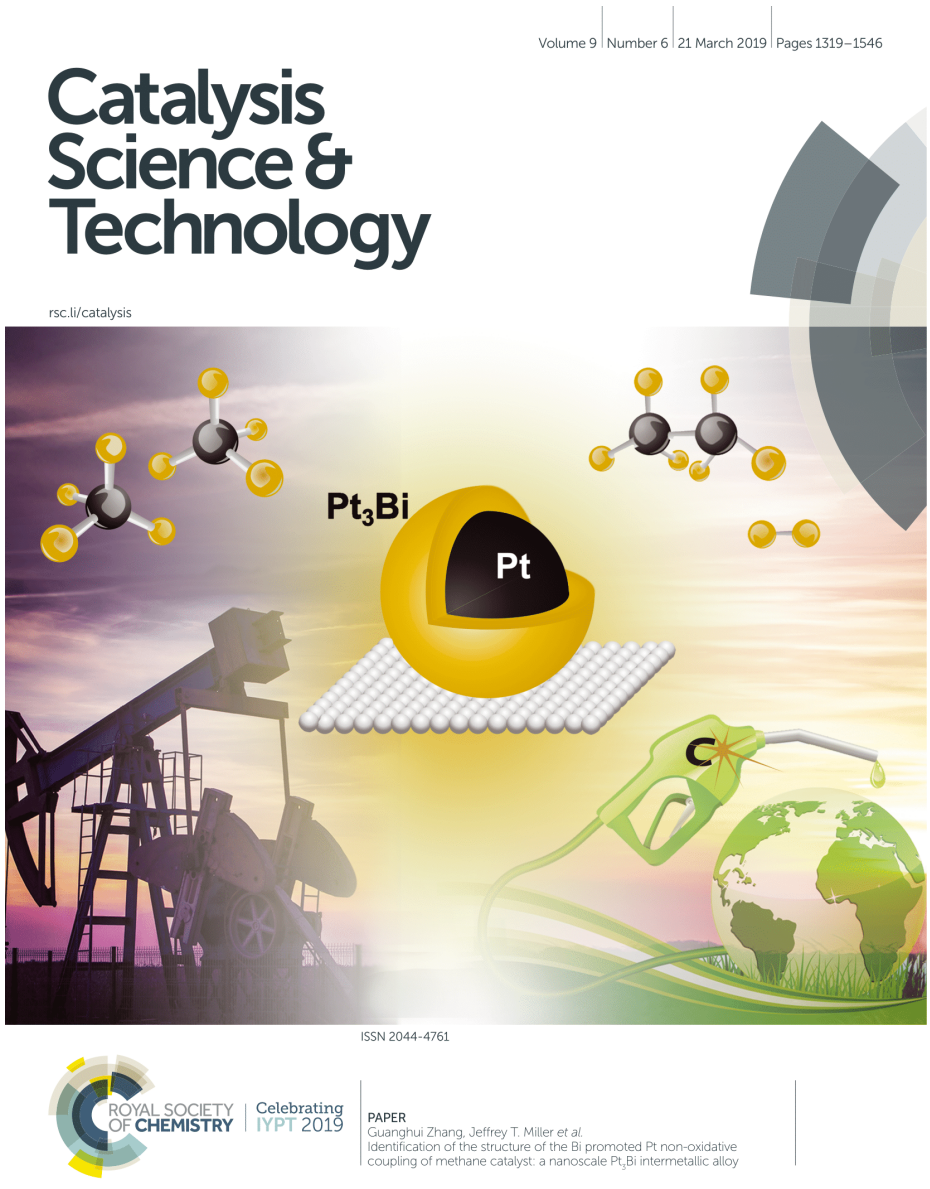

This chapter is reproduced from Zhu Chen, Johnny, et al." Structure Determination of Nanoscale Pt_3Bi Intermetallic Alloy Catalysts for Non-oxidative Coupling of Methane and Propane Dehydrogenation." Catalysis Science Technology 9 (2019): 1349-1356. by permission from The Royal Society of Chemistry. DOI:10.1039/C8CY02171F.

2.1 Abstract

Catalytic conversion of shale gas has received increasing attention in the past decade, and recently stable methane conversion with C_2 selectivity greater than 90% for up to 8 h has been reported over Pt-Bi/ZSM-5 at moderate temperatures (600-700°C). In this study we show that the structure of Pt-Bi/ZSM-5 catalyst is similar to Pt-Bi/SiO_2. EXAFS indicates the formation of Pt-rich bimetallic Pt-Bi nanoparticles with Pt-Bi bond distance of 2.80 Å. The XRD spectra (on SiO_2) are consistent with cubic, intermetallic surface Pt3Bi phase on a Pt core. The Pt_3Bi structure is not known in the thermodynamic phase diagram. In all catalysts, only a small fraction of Bi alloys with Pt. At high Bi loadings, excess Bi reduces at high temperature, covering the catalytic surface leading to a loss in activity. At lower Bi loadings with little excess Bi, the Pt_3Bi surface is effective for non-oxidative coupling of CH_4 (on ZSM-5) and propane dehydrogenation (on SiO_2).

2.2 Introduction

Shale gas has been widely exploited in the United States, and catalytic conversion of shale gas has received increasing attention in the past decade. [1,2] Methane is the major component of shale gas (¿70%) and natural gas (95%), [3] which is mainly used for electricity and power generation. Chemical utilization of methane is primarily for production of hydrogen and syngas ($CO+H_2$), which may be further converted to methanol, ammonia, etc. Direct conversion of methane to fuels and value-added chemicals holds promising potential as an alternative to production of these from petroleum. [45]

One option, which has been widely studied, is the oxidative coupling of methane (OCM) to ethane and ethylene that are important industrial intermediates for production of fuels and chemicals. [10, 46, 47] The OCM reaction, however, often leads to over-oxidation to CO and CO_2, giving low selectivity toward hydrocarbon products. [9] To avoid over-oxidation, non-oxidative conversion of methane has also been studied since Wang *et al.* reported 7.2% conversion of methane over Mo/ZSM-5 to benzene and other aromatics. [12, 17, 20, 48, 49] The reaction, however, has a high coke selectivity (50%), which blocks the zeolite pores and MoCx surface, leading to deactivation of the catalyst within a few hours. [50] Although Mo/ZSM-5 has been extensively studied, few other catalysts are known to catalyze non-oxidative coupling of methane (NOCM). Guo *et al.* showed that Fe embedded in silica matrix converts methane to ethylene and aromatics at 1363 K with sustained conversion as high as 50%. [51]

Pt catalysts have also been reported, but with limited success. Belgued *et al.* reported that Pt/SiO_2 could convert methane to ethane. [25] The lifetime, however, was approximately 10 minutes due to the rapid formation of coke. The selectivity to C_2 was also poor at about 20%. The catalyst lifetime was significantly improved to over 10 h with over 85% C_2 selectivity using a Pt-Sn catalyst. [11] The conversion, however, was lower than 0.3% with this catalyst. More recently Xiao and Varma reported stable methane conversion at 2% with C_2 selectivity greater than 90% for up to 8 h over Pt-Bi/ZSM-5 at moderate temperatures (600-700°C). [52] The optimum conversion was obtained with 0.8Bi-1Pt/ZSM-5; while with higher Bi loadings, there was little activity. Higher reaction temperatures also gave lower activity. The detailed structure of this catalyst, however, was not investigated. Determination of the catalyst structure and the role of Bi in promoting Pt are essential for understanding the structure-activity relationship and will provide useful guidance for rational design of improved NOCM catalysts.

Herein we report the characterization of the bimetallic Pt-Bi/ZSM-5 NOCM catalysts and similar $Pt\text{-}Bi/SiO_2$. The latter is also selective for propane dehydro-

genation. *In situ* X-ray absorption spectroscopy (XAS), *in situ* Fourier transform infrared (FTIR), high-angle annular dark field scanning transmission electron microscopy (HAADF-STEM), energy dispersive X-ray spectroscopy (EDS) and *in situ* synchrotron X-ray diffraction (XRD) were used to determine the structure of the bimetallic nanoparticles.

2.3 Experimental

2.3.1 Materials

Davisil 636 silica gel (99%), H2PtCl$_6$·6H$_2$O (99.9%), BiCl$_3$ (99.999%), Pt(NH$_3$)$_4$(NO$_3$)$_2$ (99.995%), Bi(NO$_3$)$_3$·5H$_2$O (99.999%) were purchased from Sigma-Aldrich and used without further purification. ZSM-5 (Si/Al=40) of ammonium form was from Zeolyst International. The gases used for the catalytic testing were purchased from Indiana Oxygen Company, and the C3H8 is 5% balanced with N_2. The H_2 was also 5% balanced with N_2. Ultra-high purity gases were N_2 (99.999%) and He (99.98%). The gases used for XAS and XRD experiments were purchased from AirGas, Illinois, and all the gases were balanced with He.

2.3.2 Catalyst preparation

Pt-Bi bimetallic catalysts on silica with target Pt loading of 2 wt% were synthesized by a sequential incipient wetness impregnation (IWI). 0.2 g Pt(NH$_3$)(NO)$_2$ was dissolved in 3.5 mL DI water. The obtained solution was added dropwise to 5.0 g Silica (Davisil 636 silica gel, 480 m^2/g, 0.75 mL/g pore volume) with continuous stirring. Pt/SiO$_2$ was dried at 100 °C overnight followed by calcination at 400 °C for 4 hours. Different amounts of Bi(NO$_3$)$_3$ ·5H$_2$O was dissolved in 3.5 mL 2 mol/L nitric acid. The solution was added dropwise to the Pt/SiO$_2$ catalyst. The obtained catalysts were dried overnight at 100 °C and calcined at 400 °C for 4 h. These samples are referenced as xBi-2Pt/SiO$_2$, where x denotes as x wt% of Bi loading. For comparison,

the monometallic 2Pt/SiO_2 catalyst with 2 wt% Pt loading was also prepared using the same method.

ZSM-5 (Si/Al=40) of ammonium form (CBV 8014, 425 m^2/g) was calcined at 550 °C for 4 hours to transform into H-form. Pt-Bi bimetallic catalysts on ZSM-5 with target Pt loading of 1 wt% were synthesized by a sequential wet impregnation. $H_2PtCl_6 \cdot 6H_2O$ was dissolved in HCl (pH=5-6) solution and added dropwise to HZSM-5 slurry, with stirring at room temperature for 8 hours. Pt/HZSM-5 was dried at 100 °C overnight followed by calcination 400 °C for 4 hours. Various amounts of $BiCl_3$ were dissolved in HCl solution (pH=5-6) and added dropwise to Pt/HZSM-5. The obtained catalysts were dried overnight at 100 °C and calcined at 400 °C for 4 h. These samples are named as xBi-1Pt/ZSM-5, where x denotes as x wt% of Bi loading. For comparison, the monometallic 1Pt/ZSM-5 catalyst with 1 wt% Pt loading was also prepared using the same method.These catalysts were shown to have similar activity, C2+ selectivity and stability for NOCM as previously reported. [52]

2.3.3 *In situ* X-ray diffraction (XRD)

The XRD measurements were performed at 11-ID-C beamline at the Advanced Photon Source (APS) in Argonne National Lab. X-rays at 105.715 keV (=0.11730 Å) were used to acquire the XRD patterns. Catalyst samples were pressed into small pellets and placed into a Linkam Thermal Stage to perform the XRD measurements. The stage was purged with He at room temperature. 5% H_2/He at 50 cc/min was introduced to the stage and the temperature was ramped to 550 °C. After reduction for 30 min, the diffraction pattern was collected at 550 °C. After cooling the sample to room temperature, the diffraction pattern was collected. The diffraction data for the empty stage and silica support was also collected with the same procedure for background subtraction. The obtained 2-D diffraction patterns were converted to 1-D patterns of intensity versus 2θ by the Fit2D software. The diffraction patterns of Pt (ICSD:9012957) [53], Pt_1Bi_1 (ICSD:9008911) [54], Pt_1Bi_2 (ICSD:9012345) [55],

Bi (ICSD:2310889) [56] were simulated by using standard patterns with Materials Analysis Using Diffraction (MAUD) v. 2.5.5 software. The XRD simulation of Pt_1Bi_1 and Pt_3Bi intermetallic alloy was based on the proposed crystal structure.

2.3.4 *In situ* X-ray absorption spectroscopy (XAS)

The XAS measurements were performed at 10-BM beamline at the APS. Measurements were carried out in step-scan transmission mode in about 10 min. Samples were pressed in a cylindrical sample holder containing six wells to form self-supported catalyst wafers. The sample holder was placed in a quartz tube with ports containing Kapton windows so samples could be treated prior to measurements. The catalysts were pre-reduced in 100 cc/min of 3% H_2/He at 550 °C before taking the spectra at room temperature.

XAS data was fitted by using Demeter 0.9.25 software package. The edge energy was determined using the maximum of the first peak in the first derivative of the XANES spectra. Least-squares fit in R-space of the k^2-weighted Fourier transform data from 3.0 to 12.0 [1] was used to obtain the EXAFS coordination parameters. The first shell was used to fit the EXAFS spectra. The amplitude reduction factor (S_0^2) was determined as 0.80 by fitting a reference spectrum of the Pt foil, and then it was used for fitting of all the other EXAFS spectra. One Pt and Bi path were included, and eight free parameters were used for the initial fitting. With the information of the Pt3Bi1 structure, three-path fitting was carried out by fixing one Pt-Pt path as an equal distance as one Pt-Bi path, and the ratio of the coordination numbers of the two paths was set as 2:1 consistent with the Pt_3Bi crystal structure.

2.3.5 STEM

STEM experiments were conducted using the FEI Talos F200X scanning transmission electron microscope with a high angle annular dark field (HAADF) detector at 300 kV. The samples were reduced in H2 at 550 °C for 30 min and exposed to air at

the room temperature before the STEM measurement. The samples were grounded and dispersed in isopropanol. Then the suspension was dropped on Au TEM ready grids (TedPella) and dried on a hot plate. The particle size distribution was determined by counting 200 particles per sample using Nano Measurer 1.2.

2.3.6 CO FTIR

In situ Fourier Transform Infrared spectra were acquired with a Bruker TENSOR27 spectrometer equipped with a mercury cadmium telluride detector in transmission mode between 1000 cm^1 and 4000 cm^1 with 32 scans and a resolution of 4 cm^1. About 30 mg of the sample was pressed to a disk with a diameter of 13 mm. The samples were pretreated in 50 mL/min of N_2 at 120 °C for 10 min and then cooled down to room temperature to collect the background spectrum. 5% CO/He was then flowed in the sample disk for 5 10 min until the intensity of gaseous peaks didn't change. Subsequently, the gas was switched to N2 (50 mL/min) to collect the spectra until the CO gaseous peaks disappeared. Then the samples were reduced in 50 mL/min H_2 at 500 °C for 20 min. Finally, the samples were cooled down to room temperature and the CO adsorption and N_2 blowing processes were repeated.

2.3.7 CO chemisorption

CO chemisorption was performed on a Micromeritics ASAP 2020 chemisorption instrument. Around 0.1 g catalysts were weighted and loaded into a U-shaped quartz reactor. 50 cm^3/min of 5% H_2/He was introduced into the reactor to reduce the catalysts at 550 °C and cooled to RT. He was flushed for 30 min before evacuation and measurements. The catalyst dispersion was obtained by difference analysis in the chemisorption curve. A stoichiometry of CO: Pt = 1 : 1 was assumed to calculate the dispersion for the catalysts.

2.3.8 Propane dehydrogenation catalytic performance tests

Propane dehydrogenation catalytic performance was tested in a quartz tube reactor (I.D. = 9.5 mm) connected to Agilent 6890 gas chromatograph. A K-type thermocouple (O.D. = 3.2 mm) was placed in the center of the catalyst bed to measure the temperature of the catalyst. A furnace connected to a controller was used to maintain the desired temperature. The catalyst was diluted with Davisil 636 silica gel to maintain the catalyst bed height at 12.7 mm. The criteria by Weisz and Prater [57] and Mears [58] were both satisfied, confirming the absence of heat-transfer and mass-transfer effects in all measurements.

Prior to the reaction, the catalysts were reduced at 550 °C at 50 mL/ h 5% H_2 and balance N2 while temperature was ramped from room temperature to 550 °C at 10 °C / min and held at 550 °C for 30 min. The reaction temperature was 550 °C and the reactants were 2.5% C3H8, 2.5% H2 and balance N_2. The gas hourly space velocity (GHSV) was adjusted to determine the selectivity at certain conversions. A Carboxen-1010 PLOT capillary GC Column was used to separate the components in the reactor effluent gas mixture.Selectivity was calculated by C_3H_6/(total carbon - C_3H_8)×100%.

2.4 Results and discussion

The Pt L_3 edge X-ray Absorption near edge structure (XANES) spectra of Pt-Bi on ZSM-5 with different Bi loadings are shown in Figure 2.1 (A). These catalysts had similar catalytic performance for NOCM as previously reported. [52] The white line intensity is typical of fully reduced metallic Pt in all catalysts. The edge energies determined by the inflection point of the leading edge are given in Table 2.1. The edge energy of 0.1Bi-1Pt/ZSM-5 was 0.1 eV higher than monometallic Pt; while those of 0.8Bi-1Pt/ZSM-5 and 1Bi-1Pt/ZSM-5 were 0.6 eV higher. The shift in XANES energy and change in the shape of the white line suggest that Pt and Bi form bimetallic nanoparticles.

Table 2.1.
XANES edge energy for the catalysts

Sample Name	XANES edge energy (keV)
$2Pt/SiO_2$	11.5640
$1Bi\text{-}2Pt/SiO_2$	11.5646
$2Bi\text{-}2Pt/SiO_2$	11.5647
$4Bi\text{-}2Pt/SiO_2$	11.5648
1Pt/ZSM-5	11.5640
0.1Bi-1Pt/ZSM-5	11.5641
0.8Bi-1Pt/ZSM-5	11.5646
1Bi-1Pt/ZSM-5	11.5646

The atomic numbers of Pt and Bi differ only by 5; therefore, scattering from Pt-Pt and Pt-Bi at the same bond distance shows only slight differences in the k space extended X-ray absorption fine structure (EXAFS) spectra as shown in Figure 2.1. Although there are minor differences, these are not generally large enough to resolve the contributions in the EXAFS. If however, the Pt-Pt and Pt-Bi bond distances are different, the differences in EXAFS are larger (Figure 2.1) and can be resolved in the fits.

Three main peaks in k^2-weighted magnitude of the Fourier transform of Pt/ZSM-5 shown in Figure 2.2 (C) are typical Pt-Pt scattering of metallic Pt nanoparticles. The peak positions and relative intensities, however, change with increasing Bi loading suggesting the presence of Bi scattering neighbors within the bonding distance. Despite the similar particle sizes, [52] the magnitude of the Fourier transform decreases with increasing the Bi loading likely indicating the presence of destructive interference of the EXAFS.

The fit of the EXAFS at Pt edge of the Pt-Bi/ZSM-5 catalysts are given in Table 2.2. The 2Pt/ZSM-5 has a Pt-Pt coordination number of 10.2. The Pt-Pt bond distance is 2.74 Å, in agreement with the Pt nanoparticles. For Pt-Bi catalysts, fits of the EXAFS with a single scattering distance were poor. Using two scattering paths, a Pt-Pt bond distance at 2.75 Å, and a second scattering path of Pt-M, where M could

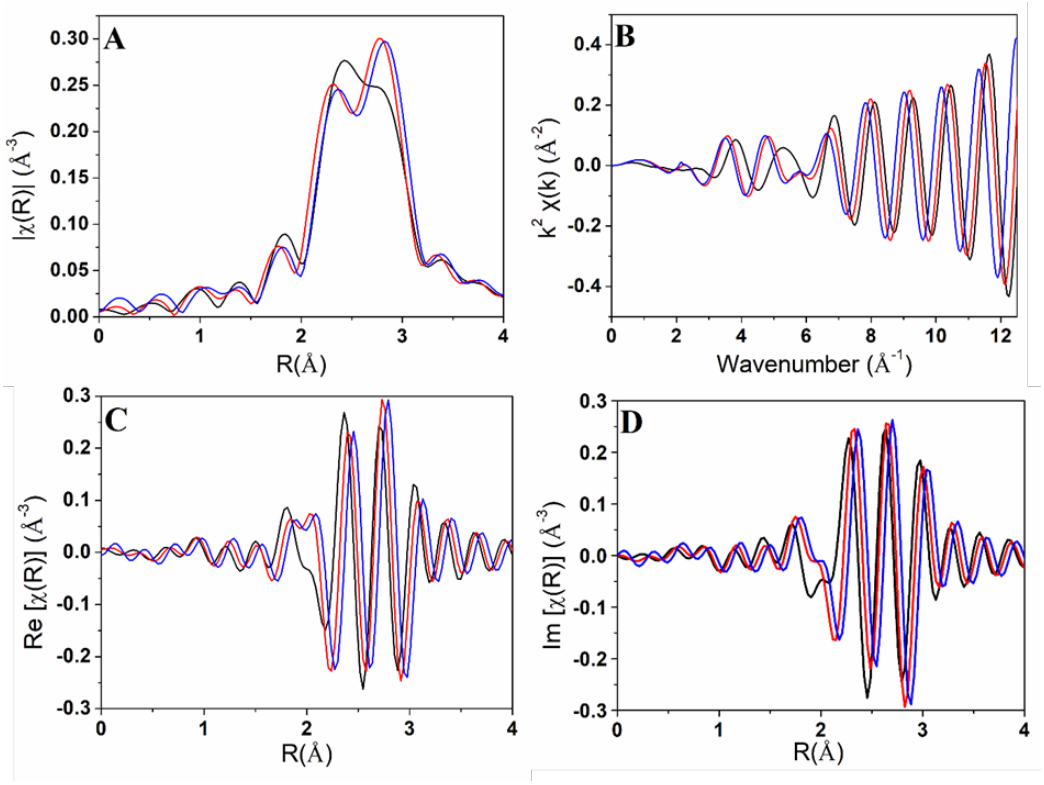

Fig. 2.1. Pt L_3 edge EXAFS spectra FEFF calculation: A) R space FT magnitude, B) k space, C) R space FT real part and D) R space FT imaginary part. Pt-Pt at R=2.75 Å (black), Pt-Bi at R=2.75 Å (red), Pt-Bi at R=2.80 Å (blue).

be Pt or Bi, at a bond distance of 2.81 Å gave good fits. The Pt-M coordination number increased with increasing Bi, at a bond distance of 2.81 Å gave good fits. The Pt-M coordination number increased with increasing Bi loading suggesting M is likely Bi. The Pt-Pt coordination number is larger than Pt-M, which suggests Pt-rich bimetallic Pt-Bi nanoparticles.

To study the crystal phase of the bimetallic nanoparticles, diffraction is needed. The XRD spectra of Pt-Bi/ZSM-5 shown in the previous study, however, have large ZSM-5 peaks, which obscure the weak Pt-Bi metallic nanoparticle peaks. [52] Therefore, Pt and Pt-Bi catalysts of similar composition were synthesized on amorphous SiO_2 support to allow nanoparticle diffraction to be resolved. The STEM images of

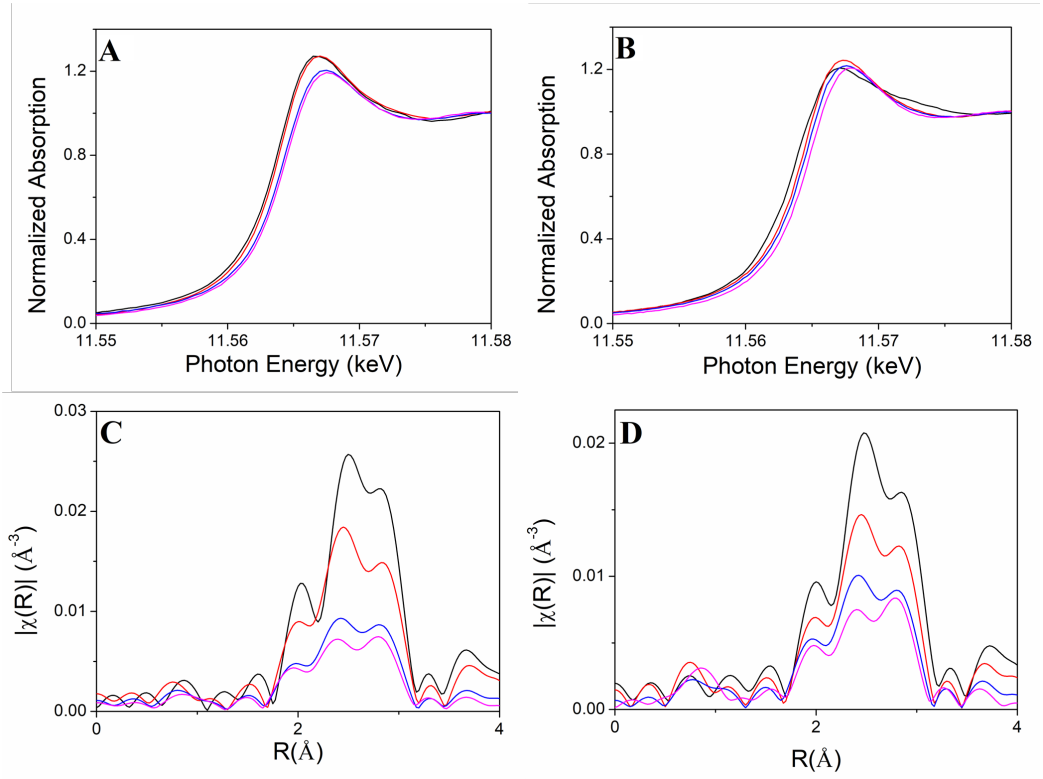

Fig. 2.2. Figure 1. (A) Pt L_3 edge XANES spectra of Pt-Bi/ZSM-5. (B) Pt L_3 edge XANES spectra of Pt-Bi/SiO_2 (C) k^2-weighted Fourier transformation magnitude of the EXAFS spectra of Pt-Bi/ZSM-5. k^2-weighted FT k-range of 3.0 – 12.5 Å^{-}1. (D) k^2-weighted Fourier transformation magnitude of the EXAFS spectra of Pt-Bi/SiO_2. k^2-weighted FT k-range of 3.0 – 12.5 Å^{-}1. For (A) and (C): 1Pt/ZSM-5 (black), 0.1Bi-1Pt/ZSM-5 (red), 0.8Bi-1Pt/ ZSM-5 (blue) and 1Bi-1Pt/ZSM-5 (magenta). For (B) and (D): 2Pt/SiO_2 (black), 1Bi-2Pt/SiO_2 (red), 2Bi-2Pt/SiO_2 (blue) and 4Bi-2Pt/SiO_2 (magenta).

the Pt-Bi/SiO_2 catalysts are shown in Figure 2.3. The average particle size is 2-3 nm, Table 2.2 and Figure 2.4, which are similar to those in Pt-Bi/ZSM-5 [52] The infrared spectra also show linear bonded CO at similar frequencies, Figure 2.5.

The bimetallic nanoparticles on Pt-Bi/SiO_2 catalysts are very similar to the ones on Pt-Bi/ZSM-5 according to XAS. The Pt L_3 XANES spectra and edge energies of the Pt-Bi/SiO_2 are shown in Figure 2.2 (B) and Table 2.1, respectively. Compared with Pt/SiO_2, the edge energies of 2Pt-1Bi/SiO_2, 2Pt-2Bi/SiO_2 and 2Pt-4Bi/SiO_2

Table 2.2.
EXAFS fitting parameters for Pt-Bi/ZSM-5

Sample Name	Scattering Pair	CN	Bond distance (Å)	σ^2 (Å^2)
1Pt/ZSM-5	Pt-Pt	10.2±0.4	2.74±0.02	0.004
1Pt-0.1Bi/ZSM-5	Pt-Pt	9.4±0.9	2.75±0.01	0.005
	Pt-Bi	1.1±0.9	2.81±0.05	0.009
0.8Bi-1Pt/ZSM-5	Pt-Pt	6.1±0.6	2.75±0.01	0.006
	Pt-Bi	2.7±1.5	2.81±0.03	0.005
1Bi-1Pt/ZSM-5	Pt-Pt	4.8±0.8	2.75±0.01	0.005
	Pt-Bi	3.4±1.3	2.80±0.04	0.009

Table 2.3.
Propane dehydrogenation, CO chemisorption and STEM Particle Size[a]

Sample Name	C_3H_6 Selectivity (%)	Particle size (nm)[b]	Pt Dispersion (%)[c]	Initial Turnover Rate (s^{-1}) [d]
2Pt/SiO_2	60	2.7±0.5	30.2	0.22
1Bi-2Pt/SiO_2	90	2.3±0.5	8.2	0.43
2Bi-2Pt/SiO_2	87	2.2±0.4	6.5	0.58
4Bi-2Pt/SiO_2	87	2.7±0.4	4.4	0.31

[a] Reaction conditions: 550 °C , 2.5 % C_3H_8 + 2.5 % H_2 balanced with N_2; selectivity and TOR calculated at 10% C_3H_8 conversion.
[b] Particle size calculated from STEM.
[c] Pt dispersion calculated by CO chemisorption.
[d] TOR calculated based on C_3H_8 conversion rate.

were shifted to higher energy, 0.6 eV, 0.7 eV and 0.8 eV, respectively. The increase in the XANES energy with increasing Bi loading is similar to that in Pt-Bi/ZSM-5. The k^2-weighted magnitude of the Fourier transform of the Pt-Bi/SiO_2 catalysts are shown in Figure 2.2 (D) and decrease with increasing Bi loading very similar to that on ZSM-5 (Figure 2.2 (C)). The Pt-Pt coordination number was 8.7 and the bond distance was 2.73 Å, similar to 1Pt/ZSM-5. For Pt-Bi/SiO_2 catalysts (Table 2.4), the catalysts were fit using two scattering paths. The Pt-Pt bond distance is 2.74-2.76 Å, which is similar to Pt-Bi/ZSM-5. A second scattering path of Pt-Bi at a bond distance of 2.79 Å gave good fits. The Pt-M coordination number increases as the Bi loading increases consistent with M being Bi. The k space and R space

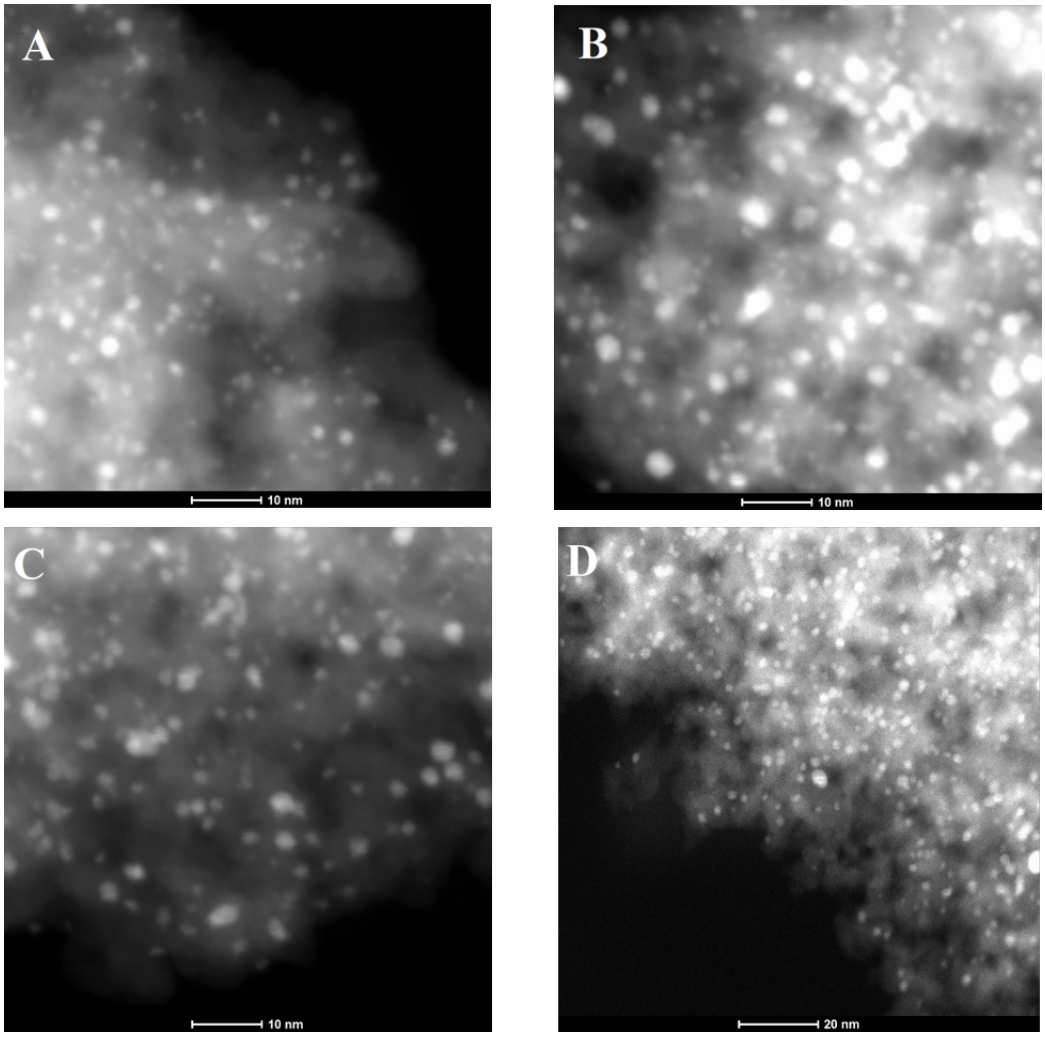

Fig. 2.3. STEM HAADF images of A) 2Bi-2Pt/SiO_2 (2.7±0.5 nm), B) 4Bi-2Pt/SiO_2 (2.3±0.5 nm), C) 2Pt/SiO_2 (2.2±0.4 nm), D) 1Bi-2Pt/SiO_2 (2.7±0.4 nm)

EXAFS spectra of 2Bi-2Pt/SiO_2 and 0.8Bi-1Pt/ZSM-5 have nearly identical spectra (Figure 2.6), and suggest that the Pt-Bi nanoparticle structures on silica and ZSM-5 are similar.

To further investigate the phase assemblage of the Pt-Bi bimetallic nanoparticles, in situ synchrotron XRD patterns were obtained on Pt-Bi/SiO_2 at 550 °C (Figure 2.7 (A)). The energy of the X-ray beam is 105.715 keV, resulting in diffraction peaks at low two theta angle. 2Pt/SiO_2 showed peaks at 2.980°, 3.430°, 4.881°, and 5.712°

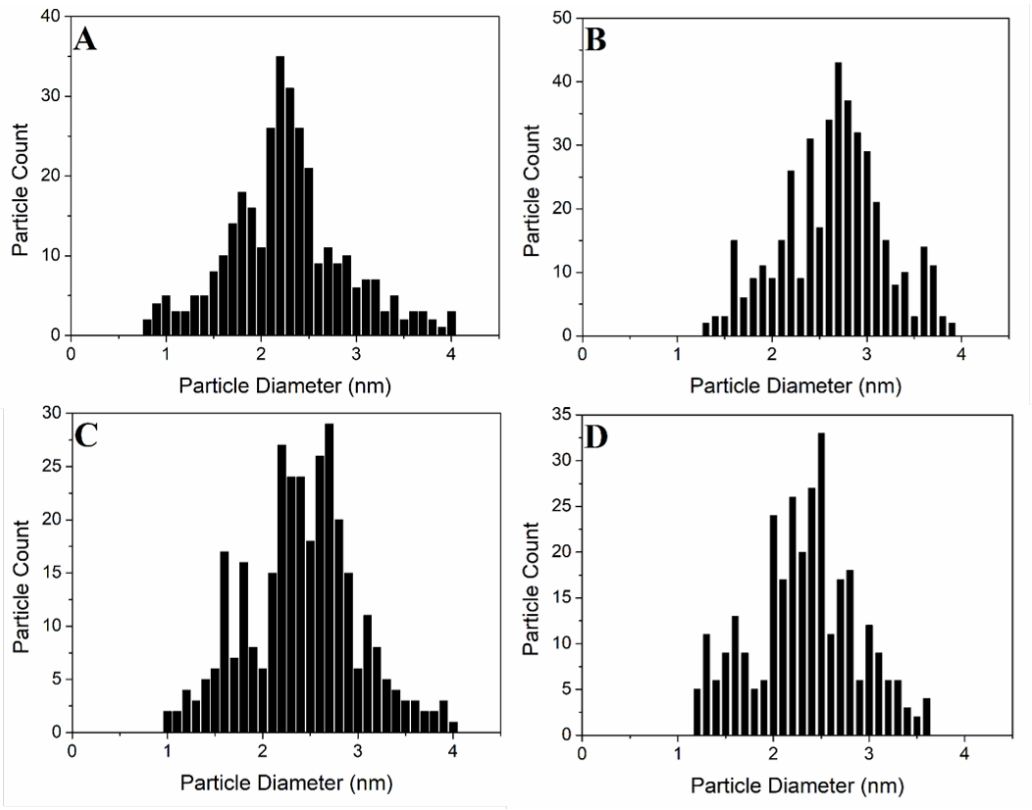

Fig. 2.4. Particle size distribution statistics of A) 2Pt/SiO_2 (2.2±0.6 nm), B) 1Bi-2Pt/SiO_2 (2.7±0.5 nm) C) 2Bi-2Pt/SiO_2 (2.4±0.5 nm), D) 4Bi-2Pt/SiO_2 (2.3±0.5 nm)

Table 2.4.
EXAFS fitting parameters for Pt-Bi/SiO_2

Sample Name	Scattering Pair	CN	Bond distance (Å)	σ^2 (Å^2)
2Pt/SiO_2	Pt-Pt	8.7±0.1	2.73±0.01	0.007
1Bi-2Pt/SiO_2	Pt-Pt	8.5±1.7	2.74±0.01	0.006
	Pt-Bi	1.1±6.4	2.79±0.15	0.012
2Bi-2Pt/SiO_2	Pt-Pt	5.6±0.9	2.74±0.03	0.006
	Pt-Bi	1.6±3.5	2.79±0.10	0.008
4Bi-2Pt/SiO_2	Pt-Pt	1.8±0.9	2.76±0.04	0.005
	Pt-Bi	4.2±1.0	2.78±0.03	0.009

corresponding to the (111), (200), (220) and (311) planes of the Pt face-centered cubic (FCC) structure. For the Pt-Bi catalysts, the peaks shift slightly to lower two Theta

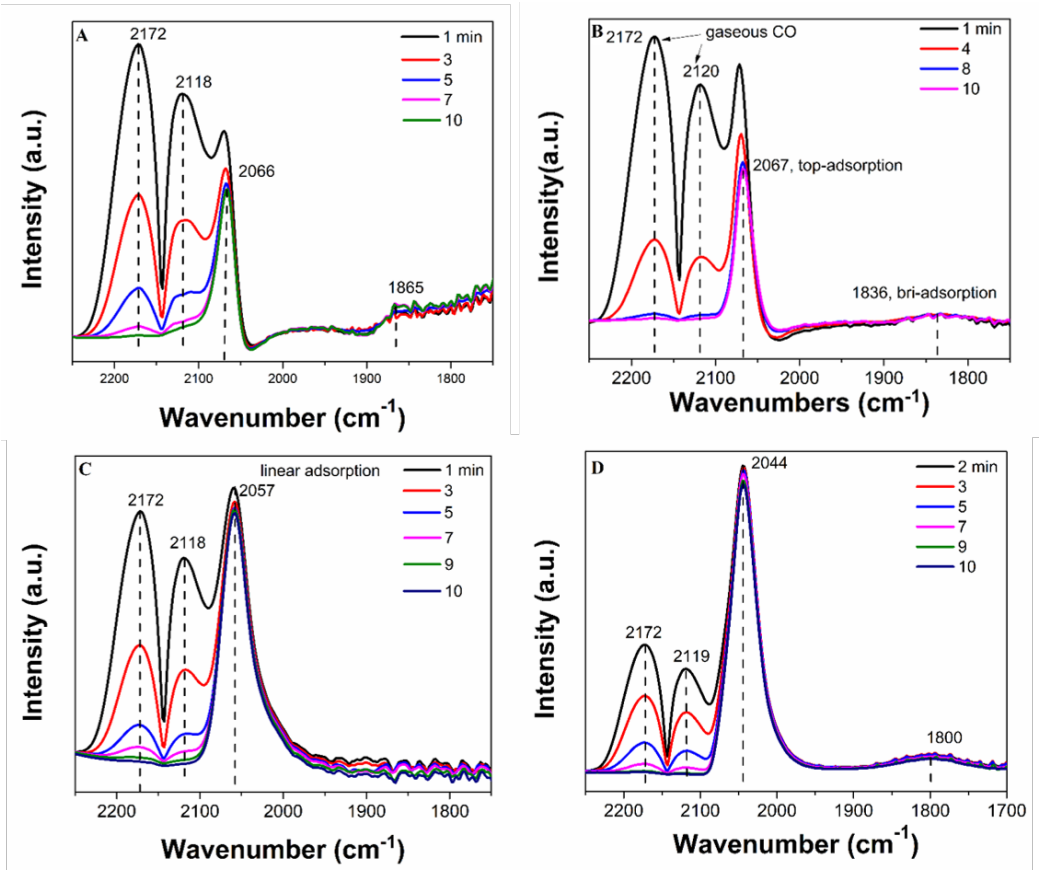

Fig. 2.5. CO FTIR analysis of BiPt Bimetallic catalyst; CO adsorption before H_2 reduction: (A) 0.8Bi1Pt/ZSM-5, (B) 1Bi2Pt/SiO_2; CO adsorption after H_2 reduction: (C) 0.8Bi1Pt/ZSM-5, (D) 1Bi2Pt/SiO_2

angles with increasing Bi loadings (Table 2.5), indicating lattice expansion caused by Bi incorporation due to the larger size of Bi than Pt, with atomic radii 1.56 and 1.39 Å, respectively. [59] In addition, the diffraction patterns of the Pt-Bi catalysts remain similar to the Pt catalyst. The relative peak positions and intensity are characteristic of FCC lattice. This suggests either formation of FCC Pt-Bi solid solution, or an intermetallic alloy with superlattice based on the FCC lattice. The former is not likely since the solubility of Bi in Pt is less than 1%, [60] which is inconsistent with the EXAFS fits in Tables 1 and 3 suggesting much higher Bi content. Solid solutions with high solubility generally form between two metals having the same lattice type (for example, FCC). [61] Though Pt is FCC, Bi is rhombohedral. In addition, the

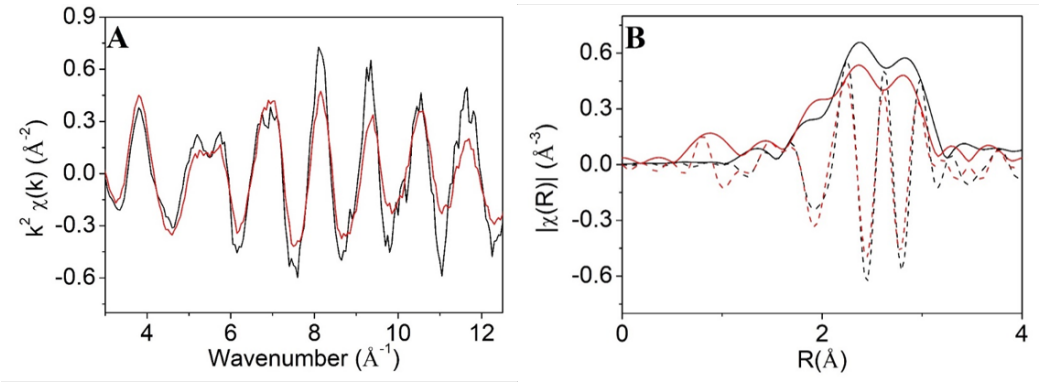

Fig. 2.6. EXAFS comparison between 2Bi-2Pt/SiO_2 and 0.8Bi-1Pt/ZSM-5 (A) k^2-weighted χ (k) for 2Bi-2Pt/SiO_2 (black) and 0.8Bi-1Pt/ZSM-5 (red) (B) k^2-weighted Fourier transformation magnitude (dashed lines) and imaginary part (solid lines) of the EXAFS spectra for 2Bi-2Pt/SiO_2 (black) and 0.8Bi-1Pt/ZSM-5 (red)

average Pt-Bi bond distance would be the sum of the radii of Pt and Bi or 2.95Å for a solid solution with 50% Bi. The experimental bond distance is much shorter at 2.80 Å, suggesting the presence of strong Pt-Bi bonds consistent with the formation of an intermetallic alloy. Finally, previous studies on similar nanoparticles between Pt and a second metal, including In [62], Mn [63] and Sb [64] shows that incorporation of the second metal into the Pt nanoparticles are diffusion limited due to the strong Pt-M bonds, leading to intermetallic transformation starting from the surface layers, which is consistent with our interpretation of the characterization data on Pt-Bi catalysts. Thus, the bimetallic Pt-Bi is not a solid solution.

Table 2.5.
Peaks of the XRD spectra taken at 550°C

Sample Name	(111) peak (°)	(200) peak (°)	(220) peak (°)	(311) peak (°)
2Pt/SiO_2	2.980	3.430	4.881	5.712
1Bi-2Pt/SiO_2	2.959	3.404	4.861	5.680
2Bi-2Pt/SiO_2	2.942	3.378	4.835	5.650
4Bi-2Pt/SiO_2	2.937	-	-	-

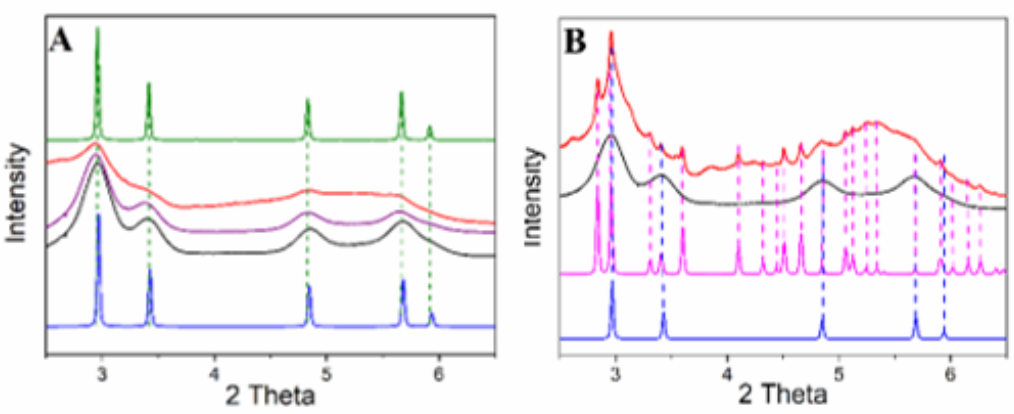

Fig. 2.7. (A) *In situ* XRD patterns taken at 550 °C (X-ray energy=105.715 keV). (B) *In situ* XRD patterns taken at room temperature (X-ray energy=105.715 keV). Pt simulation (blue, ICSD 9012957), Bi simulation (magenta, ICSD 2310889), Pt_3Bi simulation (olive),1Bi-2Pt/SiO_2 (black), 2Bi-2Pt/SiO_2 (purple), 4Bi-2Pt/SiO_2 (red).

For possible intermetallic phases, the two thermodynamically stable bulk phases, Pt_1Bi_1, [54] Pt_1Bi_2 [55] (Figure 2.8 (A)) do not have FCC type lattice, and their XRD peak positions do not match those of the Pt-Bi bimetallic nanoparticles. Thus, neither is the structure of these nanoparticles. Since the bimetallic Pt-Bi nanoparticles are not solid solutions, nor known bulk alloy structures, it is possible that there is a new nano-phase intermetallic alloy structure. Recently, several intermetallic nanoparticle alloy catalysts with AuCu structure, or closely related cubic structure, have been determined for Pt_1Zn_1, [2] β_1-PdZn [65] and Pd_1In_1. [62]For each of these, the nano-alloy phase is known in the bulk phase diagram. However, recently, Ye *et al.* identified a surface tetragonal Pt1Sb1 intermetallic nanoparticle phase with AuCu structure type, which does not exist in the bulk.30 A simulated Pt1Bi1 XRD pattern based on the same type of AuCu tetragonal structure (Pt-M at 2.81 Å and Pt-Pt at 2.74 Å) is shown in Figure 2.8 (B). This structure also does not match the diffraction peaks of the Pt-Bi catalysts.

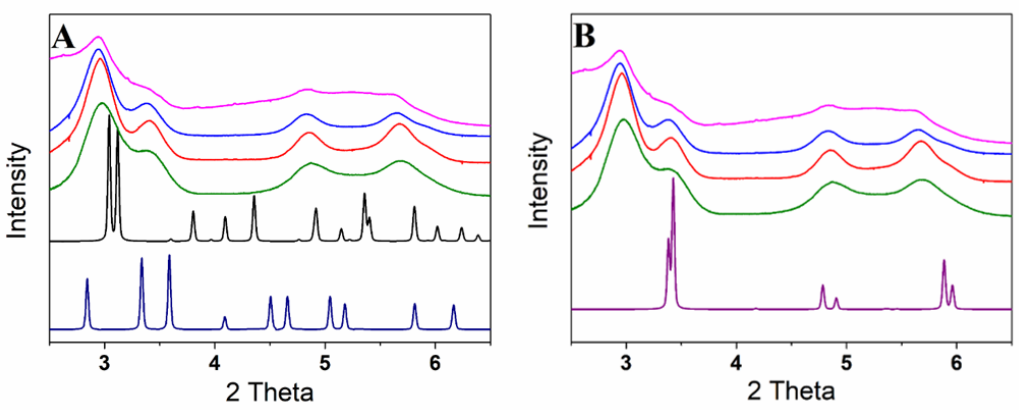

Fig. 2.8. Simulated XRD patterns (A) XRD patterns of Pt-Bi bulk alloys and experimental Pt-Bi/SiO_2 taken at 550 °C (X-ray energy=105.715 keV). Pt_1Bi_1 simulation (black, ICSD:9008911), Pt_1Bi_2 simulation (navy, ICSD:9012345) (B) XRD patterns of simulated tetragonal Pt_1Bi_1 (AuCu structure type) and experimental Pt-Bi/SiO_2 taken at 550 C (X-ray energy=105.715 keV). Tetragonal Pt_1Bi_1 simulation (purple, Pt-Pt bond distance=2.74 Å, Pt-Bi bond distance= 2.81 Å), Pt/SiO_2 (olive), 1Bi-2Pt/SiO_2 (red), 2Bi-2Pt/SiO_2 (blue), 4Bi-2Pt/SiO_2 (magneta).

In the previous study by Gercecker *et al.* [11] Pt-Sn supported on SiO_2 and ZSM-5 was catalytic for NOCM, and Pt-Sn is known to have an Cu_3Au type intermetallic Pt_3Sn [66–68] structure. In this Pt_3M structure, Pt-Pt and Pt-Bi bond distances and the XRD patterns are very similar. A simulation of Cu_3Au type Pt_3Bi phase with Pt-M with bond distances at 2.81 Å and second monometallic Pt phase with bonds at 2.74 Å, which are consistent with the EXAFS fits, gave an XRD pattern that matches the experimental peak positions in Figure 2.7 (A).Because the atomic number of Pt and Bi are similar, the superlattice peaks are too weak to be seen even in the simulation. Nevertheless, based on the EXAFS and XRD results, the bimetallic Pt-Bi nanoparticle is proposed to consist of two phases: Pt_3Bi (Figure 2.9) and unalloyed Pt, i.e., a Pt-rich Pt-Bi bimetallic nanoparticle.

Several possibilities exist for the two metallic phases in the Pt-Bi catalysts. These could be two separate phases, e.g., Pt and Pt_3Bi, a core-shell morphology, for exam-

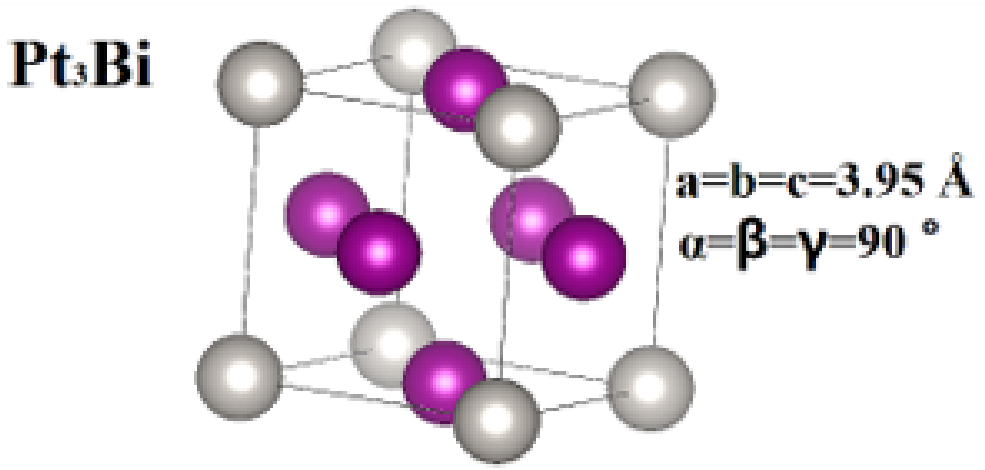

Fig. 2.9. Structure of the simulated Pt_3Bi structure

ple, Pt_3Bi on a Pt core, or the inverse. In order to determine the location of the alloy phase, the catalytic performance for propane dehydrogenation was determined for the Pt-Bi/SiO_2 catalysts. Hydrogen was co-fed with propane to increase the hydrogenolysis selectivity to light alkanes, e.g., methane, ethane and ethylene, and provides a more severe test of the catalysts' olefin selectivity. The propylene selectivity are shown in Figure 2.10 and Table 2.3 (at 10% conversion).

The propylene selectivity at 10% conversion for 2Pt/SiO_2 was 60%; while for Pt-Bi bimetallic catalysts the selectivity was ca. 90%. The propylene selectivity for monometallic Pt decreased rapidly with increasing conversion; while the propylene selectivity for Pt-Bi bimetallic catalysts remained nearly constant at about 90% as the conversion increased. As the Bi loading increases from 1-4%, there is little change in the propylene selectivity. The high olefin selectivity at low promoter loading suggests a Pt3Bi intermetallic surface alloy on a Pt core, [37] similar to other intermetallic alloys. [42, 62, 66, 69]

HAADF image (Figure 2.11(A)) reveals the atomic structure of an individual Pt-Bi particle in 0.8Bi-1Pt/ZSM-5. The EDS provides intuitive elemental distribution of Pt and Bi, where a Pt-Bi alloy shell in thickness of 1 nm could be confirmed outside a 1 nm Pt-rich core. The lattice spacing of 0.23 nm and 0.21 nm at the shell

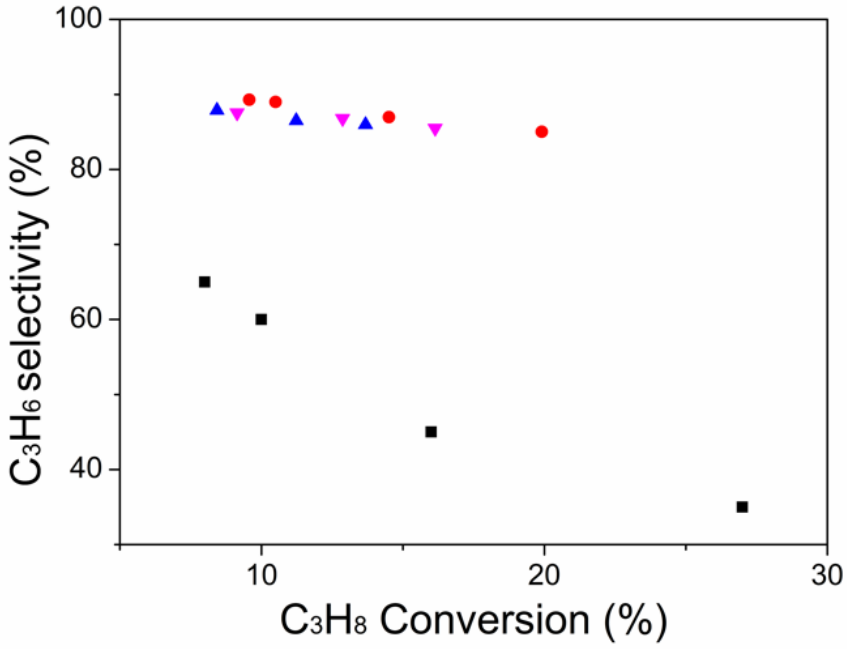

Fig. 2.10. Propylene selectivity at different conversions of $2Pt/SiO_2$ (black), $1Bi\text{-}2Pt/SiO_2$ (red), $2Bi\text{-}4Pt/SiO_2$ (blue) and $4Bi\text{-}2Pt/SiO_2$ (magenta). Reaction conditions: 550 °C, 2.5 % C_3H_8 + 2.5 % H_2 balanced with N_2.

can be indexed to be (111) and (200) planes of a typical FCC phase. In addition, the line-distribution of Pt and Bi (Figure 2.12) shows the fact of a Pt-Bi alloy shell encapsulating outside a Pt-rich core. High-resolution HAADF image (Figure 2.11(A)) shows FCC atomic arrangement symmetry suggesting the Pt3Bi structure for the shell and the metallic Pt core. The above structural evidences coincide with the propane dehydrogenation analysis serving as additional real-space microscopic evidence for the unique core-shell configuration of the Pt-Bi particle.

The turnover rates (TORs), i.e., rate per surface Pt, under differential conditions are also given in Table 2.3. The initial TORs of $Pt\text{-}Bi/SiO_2$ are very similar to that of $2Pt/SiO_2$ at 550°C. However, at higher reaction temperature, or reduction at higher temperatures and reaction at 550°C, the rates per gram of catalyst were

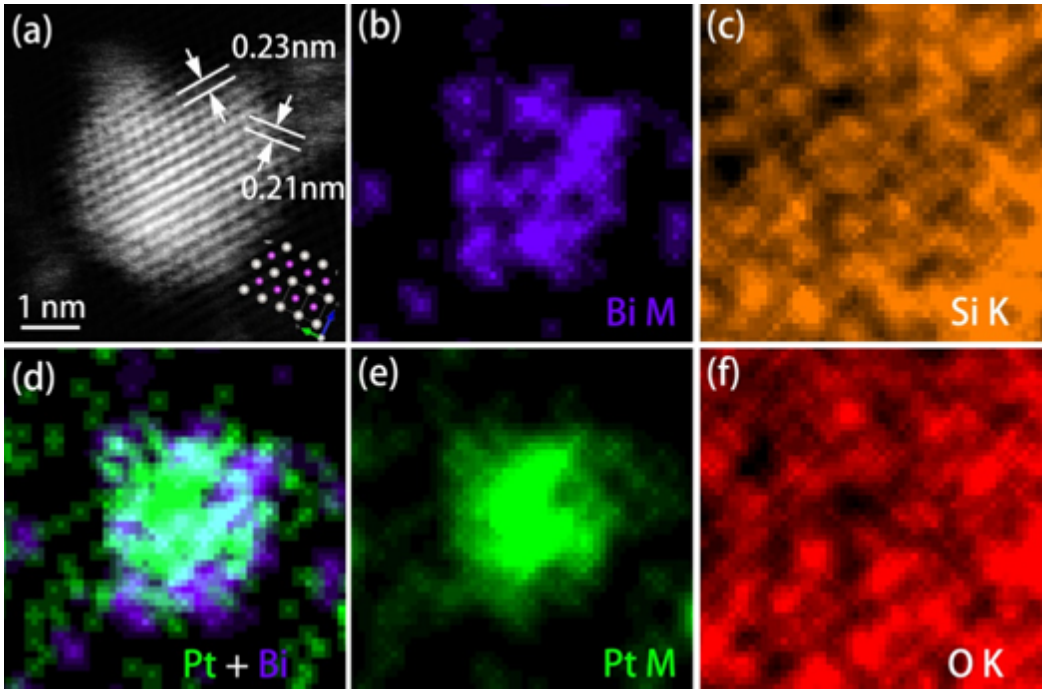

Fig. 2.11. (A) The high resolution HAADF image and elemental distribution of (B) Bi, (C) Si , (E) Pt , and (F) O as revealed by EDS analysis. The core-shell configuration has been clearly demonstrated by (D) the mix-over image of Pt M and Bi M signals.

much lower. The XRD pattern of 4Bi-2Pt/SiO_2 taken at 550 °C, Figure 2.7 (A) (red), showed broad peaks typical of the surface Pt_3Bi on Pt core structure of the Pt-Bi catalysts. However, upon cooling the pattern collected at room temperature showed many additional sharp features, Figure 2.7 (B) (red). These new peaks match those of metallic Bi. Thus, at high Bi loading and high reduction temperatures, excess Bi_2O_3 reduces to metallic Bi as liquid form (melting point of Bi is 271.5°C [70]). The loss of catalytic activity is likely due to covering of the catalytic Pt_3Bi with non-catalytic, metallic Bi.

At lower Bi loading, for example, 1% Bi, Figure 2.7 (B) (black), there are no metallic Bi peaks in the XRD at room temperature. These results suggest that for Pt-Bi, low Bi loadings and low reduction temperatures are required to maintain catalytic activity. At high Bi loading, or reduction temperatures, excess Bi is reduced,

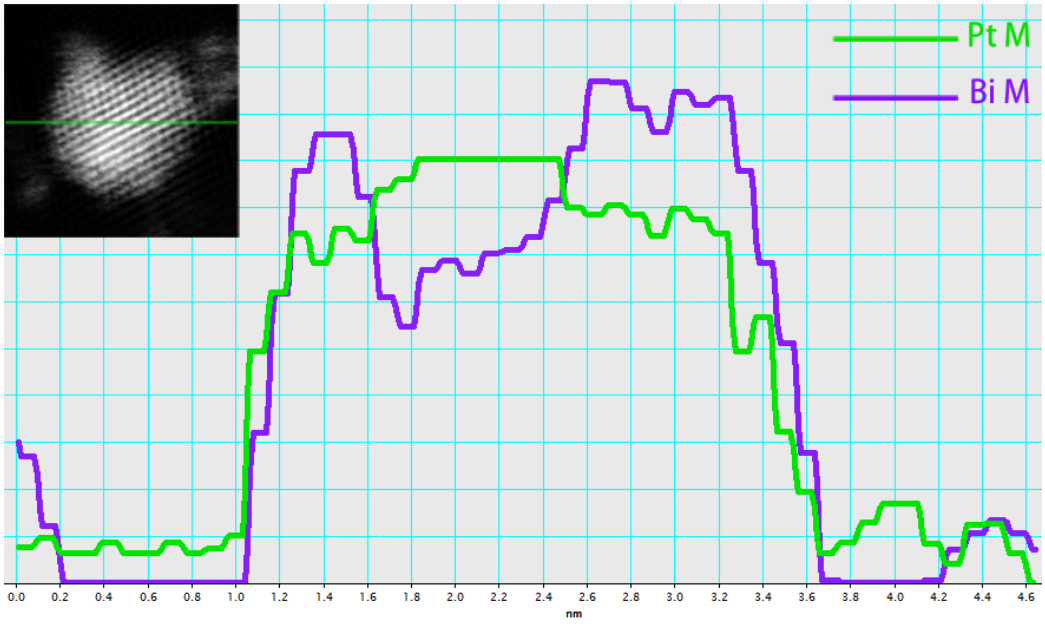

Fig. 2.12. The extracted profile of Pt M and Bi M concentration across single PtBi bimetallic nanoparticle as show inset.

mobile and covers active sites. These results for Pt-Bi/SiO_2 are consistent with the Pt-Bi/ZSM-5 NOCM catalysts, where high Bi loading, or high reaction temperature leads to poor activity. [52]

The structures of the Pt-Bi bimetallic catalysts with different Bi loadings are schematically shown in Figure 2.13, where at very low loading, e.g. about 0.1%, there is little surface Pt_3Bi and most of the surface is monometallic Pt. This catalyst has catalytic properties similar to Pt, i.e. poor selectivity and stability. At loadings sufficient to produce a Pt_3Bi monolayer, the alkane dehydrogenation (on SiO_2) and NOCM (on ZSM-5) selectivity and stability are higher. With high Bi loading, metallic Bi is more easily reduced and covers the catalytic surface. For all catalysts, the non-reduced Bi_2O_3 present in all catalysts is reduced to metallic Bi at high temperature leading to inactive catalysts. Similar bimetallic structure evolution has been reported for Pd-In [62] and Pd-Zn [42] catalysts.

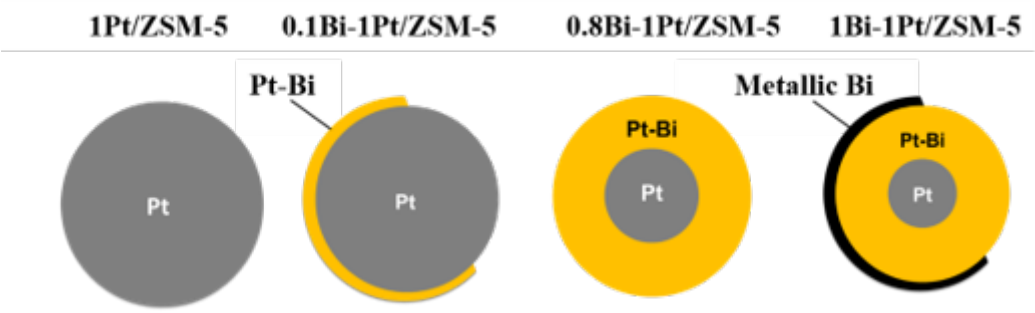

Fig. 2.13. Schematic model of geometric structure of the Pt and Pt–Bi catalysts.

2.5 Conclusions

In summary, the structure of Pt-Bi/ZSM-5 NOCM catalyst is similar to Pt-Bi/SiO_2. EXAFS indicates the formation of Pt-rich bimetallic Pt-Bi nanoparticles with Pt-Bi bond distance of 2.80 Å. The XRD spectra (on SiO_2) are consistent with cubic, intermetallic surface Pt_3Bi phase on a Pt core. The Pt_3Bi structure is not known in the thermodynamic phase diagram. In all catalysts, only a small fraction of Bi alloys with Pt. At high Bi loadings, excess Bi reduces at high temperature, covering the catalytic surface leading to a loss in activity. At lower Bi loadings with little excess Bi, the Pt3Bi surface is effective for NOCM (on ZSM-5) and propane dehydrogenation (on SiO_2).

The current study along with the previous report for NOCM by Pt-Sn catalyst [11] suggests that Pt intermetallic alloys are significantly more selective than monometallic Pt. [25] Both Pt-Sn [66, 67]and Pt-Bi bimetallic compositions have Pt_3M surface structures, suggesting that other Pt_3M alloys, and perhaps other noble metal intermetallic structures, may also be selective for NOCM. In addition, both bimetallic compositions are selective for alkane dehydrogenation. Although NOCM requires the catalyst to form a C-C bond while alkane dehydrogenation does not, these results suggest noble metal intermetallic alloys have high selectivity for both reactions. Finally, high equilibrium conversions of NOCM require very high reaction temperature, typically, up to about 900-1000°C. For Bi, at these temperatures, excess Bi_2O_3 is

reduced and covers the active Pt site leading to loss of activity. For high selectivity and conversion, alloys with promoter metals, that form Pt_3M and are not reduced under these extreme conditions may lead to better performance.

2.6 Conclusions

The authors were supported in part by the National Science Foundation under Cooperative Agreement No. EEC-1647722. Use of the Advanced Photon Source was supported by the U.S. Department of Energy Office of Basic Energy Sciences under contract no. DE-AC02-06CH11357. MRCAT operations, beamline 10-BM, are supported by the Department of Energy and the MRCAT member institutions. The authors also acknowledge the use of beamline 11-ID-C.

3. THR EFFECT OF STRONG METAL-SUPPORT INTERACTION (SMSI) ON PT-TI/SIO2 AND PT-NB/SIO2 CATALYSTS FOR PROPANE DEHYDROGENATION

This chapter is reproduced from Zhu Chen, Johnny, et al."The effect of strong metal-support interaction (SMSI) on Pt-Ti/SiO_2 and Pt-Nb/SiO_2 catalysts for propane dehydrogenation." submitted to Catalysis Science Technology.

3.1 Abstract

Strong metal-support interactions (SMSI) have been widely studied due to its unique catalytic behavior. In this study we show how SMSI affects the Pt-Nb/SiO_2 and Pt-Ti/SiO_2 electronic, geometric and catalytic properties. Transmission electron microscopy (TEM) and CO chemisorption results confirm that the Pt nanoparticles were partially covered by the SMSI oxides. X-ray absorption near edge structure (XANES), *in situ* X-ray photoelectron spectroscopy (XPS), and resonant inelastic X-ray scattering (RIXS) showed little change in the energy of Pt upon interaction with SMSI oxides. The catalytic activity per mol of Pt for ethylene hydrogenation and propane dehydrogenation was lower due to fewer exposed Pt sites, while turnover rates were similar. The propylene selectivity of the latter reaction increased, which is suggested to be due to the due to smaller ensemble sites from exposed Pt resulting on suppression of alkane hydrogenolysis.

3.2 Introduction

Supported metal nanoparticle catalysts are widely applied in petrochemical, refining and environmental technologies. Development of supported metal catalysts mainly focuses on optimizing the size, composition and geometry of the metal site

to maximize the reaction rate, or control selectivity. Various porous materials with high surface areas are often used to support these metals in order to enhance the catalytic performance. Metal-support interaction is also important for tuning the catalytic properties. [71] Tauster et al. first reported significant interactions between group VIII metals and a TiO_2 support, where after high temperature reduction the adsorption of both H_2 and CO on TiO_2-supported group VIII nanoparticles was suppressed. Other partially reducible oxides, such as Nb_2O_5, [72] CeO_2 [73] and FeO_x, [74] also exhibit strong-metal support interactions (SMSI). It is generally recognized that the metal nanoparticles are encapsulated by oxide overlayers blocking access to the nanoparticle surface. The SMSI encapsulation state is thought to occur by reduction of the oxide support to sub-stoichiometric oxides, which migrate on top of the metal nanoparticles. [75]

The SMSI state alters the catalytic properties for many reactions resulting from changes in geometric and electronic properties, although quantification of these effects has been difficult. [76, 77] Kang et al. [78] studied selective hydrogenation of acetylene to ethylene on TiO_2 added Pd catalysts. After reduction at 500 °C, the catalyst showed suppression of CO chemisorption. Their XPS and TPD results showed that the Pd surface was electronically modified leading to weaker adsorption of acetylene. Goodman et al. [79–81] showed that the Au bilayer structure on TiO_2 (110) surface causes significant changes to electronic properties. The partially reduced TiO_2 promoted the electron donation from $Ti^{\delta+}$ to Au, resulting in weaker CO bonding. Komaya *et al.* [82] found that covering Ru with amorphous TiO_x lead to lower Fischer-Tropsch (F-T) reaction activity and higher selectivity towards long-chain hydrocarbons. Lewandowski et al. [83] reported that Pt/Fe_3O_4 catalyst was promoted due to the encapsulation of Pt nanoparticles FeO (111) film over. CO adsorption was suppressed; while, the CO_2 production rate increased for CO oxidation.

Due to the complexity of metal oxide supported catalysts it has been difficult to quantify the metal-oxide interaction at the atomic level. [84] In this study we prepared Pt nanoparticles partially covered with TiO_x (or NbO_x) supported on SiO_2,

which display significantly higher propylene selectivity for propane dehydrogenation compared to SiO_2 supported Pt nanoparticles of similar size. Structural characterization by extended X-Ray absorption fine structure (EXAFS) and *in situ* synchrotron X-ray diffraction (XRD) confirm that the nanoparticles in the SMSI catalysts are monometallic Pt. Chemisorption of adsorbed CO confirms that ca. 80% of the nanoparticle surface was covered by the SMSI oxides. Electronic properties were measured by X-ray absorption near edge structure (XANES), *in situ* X-ray photoelectron spectroscopy (XPS), and resonant inelastic X-ray scattering (RIXS), confirming there are no significant changes in the energy of the Pt 5d valence orbitals. The SMSI oxides decrease the catalyst rate per gram for ethene hydrogenation and propane dehydrogenation with little change in the turnover rate (TOR). For the latter reaction, the Pt-SMSI oxide catalysts displayed higher olefin selectivity, which is suggested to result from a decrease in the number of ensemble sites responsible for hydrogenolysis.

3.3 Experimental

3.3.1 Materials

Davisil 636 silica gel (99%), $Pt(NH_3)_4(NO_3)_2$ (99.995%), titanium(IV) bis(ammonium lactato)dihydroxide (50% solution), niobium(V) ethoxide solution (99.95% trace metal basis), 200 proof ethyl alcohol were purchased from Sigma-Aldrich and used without further purification. The gases used for the catalytic testing were purchased from Indiana Oxygen Company, and the C_3H_8 is 5% balanced with N_2. The H_2 was also 5% balanced with N_2. Ultra-high purity gases were N_2 (99.999%) and He (99.98%). The gases used for XAS and XRD experiments were purchased from AirGas, Illinois, and all the gases were balanced with He.

3.3.2 Catalyst preparation

The monometallic Pt catalyst with 2 wt% Pt loading was prepared by a pH adjusted incipient wetness impregnation method (IWI) on SiO_2. $Pt(NH_3)_4(NO_3)_2$ was dissolved in 2 mL deionized water and ammonium hydroxide solution was added to adjust the pH to 11. The solution was added dropwise to Davisil Grade 636 silica (pore size = 60 Å, surface area = 480 m^2/g). This catalyst was then dried overnight at 125 °C and calcined at 225 °C for 3 h. Finally, the catalyst was reduced in 5% H_2/N_2 (100 mL/min) at 200 °C for 30 min and 550 °C for 30 min.

A series of Pt-Ti bimetallic catalysts supported on SiO_2 with a target Pt loading of 2 wt% were synthesized by a sequential incipient wetness impregnation method (IWI). Various amounts of titanium(IV) bis(ammonium lactato)dihydroxide solution (50% solution) (corresponding to 3, 6 and 8 wt% of Ti on SiO_2) were dissolved in deionized water and added dropwise to Davisil Grade 636 silica (pore size = 60 Å, surface area = 480 m_2/g). The obtained Ti/SiO_2 was dried overnight at 125 °C and calcined at 300 °C for 3 h. A second solution was made using 0.2 g of Pt(NH3)4(NO3)2 dissolved in 2 mL deionized water and 1.0 mL of 30% ammonium hydroxide solution was added to adjust the pH to 11. The solution was added dropwise to the obtained Ti/SiO_2 precursor. This catalyst was then dried overnight at 125 °C and calcined at 225 °C for 3 h. Finally, the catalyst was reduced in 5% H_2/N_2 (100 mL/min) at 200 °C for 30 min and 550 °C for 30 min.

A similar method was followed to synthesize Pt-Nb bimetallic catalysts supported on SiO_2 with a target Pt loading of 2 wt%. Various amounts of niobium(V) ethoxide solution (99.95% trace metal basis) (corresponding to 2, 4 and 8 wt% of Nb on SiO_2) were dissolved in 200 proof ethyl alcohol and added dropwise to Davisil Grade 636 silica (pore size = 60 Å, surface area = 480 m_2/g). The obtained Nb/SiO2 was dried overnight at 125 °C and calcined at 550 °C for 3 h. A second solution was made using 0.2 g of $Pt(NH_3)_4(NO_3)_2$ dissolved in 2 mL deionized water and 1.0 mL of 30% ammonium hydroxide solution was added to adjust the pH to 11. The solution was

added dropwise to the obtained Nb/SiO_2 precursor. This catalyst was then dried overnight at 125 °C and calcined at 225 °C for 3 h. Finally, the catalyst was reduced in 5% H_2/N_2 (100 mL/min) at 200 °C for 30 min and 550 °C for 30 min.

3.3.3 Scanning Transmission Electron Microscopy (STEM)

The STEM images were taken at Dalian Institute of Chemical Physics using JEM-ARM200F equipped with EDS analyzer (200 kV, probe Cs-corrector, <1Å spatial resolution). Samples were ground to fine powders and dispersed in isopropyl alcohol. One drop of the solution was added onto an ultrathin Carbon film-Au TEM ready grid (TedPella) and dried on a hot plate at 70 °C. STEM images were taken using the high angle annular dark field (HAADF) detector at 200 kV with signal collection angle of 68 174mrad. The particle size statistic was performed using the Image J program. A minimum of 200 particles were counted to obtain the size distribution for each catalyst. The electron energy loss spectroscopy (EELS) analysis was performed under 200kV on the ARM200F in the spectrum imaging mode using a converged beam in semi-angle of 40 mrad and core loss electrons for Pt-O edge, Ti L edge were collected from scattering angle up to 63 mrad over the energy range of 30 eV 542 eV. Since there is risk that for 2 nm particles the strong electron beam irradiation during EELS signal collection could result in particle reconstruction, particularly in the seriously charged environment of SiO_2-supported samples, we used single frame scanning to obtain EELS spectrum image to be able to capture the original structure before sample reconstructed. The relatively weak counts of energy loss electrons were only utilized to extract structural information of the Pt-Ti sample, rather than its electronic state, which has been more precisely analyzed through multiple X-ray absorption techniques in this work.

3.3.4 *In Situ* X-Ray Absorption Spectroscopy (XAS)

In Situ XAS experiments were performed at the 10-BM-B beamline at the Advanced Photon Source (APS), Argonne National Laboratory at the Pt L3 (11.564 keV) edge in transmission mode, with energy step of 0.3 eV and energy precision better than 0.1 eV. Catalysts were ground into a powder, pressed into a sample holder, and sealed in a sample cell with leak-tight kapton end caps. The sample cell was treated with 3.5% H_2/He for 30 minutes at 550 °C. The cell was cooled to room temperature in flowing He between each temperature exposure, sealed, and moved to the beamline to acquire data. The helium tank was connected to a gas purifier to reduce the possibility of O_2 exposure.

Each measurement was accompanied by simultaneous measurement of a Pt foil scan obtained through a third ion chamber for internal energy calibration. XAS data was fitted by using Demeter 0.9.25 software package. The edge energy was determined using the maximum of the first peak in the first derivative of the leading edge of the XANES spectrum. Least-squares fit in R-space of the k_2-weighted Fourier transform data from 2.7 to 12.0 Å^1 was used to obtain the EXAFS coordination parameters. The first shell was used to fit the EXAFS spectra. The amplitude reduction factor (S_0^2) was determined as 0.80 by fitting a reference spectrum of the Pt foil, and then it was used for fitting of all the other EXAFS spectra.

3.3.5 *In Situ* X-Ray Diffraction (XRD)

In Situ XRD measurements were performed at the 11-ID-C beamline at the APS, using X-rays of =0.1173 Å (105.715 keV) and data was acquired using a Perkin-Elmer large area detector. Samples were pressed into a self-supported pellet (¡ 2 mm thickness) and then loaded into a thermal stage. The cell was purged with He before a flow of 3.5% H_2/He at 100 ccm was introduced and the temperature was increased to 550°C. After diffraction measurements were completed at the reduction temperature, the cell was cooled to 35°C and a second diffraction measurement was obtained. A

second set of diffraction measurements were obtained at room temperature for each sample after being exposed to room temperature air, post-reduction. The background scattering of the empty cell and the cell with silica were obtained under the same conditions and subtracted from the XRD pattern. The diffraction patterns were collected as 2-D Scherrer rings and were integrated using Fit2D software to obtain 1-D diffraction patterns as scattering intensity vs. 2θ plots.

3.3.6 X-ray photoelectron spectroscopy (XPS)

Kratos Axis Ultra DLD spectrometer was used to collect XPS data. Monochromic Al K radiation (1486.6 eV) at pass energy of 20 and 160 eV for high-resolution and survey spectra was used, respectively. To achieve better resolution and to avoid non-homogeneous electric charge of non-conducting powder, a commercial Kratos charge neutralizer was used. 2%Pt/SiO_2, 2%Pt-8%Nb/SiO_2 and 2%Pt-6%Ti/SiO_2 catalysts were directly loaded onto a sample holder. Reduction was performed in a reaction chamber attached to the spectrometer by heating the samples to 550 °C in 5% H_2/Ar and holding for 30 minutes before cooling and evacuation. The XPS data were collected on reduced samples after they were transferred in vacuum (without exposure to air) to the spectrometer sample stage. XPS data were analyzed with CasaXPS software version 2313 Dev64 (www.casaxps.com). Curve-fitting was performed using Gaussian/Lorentzian peak shapes with a dampening parameter following a linear or Shirley background subtraction.

3.3.7 Resonant Inelastic X-ray Scattering (RIXS)

RIXS measurements were performed at the MR-CAT 10-ID beamline at the APS, Argonne National Lab. The catalyst was ground into a powder and pressed into a self-supported wafer in a stainless-steel sample holder at a 45°C angle to the incident beam. The sample holder was placed in a resistively-heated reactor cell through which

gases could be flowed. [85] Samples were reduced at 550 °C in 3% H2/He at 50 cc/min for 20 min and then cooled to 200 °C in the same gas flow for measurement.

A spectrometer based on the Laue geometry was used for RIXS measurements and has been described previously. [2] Briefly, a cylindrically bent silicon crystal analyzer (ρ = 350 mm, Si thickness 55 μm, [100] wafer normal, $\langle 133 \rangle$ reflection) was used to select the L5 emission line of Pt. Fluorescence X-ray were detected using a Pilatus 100k pixel area detector. Soller slits between the analyzer and detector lowered the background signal by absorbing unreflected X-rays. The entire emission spectrum was collected at each incident energy; both the analyzer and detector positions were fixed during measurements.

3.3.8 CO chemisorption

CO chemisorption was performed on a Micromeritics ASAP 2020 chemisorption instrument. A U-shaped quartz reactor was used and approximately 0.1 g of catalysts was loaded in it. 5% H_2/He was introduced into the reactor at 50 ccm to reduce the catalysts at 550 °C or 225 °C and cooled to RT. He was flushed for 30 min before evacuation and measurements. The catalyst dispersion was obtained by difference analysis in the chemisorption curve. A stoichiometry of CO: Pt = 1: 1 was assumed to calculate the dispersion for the catalysts.

3.3.9 Propane dehydrogenation and ethylene hydrogenation catalytic performance tests

Catalyst performance tests were performed in a fixed bed, quartz reactor with 3/8-inch OD. A K-type thermocouple (O.D. = 3.2 mm) was placed in the center of the catalyst bed to measure the temperature of the catalyst. A furnace connected to a controller was used to maintain the desired temperature. The weight of the catalyst (particle size 250-500 μm) loaded into the reactor ranged from 10 mg to 200 mg to vary the initial conversion and was diluted with silica to reach a total of 1

g. Prior to the reaction, the catalyst was reduced for 30 minutes at 550°C under 100 ccm 5% H_2/N_2. For propane dehydrogenation, the reaction was performed in 2.5% C_3H_8, 2.5% H_2, balanced with N_2 at 550°C. For ethylene dehydrogenation, the catalysts were pre-reduced at 550°C and the reaction was performed in 2% C_2H_4, 2% H_2, balanced with N_2 at 30°C. The products were analyzed with a Hewlett Packard 6890 Series gas chromatograph using a flame ionization detector (FID) with a Restek Rt-Alumina Bond/Na_2SO_4 GC column (30 m in length, 0.32 mm ID, and 0.5 μm film thickness).

3.4 Results

3.4.1 Catalyst Synthesis

Catalysts were prepared by addition of Ti and Nb oxides onto SiO_2 followed by addition and reduction of Pt to produce nanoparticles (NP) of approximately the same 2 nm size. The SMSI oxides were added by incipient wet impregnation of organometallic precursors (titanium(IV) bis(ammonium lactato)dihydroxide in H_2O and niobium ethoxide in ethanol), followed by dring and cacination at 550°C to remove the organic ligands. The titanium loading were 3, 6 and 8 wt%, and the niobium loadings were 4 and 8 wt%. To the SMSI-SiO_2 supports and unmodified SiO_2, $Pt(NH_3)_2(NO_3)_2$ dissolved in water with the pH adjusted to approximately 11 was impregnated, dried, calcined at 225°C. The catalysts were reduced at 200 and 550°C. The Pt loadings were 2wt%.

3.4.2 CO chemisorption

The Pt dispersions of the catalysts were determined by CO chemisorption. Dispersions after reduction at 250 ° and 550 ° are shown in Table 3.1. After reduction at 250 °, the Pt-Ti/SiO_2 (45-52%) and Pt-Nb/SiO_2 (53-57%) dispersions were similar to Pt/SiO_2 (55%) suggesting all catalysts have NPs of approximately the same

size. After reduction at 550 °, however, Pt-Ti/SiO_2 and Pt-Nb/SiO_2 dispersions decreased significantly, ca. 7-12%, much smaller than that of 2Pt/SiO_2 (45%). The low chemisorption capacity after 550 ° reduction is characteristic of an SMSI effect of Pt NPs supported on TiO_2 and Nb_2O_5. [86]

Table 3.1.
Summary of CO chemisorption results

Sample Name	% Dispersion 250 °C reduction	% Dispersion 550 °C reduction
2Pt/SiO_2	55	45
2Pt-3Ti/SiO_2	52	12
2Pt-6Ti/SiO_2	50	10
2Pt-8Ti/SiO_2	45	8
2Pt-4Nb/SiO_2	57	9
2Pt-8Nb/SiO_2	53	7

3.4.3 TEM

The STEM average particle size distributions of 2Pt/SiO_2, 2Pt-6Ti/SiO_2 and 2Pt-8Nb/SiO_2 after reduction at 550 °C were 2.5, 1.7 and 1.5 nm, respectively (Table 3.2). The microstructure of 2Pt-6Ti/SiO_2 was studied via STEM and EELS methods as shown in Figure 3.1. The nanoparticles having an average size of 1 2nm were evenly dispersed on the SiO_2 support (Figure 3.1(A)). These nanoparticles are single crystal in nature, without any shape anisotropy, as demonstrated in the magnified HAADF image (Figure 3.1(B)). The primary structure matrix of the particles coincides quantitatively with the lattice pattern of metallic platinum (Figure 3.1(C)) and slight compressive strain exists that is ascribed to the small size. Few Pt single atoms disperse near to the particle surface (orange circles in Figure 3.1(C)-3.1(D)). The EELS analysis on the elemental distribution further confirms the particle matrix is metallic Pt; while, Ti species (or TiO_x) are widely dispersed over the whole particle, forming a Ti@Pt core-shell configuration.

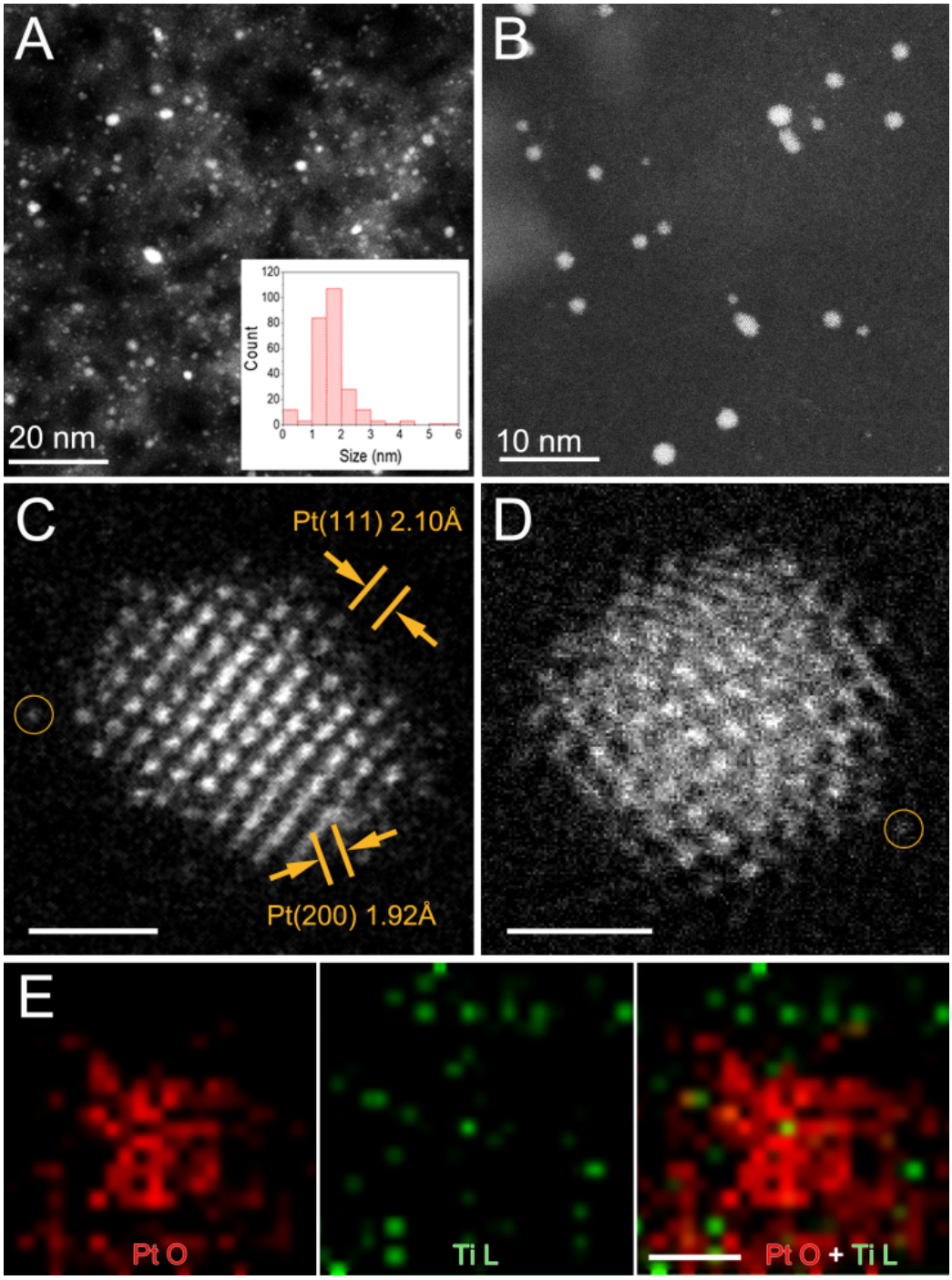

Fig. 3.1. (A) Representative low magnified dark-field STEM image of 2Pt-6Ti/SiO_2 in large field of view, inset the particle size statistic; (B) The magnified HAADF image disclosing the single-crystal nature of PtTi particles; (C) The high resolution HAADF image of one PtTi particle showing similar structure with platinum, suspened Pt single atom is marked with orange circle; (D) Another PtTi nanoparticle and its corresponding elemental distribution (E) as revealed via EELS spectrum imaging. Scale bar in (C)-(E), 1 nm.

3.4.4 *In Situ* X-Ray Absorption Spectroscopy (XAS)

The Pt L_3 edge X-ray absorption near edge structure (XANES) and extended X-ray absorption fine structure (EXAFS) spectra of 2Pt/SiO_2, 2Pt-6Ti/SiO_2 and 2Pt-8Nb/SiO_2 are shown in Figure 2. After 550°C reduction, 2Pt/SiO_2 had an edge energy of 11564.0 eV, identical to Pt foil and consistent with monometallic Pt nanoparticles. For 2Pt-6Ti/SiO_2, the shape of the XANES spectra was similar to 2Pt/SiO_2; while, the XANES of 2Pt-8Nb/SiO_2 had a broader white line compared with 2Pt/SiO_2 due a slightly smaller particle size. The edge energy, however, was identical to that of 2Pt/SiO_2 (Table 3.2).

The Pt L_3 EXAFS of 2Pt/SiO_2, shows three main peaks between 2-3 Å in the k^2-weighted magnitude of the Fourier transform, Figure 3.2 (B), which is typical for scattering in metallic Pt nanoparticles. 2Pt-6Ti/SiO_2 and 2Pt-8Nb/SiO_2 catalysts also showed similar peaks; while, the small size of the peaks suggests formation of slightly smaller nanoparticles.The k space and k2-weighted Fourier transformation imaginary part spectra of the SMSI catalysts are also similar to Pt/SiO_2 (Figure 3.3), and suggest that the SMSI catalysts are monometallic Pt nanoparticles. The EXAFS of the three catalysts were fit with a single Pt-Pt path and the results are shown in Table 3.1. The bond distance of the 2Pt/SiO_2 catalyst was 2.73 Å, and the coordination number was 8.9. The Pt nanoparticle size can be estimated from the coordination number, and is 2.5 nm for Pt/SiO_2, consistent with the STEM. [87] The bond distance of 2Pt-6Ti/SiO_2 and 2Pt-8Nb/SiO_2 was 2.71, slightly shorter than 2Pt/SiO_2. The coordination numbers of 2Pt-6Ti/SiO_2 and 2Pt-8Nb/SiO_2 are 7.8 and 6.6, respectively. The estimated particle sizes are given in Table 3.1 and are consistent with those determined by STEM.

3.4.5 *In situ* X-ray diffraction

In situ synchrotron X-ray diffraction (XRD) was used to confirm the crystalline phase of 2Pt-6Ti/SiO_2 and 2Pt-8Nb/SiO_2. Diffraction patterns were obtained at

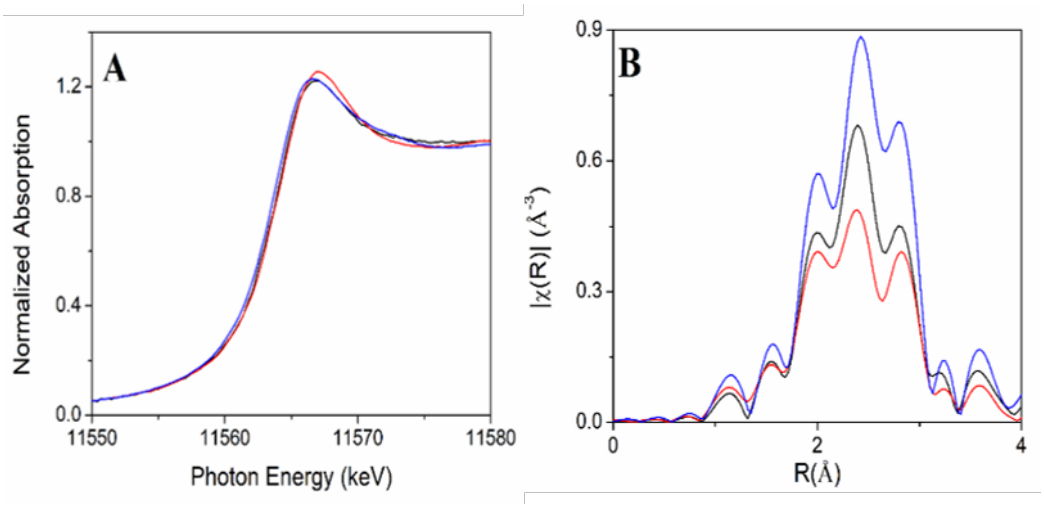

Fig. 3.2. (A) Pt L_3 edge XANES spectra of $2Pt/SiO_2$ (blue), 2Pt-6Ti/SiO_2 (black) and 2Pt-8Nb/SiO_2 (red). (B) Pt L_3 edge EXAFS spectra of $2Pt/SiO_2$ (blue), 2Pt-6Ti/SiO_2 (black) and 2Pt-8Nb/SiO_2 (red).

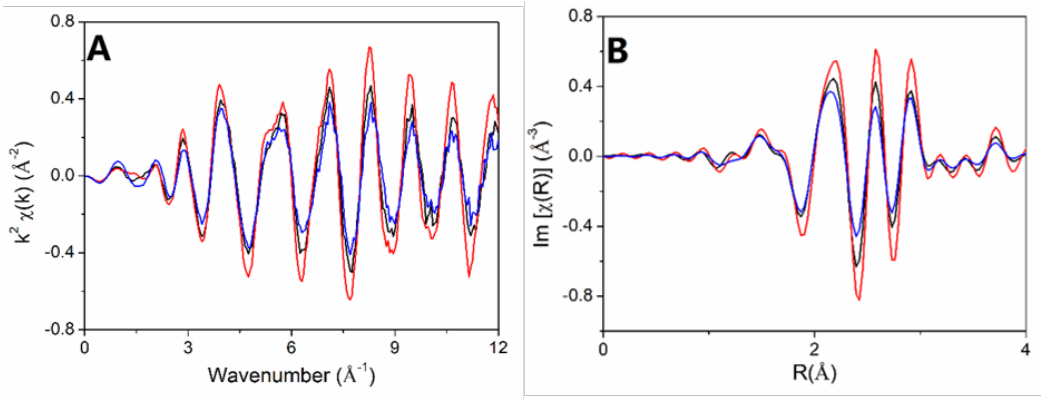

Fig. 3.3. Pt L_3 edge EXAFS spectra: A) k space, and B) R space FT imaginary part. $2Pt/SiO_2$ (red), 2Pt-6Ti/SiO_2 (black) and 2Pt-8Nb/SiO_2 (blue).

room temperature after *in situ* reduction at 550 °C. The patterns were obtained by subtracting the scattering of the empty cell, the silica support, and the gases in the X-ray path from the full diffraction patterns of the catalyst. The energy of the synchrotron X-ray beam is 10571.5 eV, thus, the diffraction pattern occurs at

Table 3.2.
XANES edge energy and EXAFS fitting parameters for the catalysts

Sample Name	XANES energy (eV)	CN_{Pt-Pt}	R (Å)	^{2} (Å^2)	Est. XAS size (nm) [87]	STEM size (nm)
2Pt/SiO_2	11564.0	8.9±0.5	2.74±0.02	0.007	2.5	2.5
2Pt-6Ti/SiO_2	11564.0	7.8±0.3	2.71±0.03	0.008	1.8	1.7
2Pt-8Nb/SiO_2	11564.0	6.6±0.2	2.71±0.03	0.008	1.1	1.5

smaller 2 Theta angles compared to lab XRD patterns. The 2 peak of the (200) plane of FCC Pt, for example, is 3.43° rather than 46.0° in the standard lab XRD (Cu k = 8.04 keV). 2Pt/SiO_2 showed peaks at 2θ of 2.980°, 3.430°, 4.881°, and 5.712° corresponding to the (111), (200), (220) and (311) planes of the Pt FCC structure, respectively. For 2Pt-6Ti/SiO_2 and 2Pt-8Nb/SiO_2, there were similar cubic patterns at the same 2θ. The patterns of the 2Pt-6Ti/SiO_2 and 2Pt-8Nb/SiO_2 catalysts, however, were broader than 2Pt/SiO_2. This is due to the slightly smaller particle size of the nanoparticles, which is consistent with the EXAFS and STEM results, and suggests that 2Pt-6Ti/SiO_2 and 2Pt-8Nb/SiO_2 formed monometallic Pt FCC structures with small particle sizes.

3.4.6 *In situ* XPS

In situ XPS measurement was performed on 2Pt/SiO_2, 2Pt-6Ti/SiO_2 and 2Pt-8Nb/SiO_2 reduced at 550 °C and measured without exposure to air. The Pt 4f region consists of two components corresponding to Pt $4f_{7/2}$ and Pt $4f_{5/2}$, respectively. The Pt NP's on 2Pt/SiO_2 showed Pt $4f_{7/2}$ and $4f_{5/2}$ binding energies of 71.7 eV and 75.0 eV respectively, which are assigned to metallic Pt. The Pt $4f_{7/2}$ peak of 2Pt-6Ti/SiO_2 and 2Pt-8Nb/SiO_2 were at the same energy as 2Pt/SiO_2, indicating that Pt in 2Pt-6Ti/SiO_2 and 2Pt-8Nb/SiO_2 were in metallic state, and there was no significant electronic interaction between Pt and SMSI oxides.

Ti 2p XPS spectra of 2Pt-3Ti/SiO_2 and 2Pt-6Ti/SiO_2 catalyst were collected to analyze the chemical states of titanium (Figure 3.6). Curve fitting gives two species

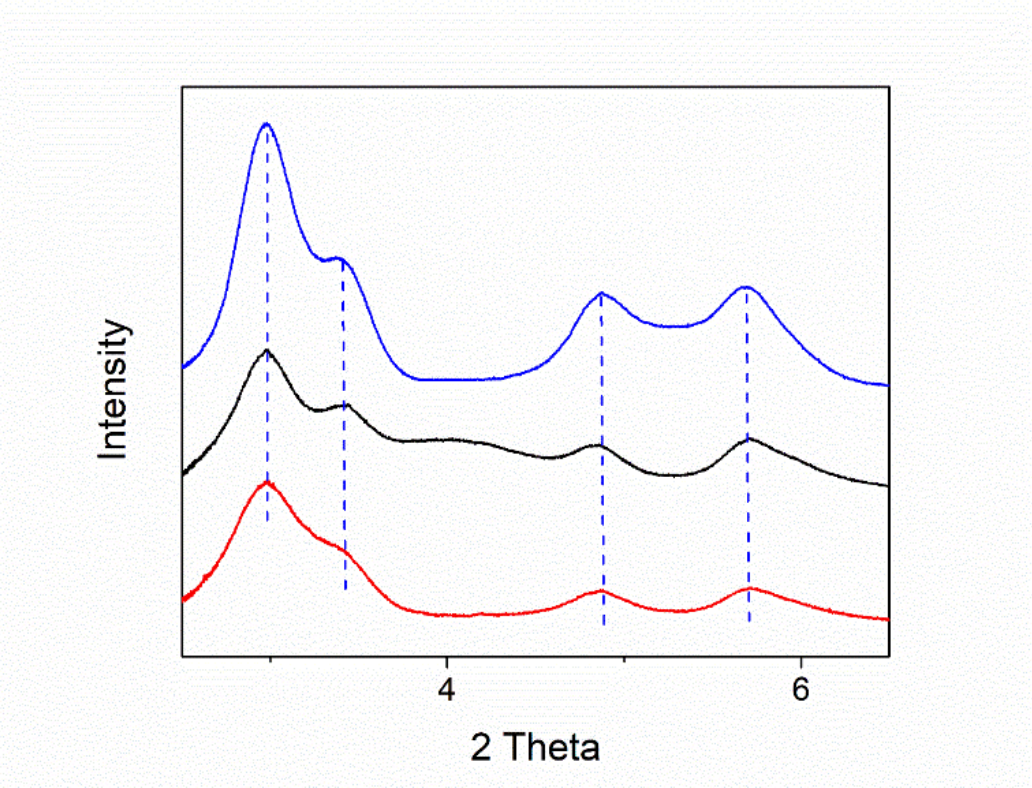

Fig. 3.4. *In situ* XRD patterns taken at 35 °C after reduction at 550 °C. 2Pt/SiO_2 (blue), 2Pt-6Ti/SiO_2 (black) and 2Pt-8Nb/SiO_2 (red).

in both catalysts with different ratios. In 2Pt-6Ti/SiO_2, the major Ti $2p_{3/2}$ peak at 459.5 eV is Ti^{4+} (red solid line), which is assigned to the excessive TiO_2. The smaller peak at 458.8 eV (blue line) indicates a lower oxidation state, which might be associated with the TiOx overlayer on Pt surface. The percentages of Ti^{4+} and Ti^{x+} ($x \leq 4$) are 83.2% and 16.8%, respectively. In 2Pt-3Ti/SiO_2, the percentages of these two species are 43.8% and 56.2%.

Nb 3d XPS spectrum of 2Pt-8Nb/SiO_2 (Figure 3.7) catalyst shows the presence of Nb^{5+} with the $3d_{5/2}$ peak at 208.0 eV and the $3d_{3/2}$ peak at 210.8 eV. Since the loading of Nb is 8%, which is much higher than the Pt loading, excessive Nb_2O_5 contributes mostly to Nb spectrum.

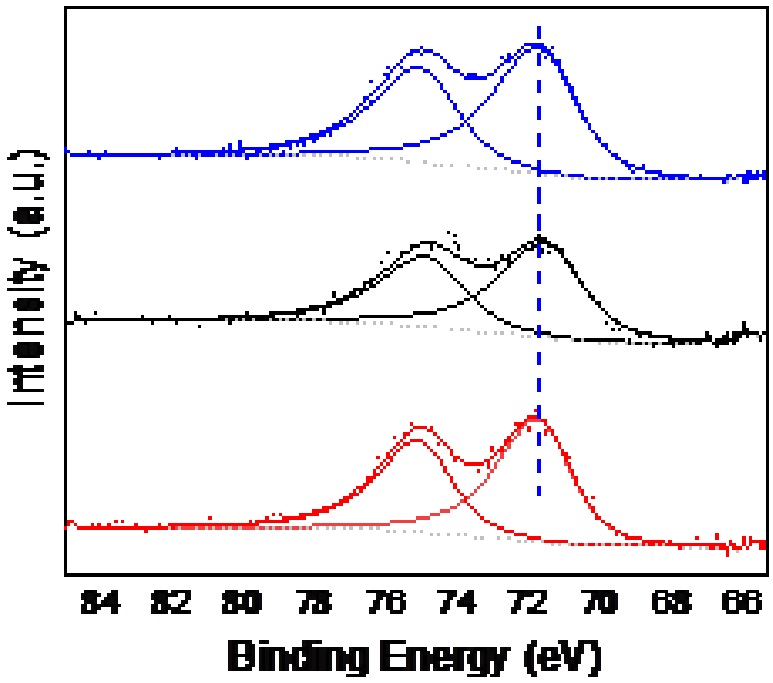

Fig. 3.5. Pt 4f XPS spectra of $2Pt/SiO_2$ (blue), $2Pt\text{-}6Ti/SiO_2$ (black) and $2Pt\text{-}8Nb/SiO_2$ (red). Dots: experimental data; grey dashed line: background; solid line: fitted data.

3.4.7 Resonant Inelastic X-ray Scattering (RIXS)

In situ RIXS spectra for $2Pt/SiO_2$ and $2Pt\text{-}8Nb/SiO_2$ were collected in order to measure the energy difference, or energy transfer (ΔE), between the filled and unfilled Pt 5d states. The energy transfer is the difference in energy of the Pt L_3 XANES absorption and Lβ_5 emission energies, which were obtained as a function of incident photon energy. [88] The RIXS spectra for $2Pt/SiO_2$ and $2Pt\text{-}8Nb/SiO_2$ are presented in Figure 3.8 as two-dimensional contour plots that show the energy transfer as a function of incident photon energy. For $2Pt/SiO_2$, the red region represents the maximum RIXS intensity, which occurs at incident energy at 11564.5 eV with ΔE = 3.0 eV. The position of maximum intensity and energy transfer of $2Pt\text{-}8Nb/SiO_2$

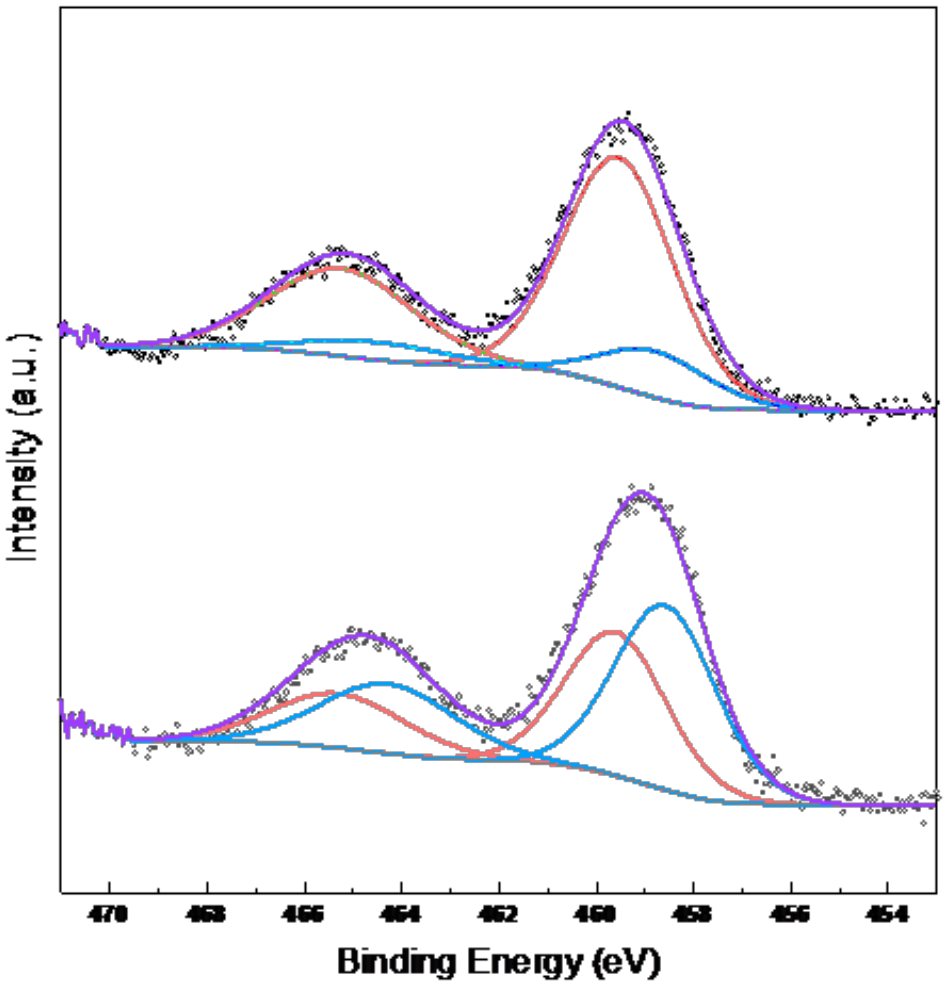

Fig. 3.6. Ti 2p XPS spectra of 2Pt-3Ti/SiO_2 (lower) and 2Pt-6Ti/SiO_2 (upper) catalysts. Black dots: experimental data; dash lines: background; solid lines: fitted data.

are similar to Pt/SiO_2. Since the energy of the XANES of both catalysts are also identical, the RIXS indicates there is no change in the energy of the filled Pt 5d states, which are responsible for catalysis, due to interaction with the SMSI oxide.

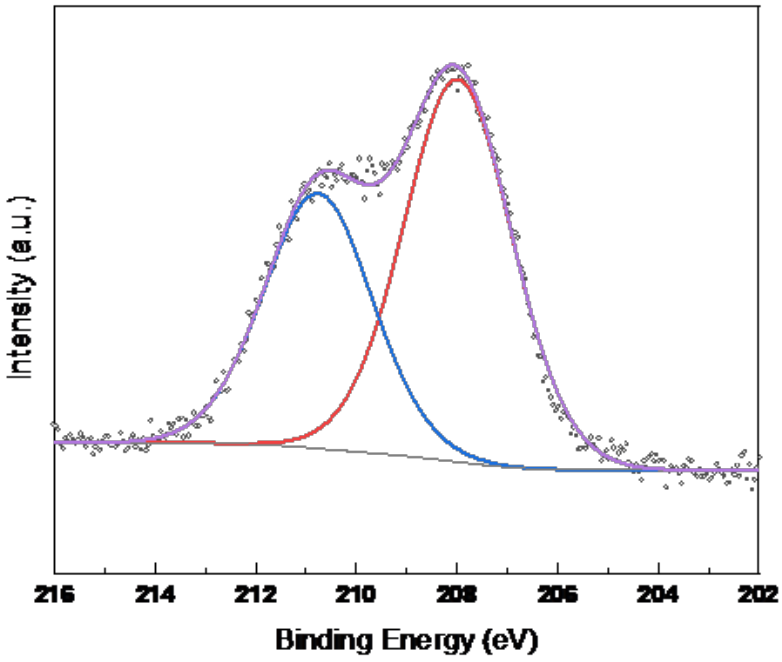

Fig. 3.7. Nb 3d XPS spectrum of 2Pt-8Nb/SiO_2 catalyst. Black dots: experimental data; grey line: background; red line: Nb $3d_{5/2}$ peak, blue line: Nb $3d_{3/2}$ peak; purple line: sum curve.

3.4.8 Ethylene hydrogenation

The effect of SMSI on catalytic performance was determined for ethylene hydrogenation. The catalysts were reduced at 550 °C and the hydrogenation reactions were performed at 30°C. The relation between the reciprocal space velocity and conversion for 2Pt/SiO_2, 2Pt-6Ti/SiO_2 and 2Pt-8Nb/SiO_2 catalysts are shown in Figure 3.9.

The rates per mol of catalyst for 2Pt/SiO_2, 2Pt-6Ti/SiO_2 and 2Pt-8Nb/SiO_2 are 1.26 mol/(s*mol Pt), 0.26 mol/(s*mol Pt) and 0.36 mol/(s*mol Pt), respectively. The turnover rates (TOR), based on CO chemisorption capacity (Table 3.1), were similar, 2.8, 2.6 and 2.1 s^{-1}, respectively, and were consistent with the previous literature. [89–91]

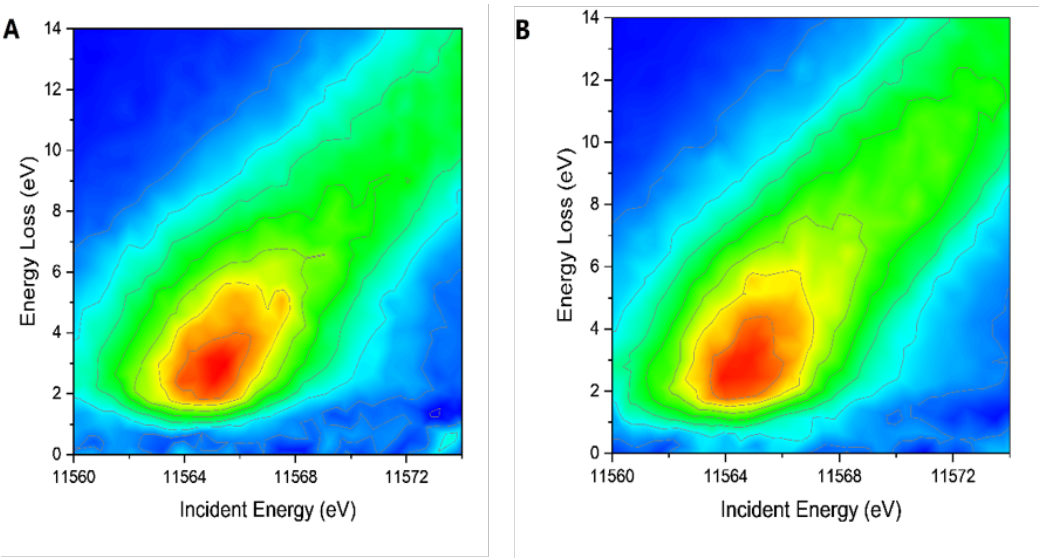

Fig. 3.8. RIXS planes for A) 2Pt/SiO_2 and B) 2Pt-8Nb/SiO_2.

3.4.9 Propane dehydrogenation

The catalytic performance was also determined for propane dehydrogenation at 550 °C. Propane was co-fed with hydrogen to increase the hydrogenolysis selectivity to light alkanes, e.g., ethylene, ethane and methane, and provides a more severe test of the catalysts' olefin selectivity. Initial selectivity, i.e., selectivity free of coke, and conversion are shown in Figure 3.10 and Table 3.3.

The propylene selectivity for 2Pt/SiO_2 at 10% conversion was ca. 70%. The selectivity also decreased with increasing conversion. The propylene selectivity for 2Pt-6Ti/SiO_2, however, was near 95% at 10% conversion and only decreased slightly with increasing conversion (90% selectivity at 25% conversion). For 2Pt-8Nb/SiO_2, the selectivity at 10% conversion was about 90% conversion and decreased slightly with increasing conversion (87% selectivity at 30% conversion). For different Ti and Nb loadings, shown in Table 3.3, the propylene selectivities were very similar to those in Figure 3.10, suggesting the catalytic performance was not sensitive to the SMSI oxide loading.

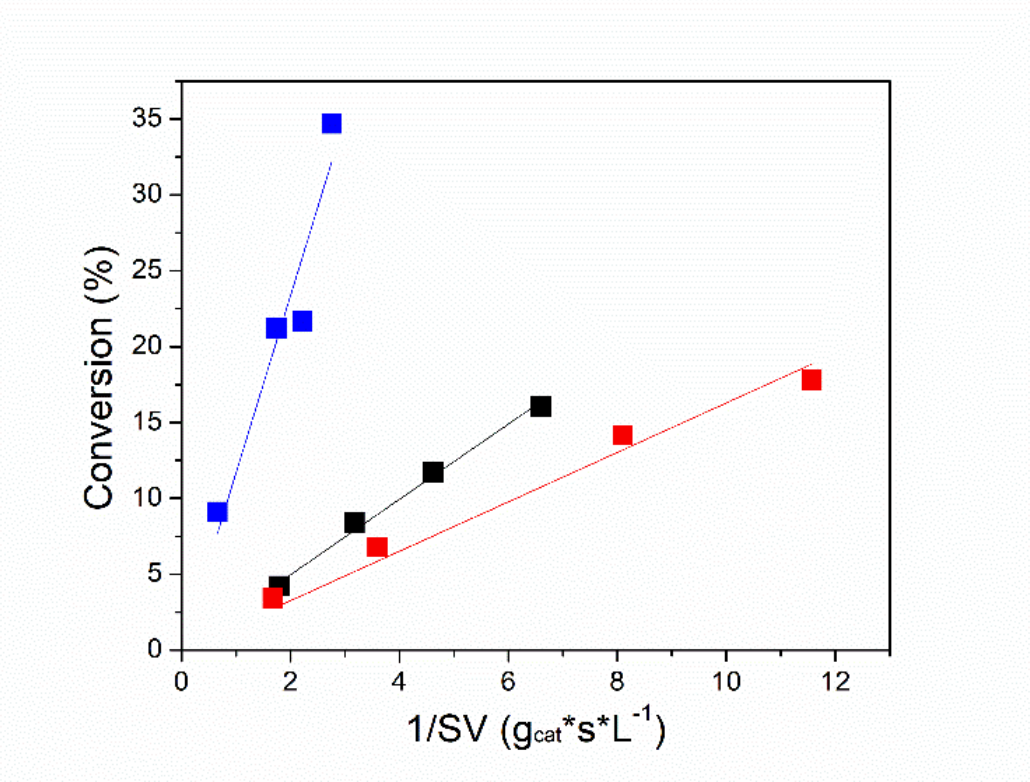

Fig. 3.9. Ethylene conversion at different space velocities of $2Pt/SiO_2$ (blue), $2Pt\text{-}3Ti/SiO_2$ (black) and $2Pt\text{-}8Nb/SiO_2$ (red) reduced at 550 °C. Reaction conditions: 30 °C, 2 % C_2H_6 + 2 % H_2 balanced with N_2.

Initial rates of the catalysts per mole Pt are shown in Table 3.3. Initial rates of $Pt\text{-}Ti/SiO_2$ and $Pt\text{-}Nb/SiO_2$ catalysts were 3-4 times lower than $2Pt/SiO_2$. The TORs under differential conditions are also given in Table 3. Initial TORs for $2Pt/SiO_2$, $2Pt\text{-}6Ti/SiO_2$ and $2Pt\text{-}8Nb/SiO_2$ catalysts, were 0.17 s^{-1}, 0.22 ss^{-1} and 0.19 ss^{-1}, respectively. The initial TORs of $Pt\text{-}Ti/SiO_2$ and $Pt\text{-}Nb/SiO_2$ catalysts were similar to those of $2Pt/SiO_2$, suggesting that the intrinsic TOR of $Pt\text{-}Ti/SiO_2$ and $Pt\text{-}Nb/SiO_2$ are the same as $2Pt/SiO_2$.

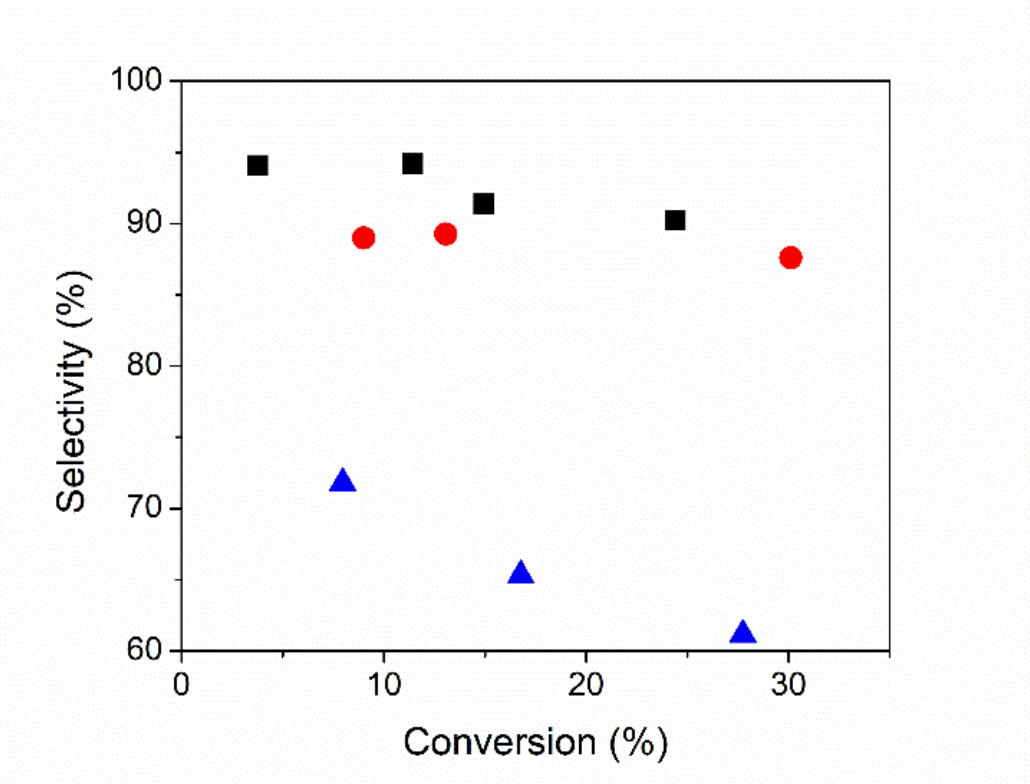

Fig. 3.10. Propylene selectivity at different conversions of $2Pt/SiO_2$ (blue triangle), $2Pt\text{-}6Ti/SiO_2$ (black square) and $2Pt\text{-}8Nb/SiO_2$ (red circle). Reaction conditions: 550 °C, 2.5 % C_3H_8 + 2.5 % H_2 balanced with N_2.

3.5 Discussion

3.5.1 Electronic and geometric effects of Pt-Nb/SiO_2 and Pt-Ti/SiO_2

The structure and catalytic properties of noble metals on SMSI oxides have been extensively studied. The strong metal-support interaction often leads to stabilization of small particle size, reduction of H_2 and CO chemisorption and altered catalytic properties. [75] Coverage of the NP by the support can lead to higher or lower rate and altered selectivity. The latter are often suggested to be due to changes in the electronic properties of the metal NPs, often described as electron transfer to metal from a partially reduced support oxide. [92,93] For example, the XPS Pt $4f_7/2$ peak is

Table 3.3.
Summary of catalytic results for propane dehydrogenation

Sample Name	C_3H_6	Rate (mol/(s*mol catalyst))	Initial Turnover Rate ($s^{-1)}$)
$2Pt/SiO_2$	70	0.077	0.17
$2Pt\text{-}3Ti/SiO_2$	93	0.019	0.16
$2Pt\text{-}6Ti/SiO_2$	93	0.022	0.22
$2Pt\text{-}8Ti/SiO_2$	94	0.017	0.22
$2Pt\text{-}4Nb/SiO_2$	88	0.025	0.28
$2Pt\text{-}8Nb/SiO_2$	91	0.013	0.19

Reaction conditions: 550 °C , 2.5 % C_3H_8 + 2.5 % H_2 balanced with N_2; selectivity and TOR calculated at 10% C_3H_8 conversion. TOR calculated based on C_3H_8 conversion rate.

shifted from 71.0 eV (Pt) to 70.2 eV (Pt/TiO_2) suggesting that Pt interacts with the TiO_2 support, which provided electrons to the surface of the nanoparticles; i.e., Pt gains electrons from the partially reduced support. Ruppert *et al.*, demonstrated that addition of ZrO_2 to Pt/TiO_2 improved the selective hydrogenation of crotonaldehyde by controlling the extent of SMSI coverage after reduction at 500 °C. Addition of ZrO_2 appears to inhibit full coverage by TiO_x leading to higher rates. For these catalysts, the Pt $4f_7/2$ binding energy was very similar to Pt, e.g., 71.0 eV. [94] The improved catalyst selectivity was ascribed to the formation of interfacial active sites of Pt NPs with TiO_x SMSI overlayers without full coverage and complete loss of activity.

Several studies of SMSI have shown evidence for electronic modification of the group VIII metal due to alloying. Haller et al. observed that for Rh/TiO_2 there is a shift in the Rh K-edge XANES thought to be due to formation of intermetallic Rh_3Ti alloy. EXAFS also showed that there was Rh-Ti scattering with the bond distance at 2.56 Å. [95, 96] Liu *et al.* showed for Pt/FeO_x that although the Pt nanoparticles were partially encapsulated, the catalytic activity was high for CO oxidation at 27 °C with TOR of 0.15 $s^{-}1$ due to dual reaction sites (Pt for CO adsorption and reaction and FeOx for O_2 adsorption and activation. [74] For Pt/FeOx and Pd/FeOx shifts to lower energy in the 4f and 3d XPS, respectively, suggested that there was electron

transfer from the FeOx to the noble metals increasing the electron density of the NPs. [74] In other studies, Fe has been shown to form alloys with Pt and Pd after reduction at 550°C. [27, 97] Thus, the electronic effect attributed to SMSI by FeO_x may be due to alloy formation, rather than by the interaction with the Fe oxide over layers.

In this study, TEM, XAS and XRD show that these catalysts are monometallic Pt NPs, of approximately the same size, ca. 2 nm ± 0.5 nm. In addition, after reduction at 550°C, TEM, EELS, CO chemisorption and catalytic rates showed that the Pt nanoparticles were partially covered by the metal oxides similar to previous SMSI studies. CO chemisorption showed that 80% of the Pt nanoparticles' surface was covered by the SMSI oxides. For example, for 2Pt-6Ti/SiO_2 the dispersion after reducing at 250 °C (without SMSI) was 50% while after 550 °C the dispersion was 10%. This reduced the fraction of exposed, surface Pt atoms and led to lower activity per gram of catalyst for ethylene hydrogenation and propane dehydrogenation. The TORs of the Pt/SiO_2 and Pt-Ti/SiO_2 and Pt-Nb/SiO_2 catalysts, however, were very similar suggesting that there was no intrinsic change in the catalytic properties of Pt. While the TORs for propane dehydrogenation for Pt-Ti/SiO_2 and Pt-Nb/SiO_2 were similar to Pt/SiO_2, the olefin selectivities are significantly improved for the former.

SMSI oxides are often thought to transfer electron density from the partially reduced support to the metal NPs altering their catalytic performance. The electronic properties of Pt in the Pt-Ti/SiO_2, Pt-Nb/SiO_2 and Pt/SiO_2 were investigated by *in situ* XANES, XPS and RIXS. All catalysts had the same *in situ* XPS binding energies, for example, the Pt $4f_{7/2}$ was 71.7 eV. Similarly, the *in situ* XANES edge energy of all catalysts were identical (11564.0 eV) and the same as Pt foil. While XPS and XANES spectra indicate no significant electronic changes, these are indirect measurements of the Pt 5d orbital energies, which are responsible for catalysis. The energy transfer determined by RIXS when combined with the XANES energies gives the energy of the Pt 5d filled states, which are responsible for the chemistry. Consistent with the XANES and XPS spectra, the energies of the Pt 5d filled orbitals are the same for

2Pt/SiO_2 and 2Pt-8Nb/SiO_2. Thus, partial coverage of Pt NPs by TiO_x and NbO_x SMSI overlayers does not lead to a change in the energy of the Pt 5d filled orbitals suggesting that the changes in propylene selectivity are not due to change in the chemical nature of the Pt NPs.

3.5.2 Structure–function relationship of Pt-Nb/SiO_2 and Pt-Ti/SiO_2 catalysts: the promotion effect of Nb and Ti

Dehydrogenation is a structure insensitive reaction, requiring individual atoms for catalytic activity. However, hydrogenolysis is a structure sensitive reaction, which requires Pt ensembles as active sites. [98] High propylene selectivity in Pt_3Mn, [63] Pt3Co, [38] Pt_3Cr, [35] Pt_3V [88] and Pt_1Zn_1 [42] intermetallic alloys has been proposed to be due to isolated or small ensemble Pt and Pd sites. Pt-Ti/SiO_2 and Pt-Nb/SiO_2 had propylene selectivity 90%, similar to alloy catalysts. [27,62,64,69,99]

While *in situ* EXAFS and XRD showed that these SMSI catalysts did not form alloys, the high olefin selectivity suggests that the higher selectivity is likely due to a change in the average surface ensemble size. SMSI of supported noble metal catalysts are known to lower the rates of alkane hydrogenolysis. For example, Bracery *et al.* have shown that SMSI leads to lower ethane hydrogenolysis rates on Pd/TiO_2. [100] Similar suppression of hydrogenolysis selectivity was observed for NiMo/SiO_2 catalyst for HDO of m-Cresol. [27] For the latter, Ni was also shown not to alloy with Mo. It seems likely, therefore, that the improved olefin selectivity of Pt-Ti/SiO_2 and Pt-Nb/SiO_2 results from the partial coverage of 1-2 nm nanoparticles leaving few surface ensembles capable of hydrogenolysis. The few remaining and exposed Pt atoms remain active for dehydrogenation. Thus, the higher dehydrogenation selectivity appears to result from selective suppression of structure sensitive hydrogenolysis reactions. The loss of surface sites does lead to lower rates per total mole of Pt, but the intrinsic catalytic properties of Pt for alkane dehydrogenation are unchanged.

The results of this study suggest that changes in catalytic performance, i.e. lower rate but higher olefin selectivity, is mainly due to the geometric influence of TiO_2 and Nb_2O_5 overlayers partially covering the Pt surface. The few exposed sites (Figure 3.8), which are about 20% of the surface atoms, lead to small Pt ensembles and low hydrogenolysis rates, consistent with a previous SMSI studies. [101] The changes in selectivity result from suppression of structure sensitive reactions while the remaning sites are catalytic for structure insensitive reactions.

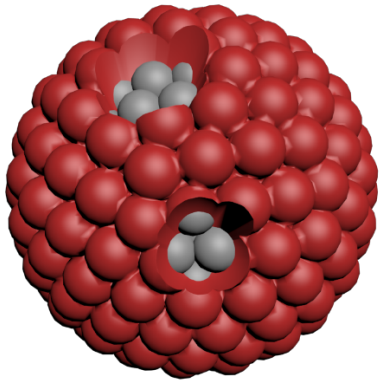

Fig. 3.11. Schematic model of geometric structure of the Pt-Ti and Pt–Nb catalysts (red atoms representing SMSI oxide and grey atoms representing exposed Pt).

3.6 Conclusions

In summary, Pt-Ti/SiO_2 and Pt-Nb/SiO_2 catalysts showed SMSI behaviors consistent with previous studies on TiO_2 and Nb_2O_5. The catalysts showed no change in energy of the Pt 5d valance orbitals responsible for catalysis. Partial covering of the catalytic surface by the SMSI oxides resulted in lower activity per gram of Pt, but similar TORs, for ethylene hydrogenation and propane dehydrogenation. The

olefin selectivity for propane dehydrogenation, however, was significantly higher on the SMSI catalysts and is thought to be due to few hydrogenolysis ensembles on the SMSI oxide covered Pt nanoparticles.

3.7 Acknowledgement

The authors acknowledge support from the National Science Foundation under award CBET-1804712 and the National Science Foundation under Cooperative Agreement No. EEC-1647722. Use of the Advanced Photon Source was supported by the U.S. Department of Energy Office of Basic Energy Sciences under contract no. DE-AC02-06CH11357. MRCAT operations, beamlines 10-BM and 10-ID, are supported by the Department of Energy and the MRCAT member institutions. The authors also acknowledge the use of beamline 11-ID-C.

4. STRONG METAL-SUPPORT INTERACTION (SMSI) OF PT/CEO2 UNDER EXTREME CONDITIONS AND ITS EFFECT ON PROPANE DEHYDROGENATION

This chapter is reproduced from Zhu Chen, Johnny, et al."Strong Metal-Support Interaction (SMSI) of Pt/CeO_2 under extreme conditions." submitted to Catalysis Today.

4.1 Abstract

Strong metal-support interactions (SMSI) has been exploited to modify reaction selectivity and activity. In this study, we show the SMSI of Pt/CeO2 happens after reducing at 975 °C. X-ray absorption fine structure (EXAFS) and transmission electron microscopy (TEM) shows the formation of 15 nm monometallic Pt nanoparticles partially covered by CeO_2. X-ray absorption near edge structure (XANES) showed little changes on the electronic structure. The catalytic activity per mol of Pt for ethylene hydrogenation was lower due to fewer exposed Pt sites and bigger particle size. The propylene selectivity of propane dehydrogenation was 95 %, which suggested that smaller ensemble sizes suppressed alkane hydrogenolysis.

4.2 Introduction

Investigation of supported metal catalysts mostly focuses on optimizing the composition or geometry of the metal sites to improve the catalytic properties of the catalysts. [102–104] On the other hand, strong metal-support interaction (SMSI) has been also exploited to modify the reaction selectivity and increase the rates. Tauster et al. found that after high temperature reduction of group VIII NPs supported on oxides like TiO_2, Nb_2O_5 and FeO_x, the CO and H_2 chemisorption is strongly suppressed; while NPs reduced at low temperature displayed normal chemisorption

behavior. [71, 74, 75, 105] It generally thought that these SMSI oxides are partially reduced at high temperature where the sub-stoichiometric oxides migrate and encapsulate metal NPs blocking the catalytic surface. The SMSI overlayers are often suggested to change the geometric and electronic properties of the group VIII NPs leading to modified catalytic properties. For example, Matsubu et al. found that the formation of a permeable HCO_x overlayer resulted in catalysts with higher CO selectivity for CO_2 reduction. [101] Worz et al. showed that partially reduced SMSI TiO_2 on Au NPs increases the activity for CO oxidation. [106] It was proposed that Au binds to oxygen vacancy sites in the SMSI support leading to an electron transfer from the support to Au. Kang et al. found that Pd NPs supported on TiO_2 were electron rich, compared to non-SMSI Pd, leading to weaker adsorption of acetylene, resulting in higher selectivity for the selective hydrogenation to ethylene. [78] Liu et al. showed that Pt/FeO_x exhibited higher catalytic activity for low temperature CO oxidation due to dual reaction sites, i.e., Pt sites for CO and FeO_x sites for O_2. [74]

CeO_2 is also known to exhibit SMSI, however, generally under more extreme temperatures than, for example, TiO_2. [73,107] In this study, we prepared Pt/CeO_2 catalysts, which have previously been shown to disperse as single atoms on the surface of the CeO_2 at oxidation temperatures higher than about 800 °C. [43,108] This catalyst was reduced at 550 °C and 975 °C and showed SMSI characteristics after reduction at about 975 °C. Structural characterization by extended X-ray absorption fine structure (EXAFS) and scanning transmission electron microscopy (STEM) confirm the formation of monometallic Pt NPs at both reduction temperatures. X-ray absorption near edge structure (XANES) also showed there are no changes in the electronic properties of metallic Pt NPs. After reduction at 550 °C, the TOR for ethylene hydrogenation and propane dehydrogenation was similar to that of Pt/SiO_2, a non-SMSI support. After reduction at 975 °C, however, the rate per gram for ethylene hydrogenation is strongly decreased, and STEM shows CeO_x surface coverage of these Pt NPs, i.e., an SMSI state. After reduction at 975 °C, however, Pt/CeO_2 showed much higher olefin selectivity for propane dehydrogenation. The higher olefin selectivity is suggested to

result from a decrease in the number of ensemble sites responsible for hydrogenolysis, from the partially covered SMSI Pt/CeO_2.

4.3 Materials and methods

4.3.1 Catalyst preparation

1 wt% Pt on CeO_2 was prepared by incipient wetness impregnation of a tetraammineplatinum (II) platinum nitrate (Sigma-Aldrich, 99.995%) solution onto a commercial ceria support (Solvay, HS5). The solution was impregnated 6 times with 3 hours of drying at 110 °C between each impregnation. The catalyst was then calcined in flowing air at 800 °C for 10 hours.

The monometallic Pt catalyst with 2 wt% Pt loading was prepared by a pH adjusted incipient wetness impregnation method (IWI) on SiO_2. $Pt(NH_3)_4(NO_3)_2$ was dissolved in 2 mL deionized water and ammonium hydroxide solution was added to adjust the pH to 11. The solution was added dropwise to Davisil Grade 636 silica (pore size = 60 Å, surface area = 480 m^2/g). This catalyst was then dried overnight at 125 °C and calcined at 225 °C for 3 h. Finally, the catalyst was reduced in 5% H_2/N_2 (100 mL/min) at 200 °C for 30 min and for 30 min at defined temperatures.

4.3.2 *In situ* X-Ray Absorption Spectroscopy (XAS)

In situ XAS experiments were completed at the Advanced Photon Source (APS), Argonne National Laboratory at the 10-ID beamline. Experiments were performed in florescence mode at the Pt L_3 (11.564 keV) edge. To perform experiments, the catalysts were crushed into a powder and pressed into a stainless-steel sample holder with the catalyst wafer oriented 45 degrees relative to the x-ray beam. The cell used for fluorescence measurement consists of a water-cooled stage fitted with kapton windows for fluorescence measurement. For treatments, the cell is equipped with water cooling and ceramic heaters for temperature control and valves for gas flow.

3.5% H_2/He (Airgas) was used to treat the sample cell at 550 °C for 30 minutes. He (Airgas) was flowed between each temperature exposure to cool the cell to room temperature. The cell was then sealed and moved to the beamline to perform the in situ XAS experiment. To reduce potential O_2 exposure, a He tank was connected to the gas purifier.

4.3.3 Propane dehydrogenation catalytic performance tests

Catalytic performance was tested in a fixed bed reactor with a quartz reactor tube of 3/8-inch OD. The temperature of the reactor was controlled by a furnace connected to a controller. To measure catalyst temperature, a K-type thermocouple (O.D. = 3.2 mm) was positioned in the middle of the catalyst bed. 10 mg to 200 mg of catalyst was diluted with enough silica to total 1.0 g and loaded into the reactor. The catalyst was reduced at 550°C or 975 °C with 100 ccm 5% H_2/N_2 for 30 minutes. Propane dehydrogenation was performed with 2.5% C_3H_8 and 2.5% H_2, balanced with N_2 at 550 °C. A Hewlett Packard 6890 Series gas chromatograph using a flame ionization detector (FID) with a Restek Rt-Alumina Bond/Na_2SO_4 GC column (30 m in length, 0.32 mm ID, and 0.5 μm film thickness was used to analyze the products.

4.3.4 Ethylene hydrogenation catalytic performance tests

Ethylene hydrogenation experiments were carried out in a U-tube quartz reactor (3/8 inch OD). The reactor was loaded with quartz wool before adding the catalyst, amount based on space velocity. The space velocity was adjusted to ensure conversions ¡ 5%. The thermocouple well inside the reactor was used to monitor the temperature of the catalyst bed. In a typical experiment, 3 torr ethylene (1% C_2H_4 in 5% Argon, balance Helium, Matheson Gas Company), 15 torr hydrogen (5% H_2, balance N_2, Indiana Oxygen Company) and balance UHP (ultra high purity) nitrogen (Indiana Oxygen Company). The effluent stream was analysed with a Gas Chromatography

unit equipped with a Flame Ionization Detector using a GS-Alumina (Agilent JW) capillary column.

4.3.5 Scanning Transmission Electron Microscopy (STEM)

Catalyst was mounted on holey carbon grids for imaging with an FEI Titan transmission electron microscope operated at 300 kV with image aberration correction for TEM images, or a JEOL NEOARM microscope operated at 300 kV with probe aberration correction for STEM images. Samples were mounted on the grids by a dry loading technique in order to eliminate the possibility of carbon contamination to ensure a fair comparison between as prepared, reduced and spent catalyst.

4.4 Results

4.4.1 STEM/TEM

Figure 1 shows a high magnification image of a 1wt.% Pt-CeO_2 sample that has been calcined at 800 °C, and reduced at 975 °C and a separate batch of the calcined sample was also reduced at 550 °C in H_2, Figures 1A, 1B and 1C, respectively. Similar to previous reports [43, 44, 108, 109] calcination of Pt on CeO_2 at temperatures above 800 °C leads to isolated Pt atoms, which are shown as bright spots and marked by the arrows. After reduction at 975 °C, the Pt NPs sinter to form particles. These also show a thin coating of CeO_x on the NP surface, i.e., the faint region highlighted by the white arrow in 1B. This thin film is present across the entire surface of the ceria and is visible as a disruption to the ceria lattice planes at the edges of ceria particles. Because this sample is freshly reduced using H_2, it has not been exposed to carbon. Thus the coating is not coke, but rather evidence of SMSI. Previously, HR-TEM has shown that after high temperature reduction Pt_3Ce [110] and $CePt_5$ [111] intermetallic alloys are formed. In the catalyst reduction at 975 °C, however, all the

particles index to metallic Pt, see the Fourier Transform the Pt NP (inset in Figure 1B).

4.4.2 *In situ* X-Ray Absorption Spectroscopy (XAS)

The Pt L_3 edge X-ray Absorption near edge structure (XANES) and extended X-ray absorption fine structure (EXAFS) spectra for the single atom $1Pt/CeO_2$ oxidized at 800 °C has previously been reported [44, 109]. Similar results have been found in our study shown in Figure 2 and Table 4.1. These have a XANES energy typical of Pt^{2+} ions with a first shell Pt-O coordination of 5 at 2.05 Å, with a small second shell scattering peak characteristic of isolated atoms. The Pt L_3 XANES for Pt/CeO_2 reduced at 550 °C and 975 °C are shown in Figure 4.2 (B). After 550C and 975°C reduction, $1Pt/CeO_2$ had an edge energy of 11564.0 eV, which is the same as Pt foil and consistent with monometallic Pt nanoparticles.

For $1Pt/CeO_2$ reduced at 550 °C and 975 °C, the Pt L_3 EXAFS shows three main peaks between 2-3 Å in the k2-weighted magnitude of the Fourier transform of $2Pt/SiO_2$ (Figure 4.2(C)), which is typical of the Pt-Pt scattering in metallic Pt NPs. The magnitude of the peaks was smaller when $1Pt/CeO_2$ was reduced at 550 °C indicating a smaller particle size. When reduced at 975 °C, Pt-Pt had a coordination of 10.8 (Table 4.1), which is consistent with the TEM particle size (¿10 nm). When reduced at 550 °C, the coordination number was 8.5, consistent with about 4 nm nanoparticles.

Table 4.1.
Ethylene hydrogenation tests on 1% Pt/CeO_2 using different pre-treatments

Catalyst pretreatment (°C)	XANES edge energy (eV)	Scattering Pair	Coordination Number	Bond distance (Å)	^{2} (Å^2)
800 °C/Air	11565.6	Pt-O	5.2±0.5	1.98±0.03	0.002
550 °C/H_2	11564.0	Pt-Pt	8.5±0.4	2.74±0.01	0.007
975 °C/H_2	11564.0	Pt-Pt	10.8±0.3	2.76±0.02	0.006
Pt foil	11564.0	Pt-Pt	12.0±0.4	2.76±0.01	0.003

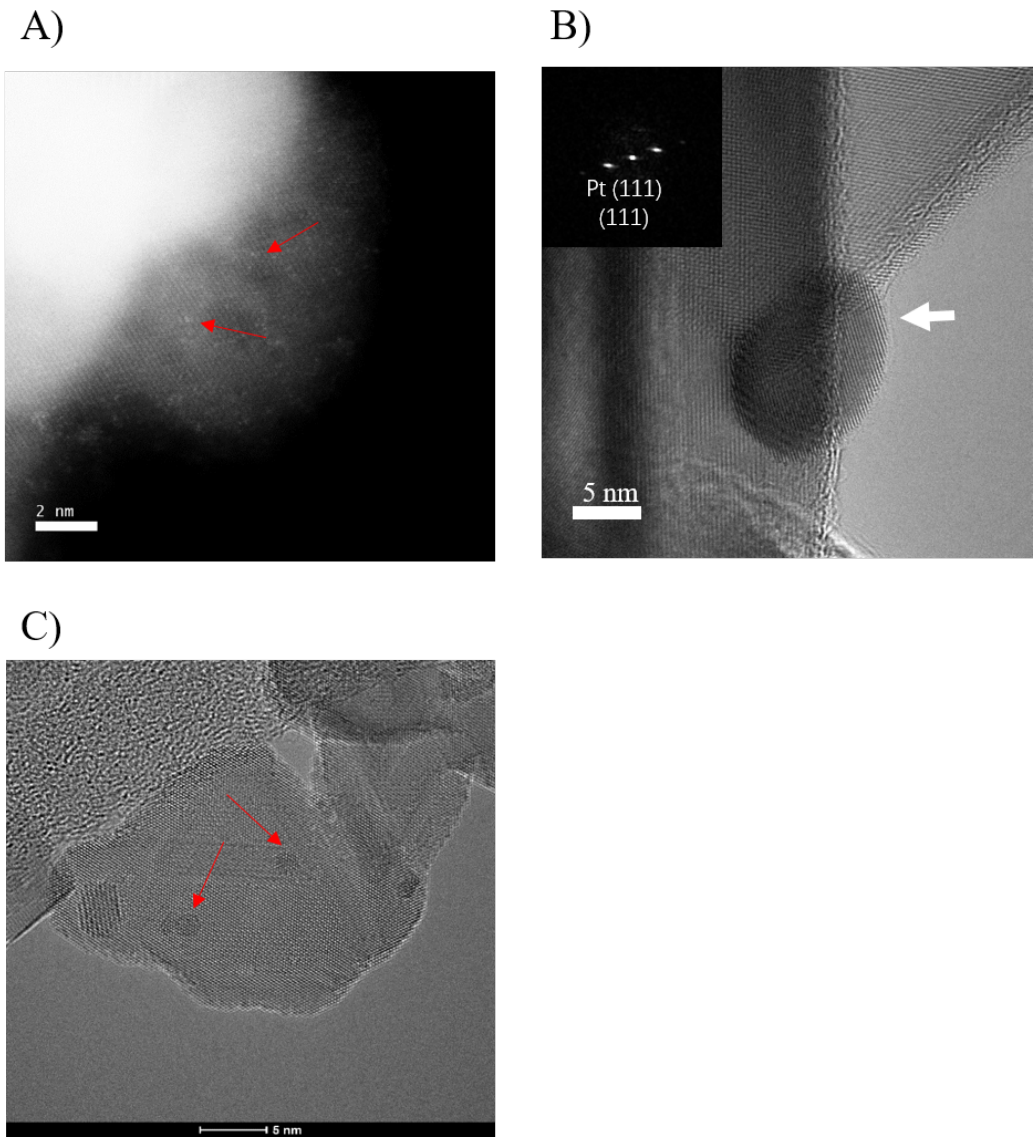

Fig. 4.1. 1wt% Pt on ceria, A. Calcined at 800 °C showing single Pt atoms on the CeO_2 support, B. reduced at 975 °C, with faint over layer of CeO_x covering the surface of the NP (white arrow), and C. reduced Pt NP's at 500 °C without a CeO_x overlayer.

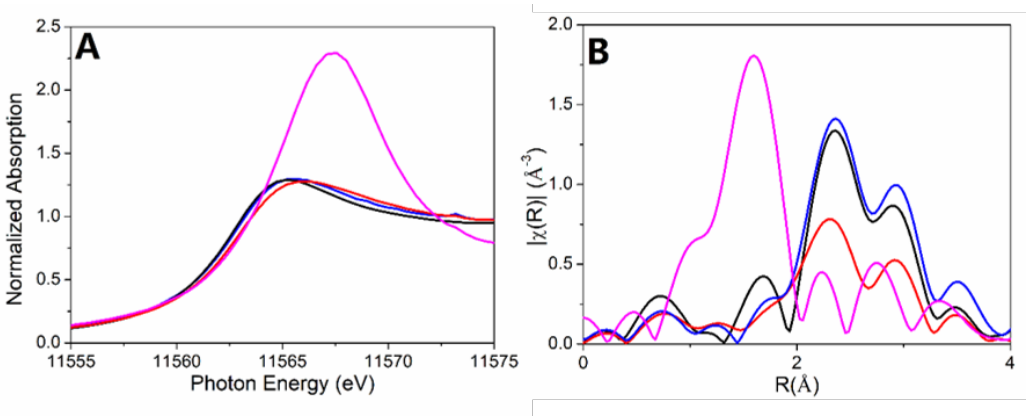

Fig. 4.2. (A) Pt L_3 edge XANES spectra of Pt foil (blue), 1Pt/CeO_2 calcined at 800 °C (magenta), 1Pt/CeO_2 reduced at 975 °C (black) and 1Pt/CeO_2 reduced at 550 °C (red). (B) Pt L_3 edge EXAFS spectra of Pt foil (blue), 1Pt/CeO_2 reduced at 975 °C (black), 1Pt/CeO_2 calcined at 800 °C (magenta) and 1Pt/CeO_2 reduced at 550 °C (red).

4.4.3 Ethylene hydrogenation

Hydrogenation of ethylene has been considered as a classical kinetic probe to understand the surface coverage of Pt [89, 112, 113]. In this work, this reaction will be used to understand the effect of varying temperature treatments on the state of the catalyst (air at 800 °C, and 550, 900 or 975 °C reduction with H^2).

As shown in Table 4.1, the fresh (air at 800 °C) Pt/CeO_2 catalysts shows low activity towards ethylene hydrogenation. Since the STEM shows that these are atomically dispersed, the turnover rate (TOR) was determined assuming each Pt is active. The TOR of 7 x 10^{-4} s^{-1} is much smaller than that reported for metallic Pt [89–91].

On H_2 reduction at 550 °C, the observed rates for ethylene hydrogenation increase to 4.3 x 10^{-1} s^{-1}, almost 3 orders of magnitude higher than atomically dispersed Pt. This is due to the formation of 4-5 nm Pt nanoparticles, which highly active for this reaction [89–91, 112]. 2%Pt/SiO2 catalyst was also tested for ethylene dehydrogenation after 550 °C and the TOR was 1.4 s^{-1} after normalization with CO chemisorption dispersion (44%). Therefore, we can estimate the Pt/CeO_2 dispersion to be 30%, which is consistent with 4 nm nanoparticles.

At higher reduction temperatures (900 °C and 975 °C), the ethylene hydrogenation rate falls significantly. Part of the loss in rate is due to sintering of the Pt NP's. The TORs based on the STEM particle sizes are 40-50 times lower than for the catalyst reduced at 550 °C, which far exceeds that from sintering alone. The strong decrease in rate is likely due to the blockage of surface Pt sites by the CeO_x over layers as evidenced in Figure 1B. Previously, CeO_2 has shown to exhibit the SMSI effect at relatively moderate temperatures (¿300 °C) and inhibit the activity of noble metal catalysts [114–116]. Cunningham *et al.* studied the effect of H_2 pretreatment on Rh/CeO_2 catalyst at temperatures up to 653 K and found a complete loss in their activity for acetone hydrogenation under reduced conditions [117]. Liotta *et al.* observed similar results with reduced activity in NO reduction by C_3H_6 for Pt/ceria-zirconia catalysts reduced in H_2 at elevated temperature. They used small angle X-ray scattering (SAXS) and XPS to detect the SMSI effect on their catalyst [118]. On the contrary, Abid et al. found that a reductive treatment at 973 K yielded a Pt/CeO_2 catalyst that was highly selectivity for crotonaldehyde hydrogenation. The improved performance was due to preferential hydrogenation of the carbonyl group in case of the metal atom existing in an SMSI state [24]. In our samples, we see little effect of SMSI at 550 °C (823 K), but do see nearly complete coverage of the Pt NP surface above 900 °C (1173 K), much higher than previously reported.

4.4.4 Propane dehydrogenation

These Pt/CeO_2 catalysts, and for comparison Pt/SiO_2, were also evaluated for propane dehydrogenation. Hydrogen was co-fed in order to increase the hydrogenolysis selectivity forming methane, ethane and ethylene, which is a more severe evaluation of the catalyst's performance. As shown in Figure 3 (pink), the propylene selectivity of $2Pt/SiO_2$ was 75% at 15% conversion, and the selectivity decreases as the conversion increases, for example about 60% at 30% conversion. The TOR was 0.17 s_{-1} (Table 3), which is consistent with previous literature [62]. For $1Pt/CeO_2$

Table 4.2.
Ethylene hydrogenation tests on 1% Pt/CeO_2 using different pre-treatments

Catalyst Pretreatment	Rate[a] (μmol/g/s)	TOR[b] (10^{-1} s^{-1})
Air/800 °C	0.04	0.0007
*H_2/550 °C	22.0	4.3
H_2/900 °C	0.5	0.01
H_2/975 °C	0.4	0.007

Reduction with 5% H_2 for 30 minutes at the defined temperatures.
Reaction conditions: P (C_2H_4) = 3 torr, P(H_2) = 15 torr, T=300 °C. Catalyst diluted to a ratio of 1:16 using Davisil grade SiO_2. Space velocity = 20 L hr^{-1} $gcat^{-1}$. Conversions for all the experiments ¡ 5%
*Space velocity = 100 L hr^{-1} $gcat^{-1}$, Dilution ratio 1:100 (to maintain ¡ 5% conversion)
[a]Initial ethane formation rate
[b]Initial TOF calculated based on total Pt loaded

reduced at 550 °C (Figure 3 (black)) the selectivity was slightly higher but similar to $2Pt/SiO_2$. The rate and change in selectivity with conversion of the former was also similar to that of the latter. Thus, the catalytic performance of 1Pt/CeO°C reduced at 550 °C is very similar to $2Pt/SiO_2$. For 1Pt/CeO°C reduced at 975 °C (Figure 3 (blue)), however, the propylene selectivity was much higher, about 94%, than for reduction at lower temperature. In addition, the change in selectivity remained high with increasing conversion. The catalyst activity was 2 magnitudes lower (Table 3), which is similar to ethylene hydrogenation.

Table 4.3.
Summary of catalytic results for propane dehydrogenation

Sample Name	Rate (mol/(s*mol catalyst))	Initial Turnover Rate (s^{-1})
Pt/SiO_2	0.077	0.17
$Pt/CeO_{2r}ed550$°C	0.065	-
$Pt/CeO_{2r}ed975$°C	0.00085	-

Reaction conditions: 550 °C, 2.5 % C_3H_8 + 2.5 % H_2 balanced with N_2; selectivity and TOR calculated at 10% C_33H_8 conversion; TOR calculated based on C_33H_8 conversion rate

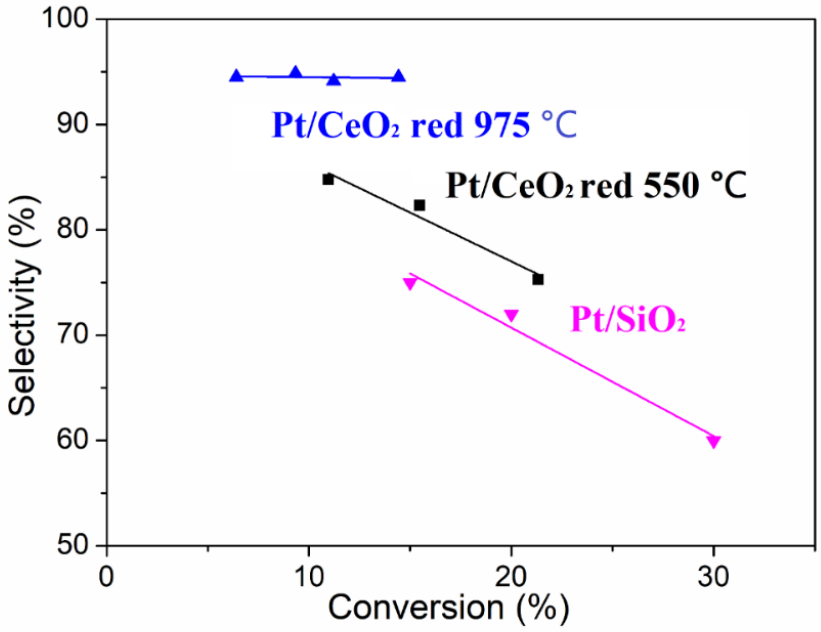

Fig. 4.3. Propylene selectivity at different conversions of 1Pt/CeO_2 reduced at 975 °C (blue, upwards triangle), 1Pt/CeO_2 reduced at 500 °C (black square), and 2Pt/SiO_2 (pink inverted triangle). Reaction conditions: 550 °C, 2.5 % C_3H_8 + 2.5 % H_2 balanced with N2.

4.5 Discussion

4.5.1 Structure of Pt/CeO_2 catalysts

Similar to previous studies, Pt single atoms are dispersed on the CeO_2 lattice after 800 °C calcination [43, 44, 108, 109]. These, however, have low catalytic activity compared to Pt NPs and are readily reduced to Pt NP's at temperatures above about 300 °C. The in situ XAS and STEM structure determination of Pt/CeO_2, reduced at 975 °C, indicates that monometallic Pt NPs are present with no evidence for formation of any intermetallic alloy, as previously reported [35, 38, 42, 62, 69, 99]. At 550 °C, the Pt NPs are 4-5 nm, with no evidence of a CeOx SMSI oxide layer. The catalytic TOR of ethylene hydrogenation is similar to Pt/SiO_2 and the propane

dehydrogenation selectivity is also similar consistent with no change in the catalytic properties due to a support interaction. Reduction after 975 °C, however, lead to the formation of an amorphous over layer observed by STEM, Figure 1B, and a significant loss in the TOR for ethylene hydrogenation consistent with CeO_x SMSI. The formation of the SMSI oxide, however, occurred at much higher temperature than reported for Pt/TiO_2, for example, which occurs at about 500 °C [75,105]. This is consistent with previous studies by Deleitenburg et al. showing that CeO2 only exhibits SMSI behavior under extremely harsh conditions while SMSI for TiO_2 and Nb_2O_5 supports occur at much lower temperature [107]. At these high temperatures required for CeO_x SMSI, the Pt NPs also sinter (ca. 15 nm) compared to the particles at lower temperature (4-5 nm).

SMSI oxides are often suggested to increase number of electrons on the metal NPs by transfer of electron density from the partially reduced support. For example, it has been shown by XPS that the $4f_{7/2}$ peak is shifted from 71.0 eV (Pt) to 70.2 eV (Pt/TiO_2) suggesting that TiO_2 provided electrons to the Pt nanoparticles [92,93]. In this study, the XANES edge energy of Pt/CeO_2 after reduced at 550 and 975 °C are very similar suggesting little change in the energy of the Pt valence orbitals.

4.5.2 The effect of SMSI on catalyst performance

The TOR of Pt NPs is independent of particle size and support for ethylene hydrogenation; thus one can estimate the SMSI coverage of the Pt NPs from the apparent TOR for the Pt/CeO_2 reduced at 975 °C. From the STEM images, the particle size of the latter is about 15 nm, which corresponds to 6% of dispersion [119]. However, the apparent TOR is much lower. Assuming that the loss in rate is due to surface coverage by SMSI CeO_2, approximately 88% of the catalytic sites are inaccessible for catalysis. Of the few remaining exposed sites, these are structurally or electronically unchanged by the interaction with the CeO_x over layers. Nevertheless, there is a significant increase in the olefin selectivity for propane dehydrogenation.

Alkane dehydrogenation, which is the reverse reaction of olefin hydrogenation is a structure insensitive reaction, thus, only requires individual atoms for catalytic activity. Hydrogenolysis, a structure sensitive reaction, requires several atom ensemble active sites [98]. Intermetallic alloys such as Pt_3Mn, [63] Pt_3Co [38], Pt_1Bi_1 [99], Pt_3Cr [35], Pt_3V [88]and Pt_1Zn_1 [42] have been identified to have isolated or three atom ensemble Pt sites and are highly olefin selective for alkane dehydrogenation. While in situ EXAFS and STEM suggested that Pt/CeO_2 did not form an alloy even after 975 °C reduction, the high propylene selectivity suggests that the ensemble size of the catalyst was likely reduced. Previous studies have shown that catalysts in the SMSI state inhibit hydrogenolysis. Previous studies have shown that SMSI catalysts inhibits hydrogenolysis. Ethane hydrogenolysis has been suppressed on Pd/TiO_2 in a study by Bracery *et al.*; while HDO of m-Cresol on $NiMo/SiO_2$ catalyst also showed hydrogenolysis suppression [100, 120]. Therefore, the higher propylene selectivity is likely that due to the high surface coverage of these large Pt NPs by CeO_x resulting in few ensemble sites capable of hydrogenolysis.

4.6 Conclusion

In summary, single atom Pt sites on CeO_2 have low catalytic rates for hydrogenation and are readily reduced to Pt NPs at temperatures above about 300 °C. Small to moderate sized NPs formed at temperatures below about 550 °C, display normal Pt catalytic properties for ethylene hydrogenation and propane dehydrogenation with no evidence of an SMSI CeO_x by catalysis or STEM. Reduction at 975 °C leads to sintering of the Pt NPs to about 15 nm and coverage of greater than about 95% of these larger particles by an SMSI CeO_x. Both sintering and SMSI lead to a large loss in catalytic rate. The small number of exposed Pt sites on SMSI Pt/CeO_2, however, lead to highly selective propane dehydrogenation catalysts compared to Pt/SiO_2, for example. The high olefin selectivity is likely due to smaller Pt ensembles, which

suppress hydrogenolysis reactions, while these exposed sites remain active for dehydrogenation.

4.7 Acknowledgement

This work was supported by the National Science Foundation under Cooperative Agreement No. EEC-1647722. Use of the Advanced Photon Source was supported by the U.S. Department of Energy Office of Basic Energy Sciences under contract no. DE-AC02-06CH11357. MRCAT operations, beamline 10-ID, are supported by the Department of Energy and the MRCAT member institutions. This work was performed, in part, at the Center for Integrated Nanotechnologies, an Office of Science User Facility operated for the U.S. Department of Energy (DOE) Office of Science by Los Alamos National Laboratory (Contract 89233218CNA000001) and Sandia National Laboratories (Contract DE-NA-0003525). Authors also want to thank JEOL for the use of STEM.

5. TUNING GEOMETRIC AND ELECTRONIC STRUCTURE OF PLATINUM CATALYSTS FOR PROPANE DEHYDROGENATION BY PHOSPHOROUS PROMOTION

This chapter is reproduced from Kou, Jiajing, et al."Tuning geometric and electronic structure of platinum catalysts for propane dehydrogenation by phosphorous promotion." submitted to ACS Catalysis.

5.1 Abstract

Metal phosphides are promising catalytic materials for alkane dehydrogenation and potentially other reactions. This work demonstrates the effect of phosphorus on the geometric and electronic environments of Pt in Pt-P catalysts. Two types of catalysts, PtP_2-rich surface on Pt core and full PtP_2 ordered structure, were characterized by scanning transmission electron microscopy (STEM), *in situ* X-ray absorption spectroscopy (XAS), and in situ synchrotron X-ray diffraction (XRD). In PtP_2 structure, Pt isolated by P atoms shows olefin high selectivity in propane dehydrogenation (PDH). X-ray photoelectron spectroscopy (XPS), X-ray absorption near edge structure (XANES) and *in situ* resonant inelastic X-ray scattering (RIXS) show P significantly modifies the energy of Pt 5d valence electrons and empty orbitals in PtP_2, which directly relates to catalysis. There is a large energy difference between unfilled Pt 5d states and filled Pt 5d states, which is suggested to decrease the Pt-adsorbate and reaction intermediate bond energies and improved catalytic performance.

5.2 Introduction

Catalytic dehydrogenation processes are of great significance due to increasing light alkanes supply from shale gas and the growing demand for olefins. [5, 89] For

propane dehydrogenation (PDH), the challenge is to cleave C-H bonds, but not C-C bonds. Additionally it is desirable to inhibit coke formation, which rapidly deactivates active sites. [31] Pt catalysts are well known to have high activity for alkane dehydrogenation; however, monometallic Pt has low olefin selectivity and deactivates rapidly. [31, 121] To improve these catalysts, a second metal (including Cr [35], Sn [89, 122], Zn [42], Co [38], Bi [99], Sb [64] and In [69]) has been investigated as a promoter by forming bimetallic Pt catalysts which show higher olefin selectivity. The increase in selectivity is attributed to the inhibition of hydrogenolysis by decreasing surface Pt ensembles as well as leading to a change of energy of the Pt valence orbitals. For example, Zhu *et al.* [122] observed an extremely high selectivity in PDH at 580 °C which is associated with isolated active Pt atoms by Sn. Cybulskis *et al.* [42] showed that Zn addition to Pt catalysts can not only form Pt_1Zn_1 alloys with isolated Pt sites, but also lowers the energy of the filled Pt 5d orbitals, significantly increasing the selectivity for ethane dehydrogenation.

Metals phosphides are an interesting class of materials and worth investigating due to their unique physicochemical properties and potential for large-scale applications. They are a potential alternative to bimetallic Pt catalysts for alkane dehydrogenation. Nickel, cobalt, iron and molybdenum phosphides have been studied for hydrogenation reactions, including hydrodesulfurization (HDS), hydrodenitrogenation (HDN) and hydrodeoxygenation (HDO). [123–125] However, the potential of metal phosphides for alkane dehydrogenation reaction remains underexplored. One example for PDH reported that Fe modified by phosphorus improved the propylene selectivity by suppressing cracking reactions. [126]

While earth abundant transition metal phosphides have received considerable attention for hydrogenation, noble metal phosphides have been less well studied, especially for alkane dehydrogenation. Noble metal phosphides share numerous properties with other metal phosphides, including forming well-defined structures with metallic catalytic properties. While the syntheses and investigation of RuP, Ru_2P, Pd_5P_2, RhP and PtP_2 were previously described, the application of these materials was lim-

ited to HDS and HDN reactions. [124, 127–130] Kanda et al. [127] observed these silica-supported noble phosphides show higher activities for HDS compared with the reduced noble metals on silica except in the case of Pt. The synthesis and study of PtP materials have attracted much attention recently in the field of electro-chemistry since many high-performance metal phosphide alloys have been widely reported in oxygen reduction (ORR) and oxygen evolution reaction (OER). [37, 131–134] PtP NPs were successfully synthesized by Ji et al. [135] and performed in methanol oxidation reaction, where they progressively changed from amorphous to crystalline with the temperature increasing to 400 °C. Although some encouraging progress have been made, noble metal phosphide catalysts have not been evaluated for alkane dehydrogenation.

In this work, we synthesize silica supported, 2-3 nm sized PtP_2 catalysts by two different methods and investigate their nanoparticle (NP) and surface structures. Two types of Pt-P catalysts, core-shell NPs (PtP_2-rich shell on Pt core) and full-body PtP_2 NPs are synthesized by sequential incipient wetness impregnation (IWI). The structures of the catalysts were determined by in situ X-ray absorption spectroscopy (XAS), *in situ* X-ray diffraction (XRD), and scanning transmission electron microscopy (STEM). In addition, the CO absorption was also investigated by *in situ* diffuse reflectance infrared Fourier transform (DRIFT) and CO chemisorption. To explore the electronic effects by the addition of P, X-ray photoelectron spectroscopy (XPS) and *in situ* resonant inelastic X-ray scattering (RIXS) were performed on the full PtP_2 ordered structure. The effect of change in energy of the Pt 5d orbitals as well as the NP and surface structures were also correlated to their catalytic performance for PDH.

5.3 Materials and methods

5.3.1 Materials

Davisil 636 silica gel (480 m^2/g, 0.75 mL/g pore volume, 99%), $Pt(NH_3)_4(NO_3)_2$ (99.995%), and H3PO4 (85% aq.) were purchased from Sigma-Aldrich and used without further purification. The gases used for the catalytic tests were purchased from Indiana Oxygen Company. The C_3H_8 is 5% balanced with N_2, and the H_2 is also 5% balanced with N_2. The gases used for XAS and XRD experiments were purchased from AirGas, Illinois.

5.3.2 Catalyst synthesis

All catalysts were synthesized by sequential incipient wetness impregnation (IWI). To prepare Pt/SiO_2 with target Pt loading of 2 wt%, 0.2 g of $Pt(NH_3)_4(NO_3)_2$ was dissolved in 2.75 mL de-ionized (DI) water, and 1.0 mL concentrated NH4OH was added to obtain a clear solution with pH around 11. This solution was added dropwise to 5.0 g Silica (Davisil 636) with continuous stirring. The obtained sample was dried at room temperature (RT) for 3 h before drying at 105 °C overnight, and then calcined at 225 °C for 3 h. The reduction step was performed under a 5% H2/N2 at 225 °C for 30 min, and then 250 °C for 30 min, followed by 550 °C for another 30 min.

To prepare P-Pt catalysts with low P loading, a certain amount of H_3PO_4 (85% aq.) was dissolved in DI water to give a total volume of 15 mL. 3.75 mL of this solution was added dropwise to 5.0 g of the reduced Pt/SiO_2. The resulting solid was dried at RT for 3 h before drying in the oven at 105 ° overnight. The obtained catalyst was denoted as Pt-P-x (x<10), where x means the molar ratio of P over Pt. Pt-P-1, Pt-P-2, Pt-P-4 were synthesized by this method, respectively.

To prepare Pt-P catalysts with high P loading, the Pt/SiO_2 was not reduced. The above diluted H_3PO_4 was dropwise added to the unreduced Pt/SiO_2. The obtained solid was dried at RT for 3 h before drying in the oven at 105 °C overnight, and then

calcined at 600 for 1 h. The obtained catalyst was denoted as Pt-P- y (y)≥10), where y also donates as the molar ratio of P over Pt. Pt-P-10, Pt-P-20 and Pt-P-50 were synthesized by this method, respectively.

5.3.3 Catalyst testing

Propane dehydrogenation was carried out in a quartz fixed-bed reactor with a quartz tube of 3/8 in. OD. To vary the initial conversion, the loaded catalysts range from 10 to 300 mg and were diluted with SiO_2 to 1 g. A thermocouple was placed at the center of the catalyst bed to measure the reaction temperature. Before each test, the catalyst was reduced for 30 min at 550 °C under 100 mL/min 5% H_2/N_2. The flow of 5% C_3H_8 and 5% H_2 were adjusted to vary the initial conversion. The gas products were analyzed with an Agilent 7890A gas chromatograph system equipped with a Flame Ionization Detector (FID).

5.3.4 Scanning transmission electron microscopy (STEM)

The atomic resolution microscopy analysis for Pt-P catalysts was performed on a JEM ARM200F thermal-field emission microscope with a probe Cs-corrector working at 200 kV which is located at electron microscopy center of Dalian Institute of Chemical Physics (DICP) Chinese Academy of Sciences. For the high angle annular dark-field (HAADF) imaging, the convergence angle of 23 mrad and collection angle range of 68-174 mrad were adapted for the incoherent atomic number imaging. The elemental composition as well as distribution iswerewas analyzed on the energy dispersive X-ray analyzer (EDS, EX-230 100 mm^2 detector) equipped on the microscope.

Additionally, the Titan Themis G3 environmental transmission electron microscope (ETEM, Thermo Scientific Company) worked at 300 kV in TEM mode was utilized as complementary to ARM200F microscopy for imaging the Pt-P-50 catalyst. For all the STEM/TEM sample preparation, catalysts were dispersed in ethanol

and dropped onto the copper grids and dried on a hot plate (150 °C). Several images were taken from randomly selected locations on the catalysts to perform the size distribution based on over 400 nanoparticles.

5.3.5 *In situ* X-ray absorption spectroscopy (XAS)

In situ XAS measurements at the Pt L_3 edge (11.564 keV) in transmission mode were performed at the 10-BM-B beamline at the Advanced Photon Source (APS), Argonne National Laboratory. Catalysts and reference compounds were ground into fine powders and pressed into a sample holder containing six wells. Then the holder was loaded into a quartz tube allowing gas flow so that samples could be treated prior to measurements. The catalysts were treated with 3.5% H_2/He at 550 °C, then cooled to RT in flowing He before moving to the beamline to acquire data. For internal energy calibration, a Pt foil scan accompanied with each measurement was simultaneously obtained. Athena software was used to calibrate energy and normalize the data, and the edge energy was determined by the first maximum peak in the first derivative of X-ray absorption near edge structure (XANES) spectra. [136] Extended X-ray absorption fine structure (EXAFS) spectra were fit using a least-squared fit in R-space of k^2-weighted Fourier transform (FT) to determine coordination number (CN) and bond distances (R) between Pt and its neighbors using the Artemis software26, and the k range for Fourier transform of Pt L3 edge was k = 3.0 12.0 Å-1.The $S0^2$ value was determined from fitting the Pt foil standard. In the fit of the difference XAS spectrum, the phase of the Pt-O scatter is radian out of phase from the normal scattering pair due to subtraction of the oxidized EXAFS from the reduced.

5.3.6 X-ray photoelectron spectroscopy (XPS)

X-ray photoelectron spectroscopy (XPS) measurement was performed over a Kratos AXIS Ultra DLD Imaging spectrometer, using monochromatic Al K radiation as an excitation source. Prior to spectra acquisition, fresh catalysts were firstly reduced in

a catalytic cell by 5% H^2 balanced with Ar at 550 °C for 1 h, and then transferred under ultra-high vacuum (UHV) into the analysis chamber without exposure to air.

The data was analyzed with CasaXPS software. For charge correction, the C 1s peak of the adventitious carbon was set to a binding energy of 284.8 eV. The background was subtracted using Shirley line shape, and curve-fitting was performed using synthetic function of Lorentzian blended with Gaussian.

5.3.7 *In situ* X-ray Diffraction (XRD)

In situ XRD measurements were performed at the 11-ID-C beamline at the APS, Argonne National Laboratory. The data were collected in transmission mode by a PerkinElmer large-area detector using X-rays of λ=0.1173 Å at 105.091 keV. Samples were pressed into thin wafers, then loaded into a Linkam Scientific TS1500 heating stage equipped with water cooling. Prior to measurements the stage was purged with He for 5 min at RT and then ramped to 550 °C in 3.5% H_2/He at 50 cc/min. Diffraction patterns were acquired after reduction at 550 °C for 20 min, and also collected at 35 °C after being cooled down in the same atmosphere. The 2-D scattering images were integrated to 1-D intensity versus 2θ plots by using Fit2D software. [137] Materials Analysis Using Diffraction (MAUD) software was used to simulate standard diffraction patterns of Pt FCC and PtP_2 phases which were used to determine the crystal structure of Pt-P catalysts in comparison with experimental diffraction patterns. [138]

5.3.8 *In situ* infrared spectroscopy (IR)

In situ diffuse reflectance infrared Fourier transform (DRIFT) spectra were collected on a Nicolet iS50 spectrometer with a mercury cadmium telluride (MCT) detector cooled by liquid nitrogen. Prior to the test, 20 mg of the sample was reduced at 550 °C under 5% H_2 for 30 min, and the background spectrum was collected after purging with N_2 at room temperature for 40 min. Then the pre-reduced samples were

exposed to 10 vol.% CO in N_2 at 25 °C for 40 min, and the sample IR spectra were collected after purging with N_2 for 40 min.

5.3.9 CO chemisorption

The CO chemisorption were measured by a Micromeritics ASAP 2020 chemisorption device. Approximately 0.1 g of catalysts whose size has been prescreened between 60 and 120 mesh, was placed in a U-shaped quartz reactor. The chemisorption tests were conducted at 35 °C with 50 cc/min of 5%CO. Before each test, the sample was first heated to 550 °C in a flow of 5% H_2 with 50 cc/min, then cooled to 35 °C.

5.4 Results

5.4.1 STEM

The particle sizes of Pt-P catalysts were determined by STEM. The uniform distribution of the bright spots suggests a narrow range of the particle sizes, which could be confirmed by the statistic size distribution, as shown in Figure 5.1 and Table 5.1. All catalysts have average particle sizes less than 3 nm. As for the Pt-P catalysts with low P loading, the average particle size of Pt-P-2 is 1.7 nm. With increasing the P loading, the particle size decreased slightly, and Pt-P-4 has smallest particle size of 1.1 nm. Whereas for the Pt-P catalysts with high P loading, the average particle size is around 2-3 nm. The average particle sizes of Pt-P-10 and Pt-P-50 are 2.6 and 2.4 nm, respectively. Pt-P-50 shows broader particle size distribution and larger standard deviation than that of Pt-P-2.

5.4.2 *In situ* X-ray Absorption Spectroscopy (XAS)

The local Pt coordination was determined by XAS at the Pt L3 edge (11.564 keV). The XANES spectra of Pt-P samples are shown in Figure 5.2. The XANES spectra of Pt nanoparticles (black line) shows a shape, white line intensity and edge

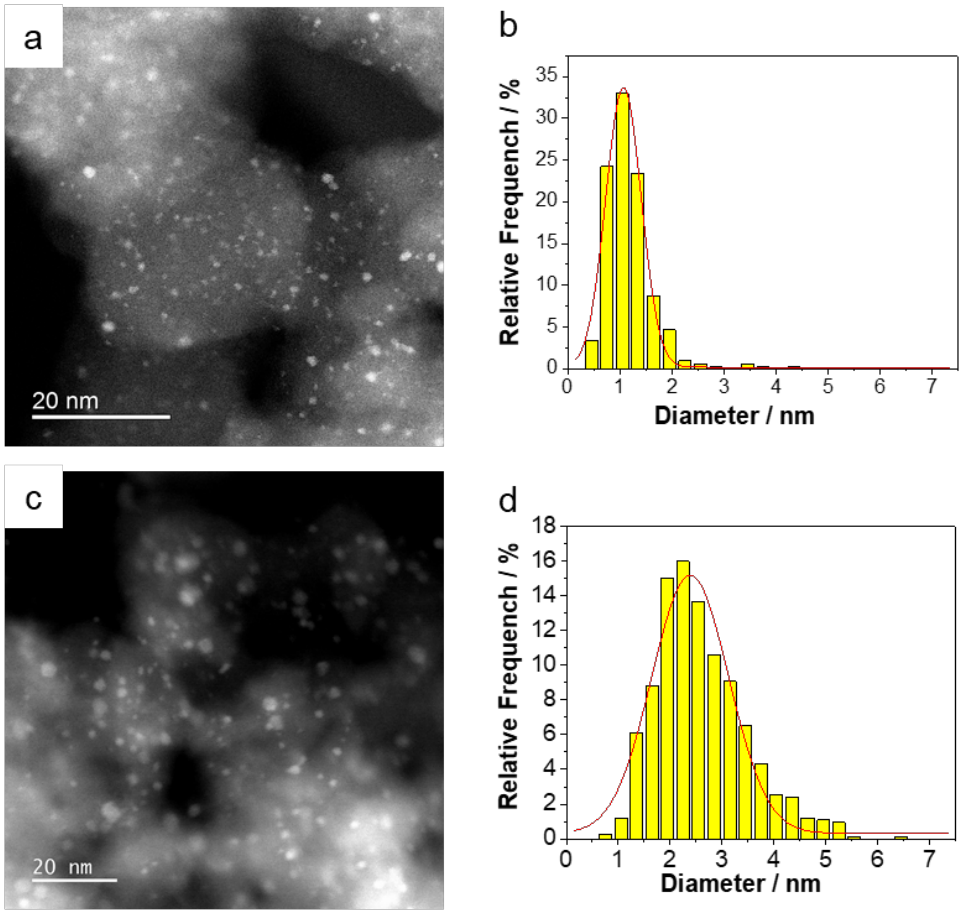

Fig. 5.1. STEM images and particle size distributions for Pt-P-4 (a, b) and Pt-P-50 (c, d).

Table 5.1.
Particle Size Distribution of the Nanoparticles

Sample Name	Pt (wt%)	Molar Ratio of P:Pt	Average Particle Size (nm)	Standard Deviation
Pt-P-2	2	2	1.7	0.5
Pt-P-4	2	4	1.1	0.3
Pt-P-20	2	10	2.6	1.0
Pt-P-50	2	50	2.4	0.7

energy, similar to those of Pt foil, consistent with fully reduced Pt. For all Pt-P catalysts, the XANES energy, which is the inflection of the leading edge, is shifted to

higher energies (Figure 5.2). In addition, there is an increase in the intensity of the white line, i.e. the first peak beyond the edge. As the amount of P in the catalysts increased, both the edge energy and white line intensity increased (Table 5.2). The maximum XANES edge energy shift of 1.5 eV was observed in Pt-P-20 and Pt-P-50 catalysts.

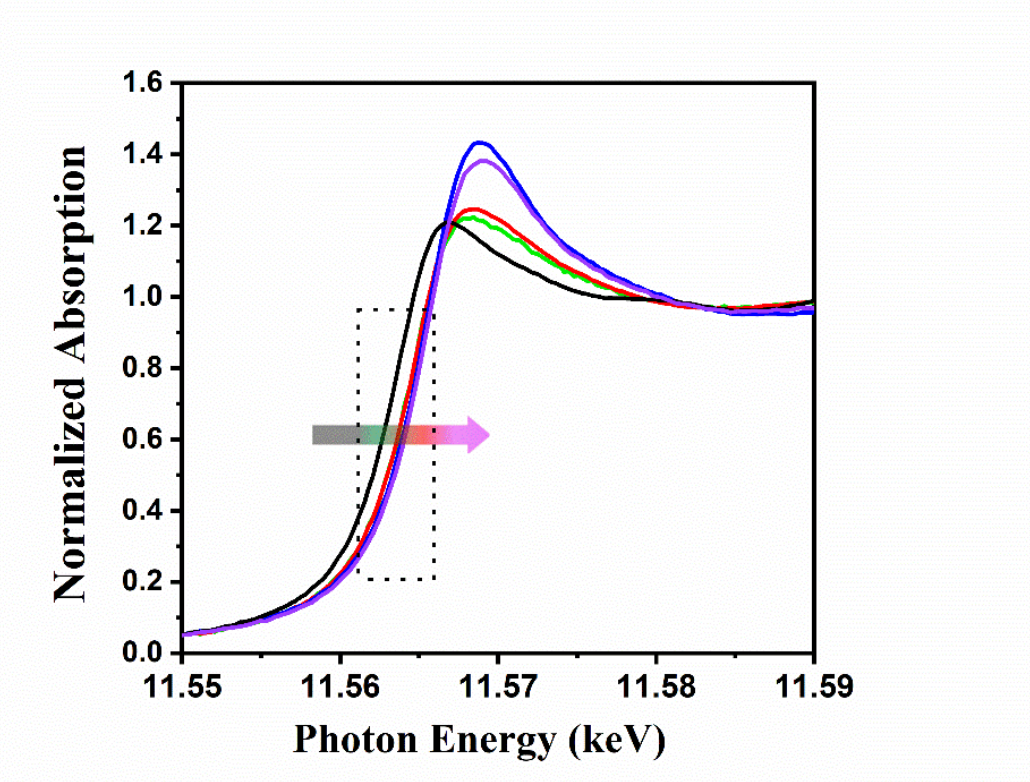

Fig. 5.2. Normalized XANES spectra at the Pt L_3 edge of Pt/SiO_2 (black line), Pt-P-1(green line), Pt-P-4 (red line), Pt-P-20 (purple line) and Pt-P-50(blue line).

The k^2-weighted magnitudes of the FT of EXAFS spectra of Pt and Pt-P NPs are shown in Figure 3. The magnitude and imaginary parts (not shown) of the FT of the EXAFS at Pt L3 edge of all catalysts were fit to determine the coordination number (CN) and bond distances (R), Table 5.2. The spectrum of Pt/SiO_2 shows the same shape and peak position as a Pt foil, where there are three main peaks between about 2 Å and 3 Å (phase uncorrected distance).8 The Pt-Pt coordination number

(CN_{Pt-P}) of Pt/SiO_2 was 8.1 at 2.74 Å, and the lower CN_{Pt-P} and shorter bonding distance compared with those of the Pt foil are typical of nanoparticles. [87]

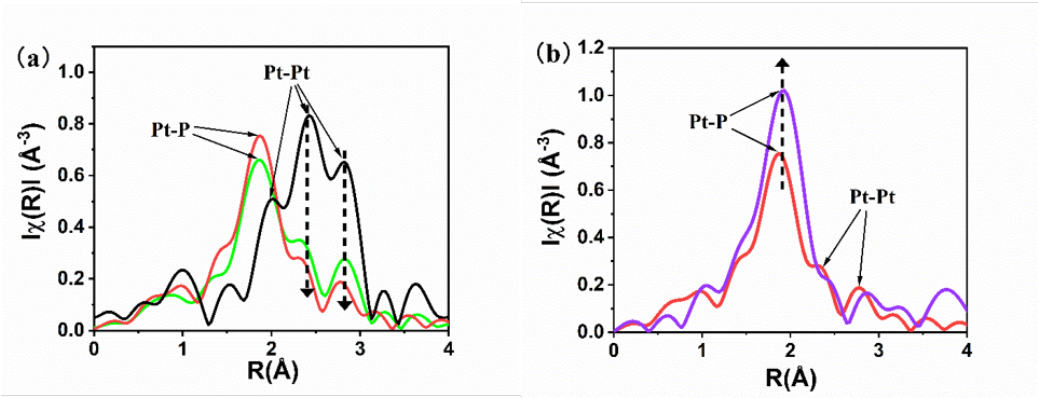

Fig. 5.3. Pt L_3 edge EXAFS of Pt/SiO_2 (black line), Pt-P-1 (green line), Pt-P-4 (red line) and Pt-P-20 (purple line).

The Pt-P-20 catalyst has a very different spectrum from Pt NPs (Figure 3b). A large peak located around 2 Å, likely indicating the presence of shorter bonds, but no peaks from Pt-Pt scattering. The spectrum was fit with Pt-P scattering and the Pt-P coordination number (CN_{Pt-P}) of 4.0 at 2.35 Å was obtained. A similar fit (CN_{Pt-P} of 4.1 at 2.36 Å) with one Pt-P scattering path was obtained for Pt-P-50.

Compared with Pt-P-20 and Pt NPs, the EXAFS spectrum of Pt-P-4 sample shows a large peak at about around 2 Å and much smaller second and third peaks between about 2-3 Å, likely suggesting the presence of both Pt-Pt and Pt-P bonds. Two scattering pairs of Pt-Pt and Pt-P were used to fit the EXAFS, resulting in a CN_{Pt-P} of 2.7 at 2.73 Å and CN_{Pt-P} of 2.3 at 2.31 Å.

5.4.3 *In situ* XRD

While XAS shows there are Pt-P bonds in these catalysts, it is a local scattering technique and does not provide information on the crystal phase of the NPs. *In situ* synchrotron XRD was performed to identify the phase. Due to the high X-ray energy (105.70 keV or λ=0.1173 Å), the resulting in diffraction patterns were obtained at

Table 5.2.
Particle Size Distribution of the Nanoparticles

Sample Name	Edge Energy (keV)	R(Å)	CN	
Pt/SiO_2	11.5640	Pt-Pt	2.74	8.4
Pt-P-1	11.5643	Pt-Pt	2.73	4.3
		Pt-P	2.32	2.0
Pt-P-2	11.5645	Pt-Pt	2.73	2.9
		Pt-P	2.31	2.3
Pt-P-4	11.5649	Pt-Pt	2.73	2.7
		Pt-P	2.31	2.3
Pt-P-4	11.5655	Pt-P	2.35	4.0
Pt-P-50	11.5655	Pt-P	2.36	4.1

lower 2θ angles, typically from 0 to 10° shown in Figure 5.4. The high flux of the synchrotron x-ray beam gives a better signal-to-noise ratio, while shorter wavelength enables the diffraction within a shorter range, both of which are crucial for resolving small diffraction peaks of around 2 nm NPs. In order to reduce the effects of thermal strain, the XRD patterns for all the catalysts were obtained at room temperature in H_2 atmosphere after reduction in H_2 at 550 °C. Figure 5.4a shows all the reflections of Pt-P-1 match those of simulated Pt face center cubic (FCC) structure. The broad peaks of Pt-P-1 indicated smaller particle sizes than bulk metallic Pt, and the peak position slightly shifted to higher 2θ angles due to the slightly shorter bond distance of Pt-P-1 NPs. 30 Although XAS suggested two components in Pt-P-1, the XRD patterns show only metallic Pt NPs. It is likely that scattering from the small size of Pt-P NPs could not be detected by XRD. At high P loading, e.g. Pt-P-20 catalyst, the XRD pattern matched most peaks of simulated PtP2 (ICSD 9015002) with a lattice spacing of 2.81 Å are ascribed to (020) and (200) of PtP_2. The peaks of Pt-P-20 are broader than those of bulk PtP_2, consistent with the small particle size. The unit cells of Pt and PtP_2 are shown in Figure 4b. In PtP_2 structure, Pt still adopts FCC unit cell, while two P atoms are midway between the Pt atoms, which are at a

distance of 4.02 Å, significantly longer than that in Pt NPs (2.78 Å). Therefore, Pt atoms in PtP_2 are geometric isolated by P atoms.

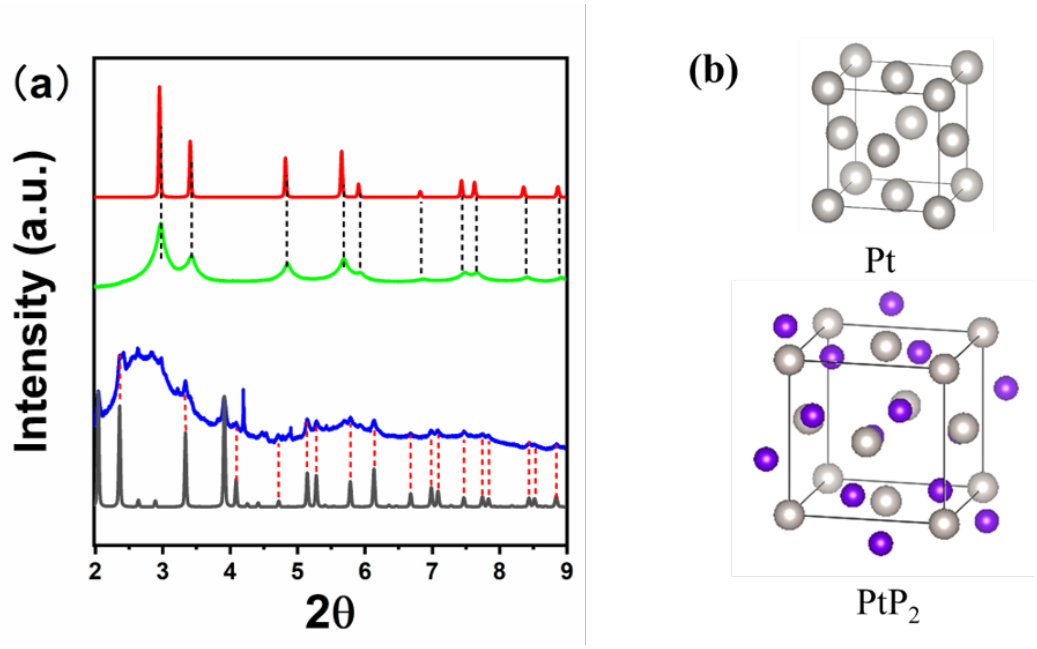

Fig. 5.4. (a) XRD patterns of Pt-P-1 (green line), Pt-P-20 (blue line), Pt simulation (red line, ICSD 9012957) and PtP_2 simulation (black line, ICSD 9015002); (b) the unit cell of Pt and PtP_2 (Pt atoms are represented in gray and P atoms in purple).

5.4.4 HRSTEM

To further confirm the structure of Pt-P catalysts, high angle annular dark field (HAADF) STEM was conducted on Pt-P-2, Pt-P-4 and Pt-P-50, and images are shown in Figure 5. Figure 5(a) presents a highly ordered NP with a zone axis ⟨001⟩ for Pt-P-50. The lattice spacing of 2.81 Å is ascribed to (020) and (200) of the PtP_2 structure. The characteristic of atomic number is correlated contrast distribution in HAADF. For Pt-P-2 catalyst (Figure 5b), the lattice spacings of 1.95 Å and 2.34 Å are pointed to the (200) and (111) of Pt FCC structure, whereas at the edge of the particle, the spacings of 2.86 Å and 3.38 Å are consistent with (200) and (111) of

PtP2 structure. The brighter core and relatively darker shell correspond to metallic Pt and PtP_2, suggesting Pt-P-2 catalyst has a core-shell structure with likely one layer of PtP_2 shell on Pt core. Similarly, for Pt-P-4 catalyst (Figure 5c), the lattice spacing of 2.34 Å is corelated to Pt (111) and the 2.82 Å is corelated to PtP2 (200), showing a core-shell structure with Pt core.

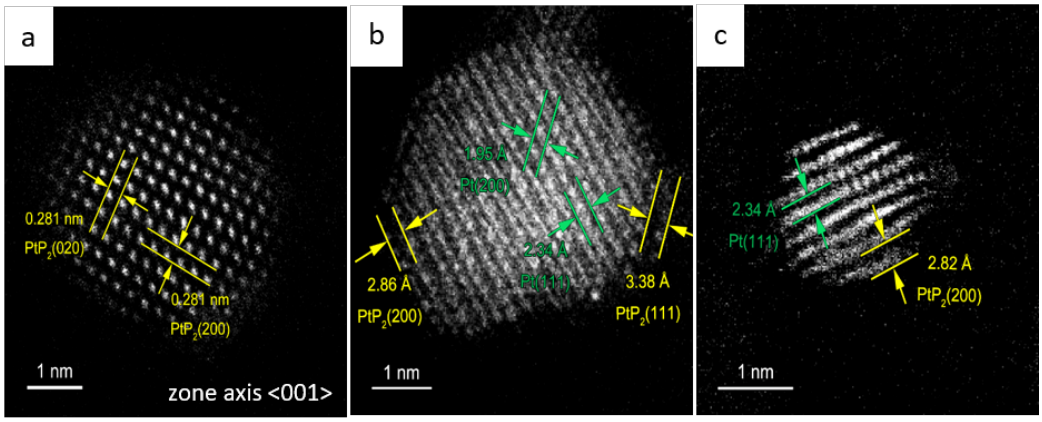

Fig. 5.5. HRSTEM images of (a) Pt-P-50, (b) Pt-P-2 and (c) Pt-P-4.

5.4.5 XPS

The catalysts were further analyzed for chemical states of Pt by XPS, as shown in Figure 5.6. Pt 4f region consists of two components which correspond to two spin-orbital splitting peaks of Pt $4f_{7/2}$ (at lower binding energy) and Pt $4f_{5/2}$ (at higher binding energy). As a reference, Pt/SiO_2 exhibits a Pt $4f_{7/2}$ peak at 71.8 eV, which is assigned to metallic Pt. This value is higher than the binding energy of Pt bulk metal at 71.0 eV, due to the deceased extra-atomic relaxation of small metal particles. [139] For Pt-P-50, the Pt $4f_{7/2}$ binding energy is at 73.0 eV, higher than that of Pt NP's. The 1.2 eV shift towards higher binding energy in comparison with Pt NPs can be attributed to the presence of Pt-P bonds in the NPs. For Pt-P-4 catalyst, the spectrum can be well fitted by two pairs of peaks, indicating that Pt was in two different chemical states. One Pt $4f_{7/2}$ peak at 72.0 eV is ascribed to Pt0

and the other at 73.1 eV is ascribed to Pt-P alloy structure. The percentages of Pt0 and Pt-P are 70% and 30%, respectively, estimated by the area of peaks. This is also consistent with Pt-Pt and Pt-P bonds observed by EXAFS and HRSTEM.

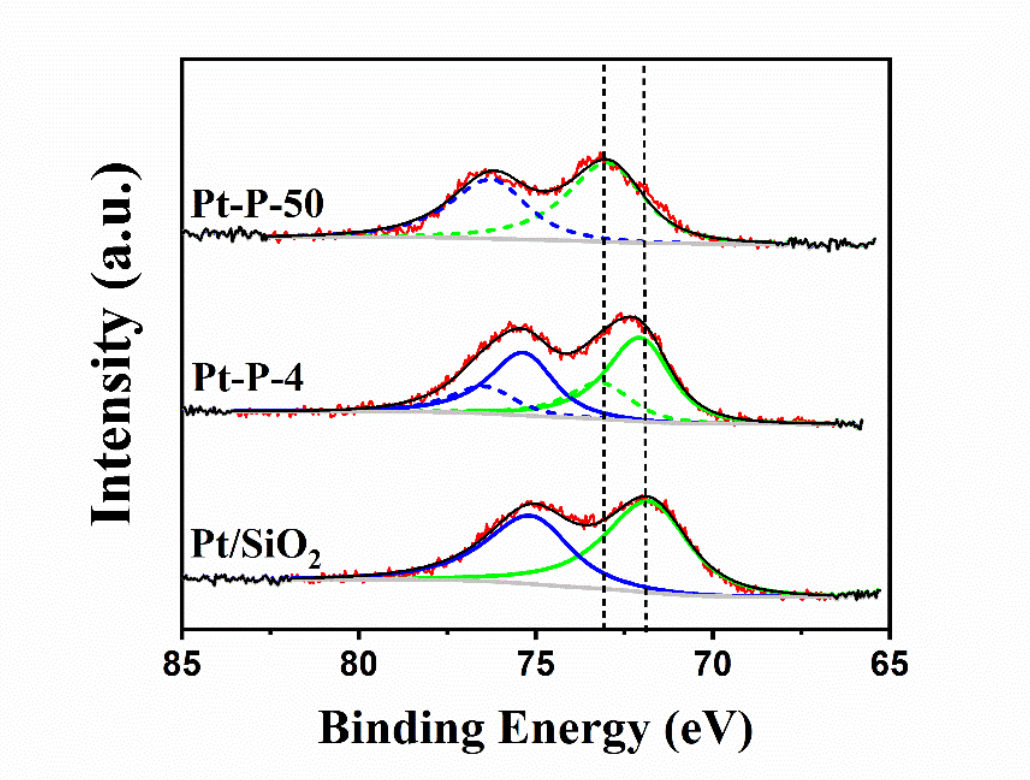

Fig. 5.6. Pt 4f XPS spectra of catalysts after reduction at 550 °C with H_2. Raw data (red solid line), fitting curve (black solid line),Pt^0 state: Pt $4f_{7/2}$ (green solid line) and Pt0 $4f_{5/2}$ (blue solid line), Pt^{2+} state: Pt $4f_{7/2}$ (green dash line), Pt $4f_{5/2}$ (blue dash line).

5.4.6 RIXS

The formation of PtP_2 alloy changes the unfilled 5d orbital energies of Pt suggested by the L_3 edge XANES and the binding energy seen in XPS. Both techniques, however, are indirect measurements of the energy of the filled 5d orbitals, which are also responsible for catalytic performance. To determine the energy of the valence states by P alloying, *in situ* RIXS measurements were conducted on Pt/SiO_2 and

PtP_2/SiO_2. The energy difference between the unfilled and filled Pt 5d states was determined by the measurements of L_3 absorption edge and L_5 emission lines. Figure 5.7 shows the experimentally measured RIXS spectra for Pt/SiO_2 and PtP_2/SiO_2 as 2-D contour plot maps, where the energy transfer (ΔE) is as function of the incident photon energy (Ω). The location of maximum intensity can be used to determine the difference between the average energies of the filled and unfilled 5d states. The maximum intensity of Pt catalysts occurs at Ω = 11564.2 eV with ΔE of 2.7 eV in accordance with literature.7, 32 Upon forming the PtP_2 alloy, the maximum RIXS intensity shifts to higher Ω of 11567.0 eV and higher energy transfer, ca. ΔE 5.5 eV, or 2.8 eV larger than that in Pt NPs. Since the energy of unfilled valence states in PtP_2 was 1.5 eV higher than that in the monometallic Pt confirmed by XANES in Figure 5.2, the energy of filled 5d valence states in PtP2 was 1.3 eV lower than that in Pt NPs, as shown in Figure 5.8.

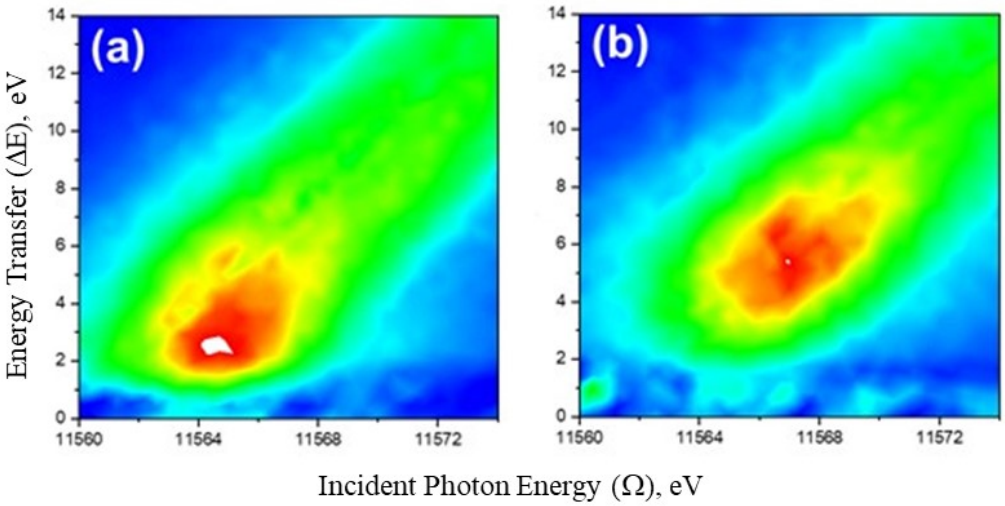

Fig. 5.7. L_3 RIXS of planes of (a) Pt/SiO_2 and (b) PtP_2/SiO_2.

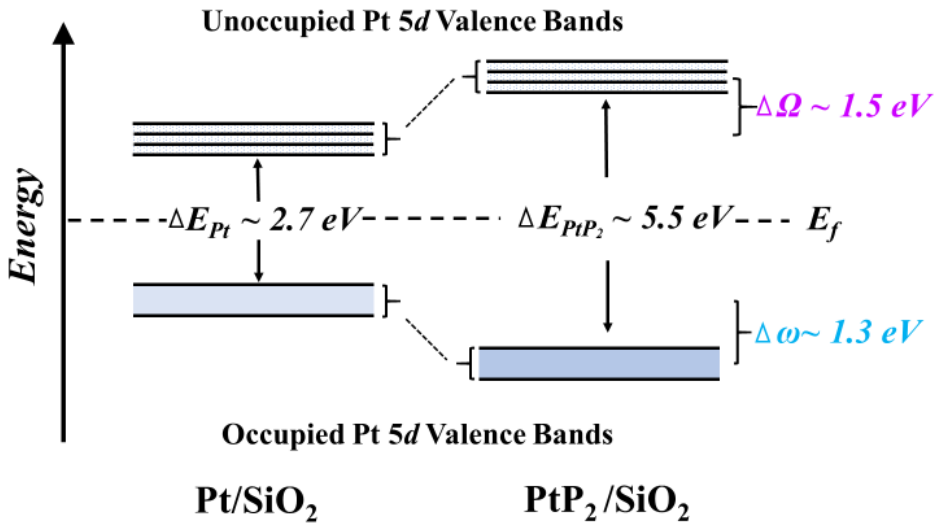

Fig. 5.8. Energy level diagram for Pt 5d valence bands in Pt/SiO_2 and PtP_2/SiO_2.

5.4.7 *In situ* CO-IR and CO chemisorption

In situ CO-IR was performed on these Pt-P catalysts after reduction at 550 °C in 5% $H2_2$, and the spectra are shown in Figure 5.9. The major peak in the spectra of Pt-P-1 and Pt-P-4 at about 2075 cm^{-1} is identical to linearly absorbed CO on Pt NPs. [140–142] For these catalysts, there was little bridge bonded CO in the DRIFT spectra. In the DRIFT spectrum of Pt-P-50 catalyst, there are no obvious peaks, suggesting there is little absorbed CO.

To further quantify the absorption of CO, chemisorption measurements were conducted on all Pt-P catalysts together with reference Pt/SiO_2, and the metal dispersion was also obtained assuming linearly absorbed CO (Table 5.3). Pt/SiO_2 had a dispersion of 45%, consistent with 2 nm Pt NPs. As the P loading increased, the dispersion decreased from Pt-P-1 of 31% to Pt-P-4 of 23%. For Pt-P-20 and Pt-P-50 catalysts, the dispersion decreased sharply to 3.0% and 4.9%, respectively, indicating little absorbed CO in the samples with a large excess of P.

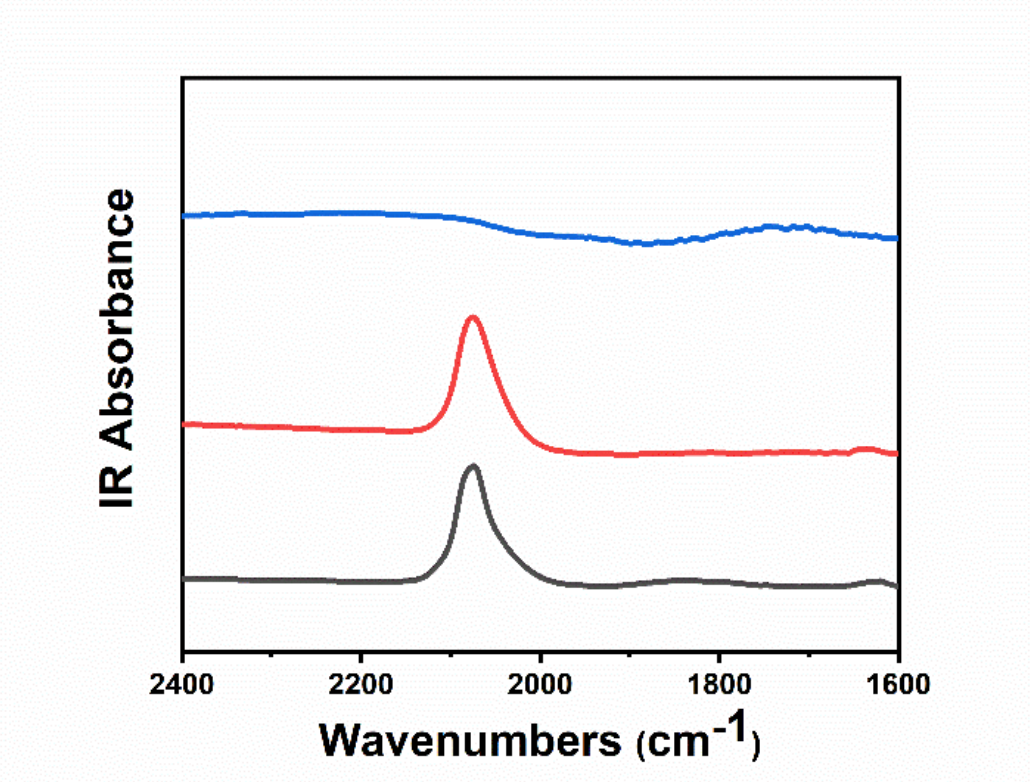

Fig. 5.9. CO DRIFT spectra of Pt-P-1(black line), Pt-P-4 (red line) and Pt-P-50 (blue line) catalysts.

5.4.8 Catalysis

Figure 5.10 shows the initial selectivity vs conversion of these supported Pt catalysts for PDH reactions at 550 °C in 5% C3H8 and 5% H_2 balanced with N_2. The addition of H_2 to the reaction gases is a more severe test of the catalyst performance since the presence of H2 promotes the hydrogenolysis reaction. For further comparison, the selectivity of these Pt catalysts at 25% conversion were obtained (Table 5.3). For the reference Pt/SiO_2 catalyst, the selectivity decreased rapidly from 82% to 63% as the conversion increased from 8% to 27%, which is consistent with literature. [35,38] In contrast, the Pt-P catalysts showed a better performance for PDH and achieved high olefin selectivity, as shown in Table 5.3. For Pt-P-50 catalyst, the propylene selectivity remains about 97% at 25% propane conversion. The Pt-P-20 shows almost

the same performance as Pt-P-50, where the selectivity was approximately 96% at 25% conversion.

For Pt-P-4 catalyst, the selectivity decreased slightly to 93% with increasing the conversion up to about 40%. The selectivity of Pt-P-1 shows the same trend as Pt-P-4 under varying conversions, but with slightly lower selectivity. For instance, the 91% selectivity of Pt-P-1 is slightly lower than 96% of Pt-P-4 at 25% conversion.

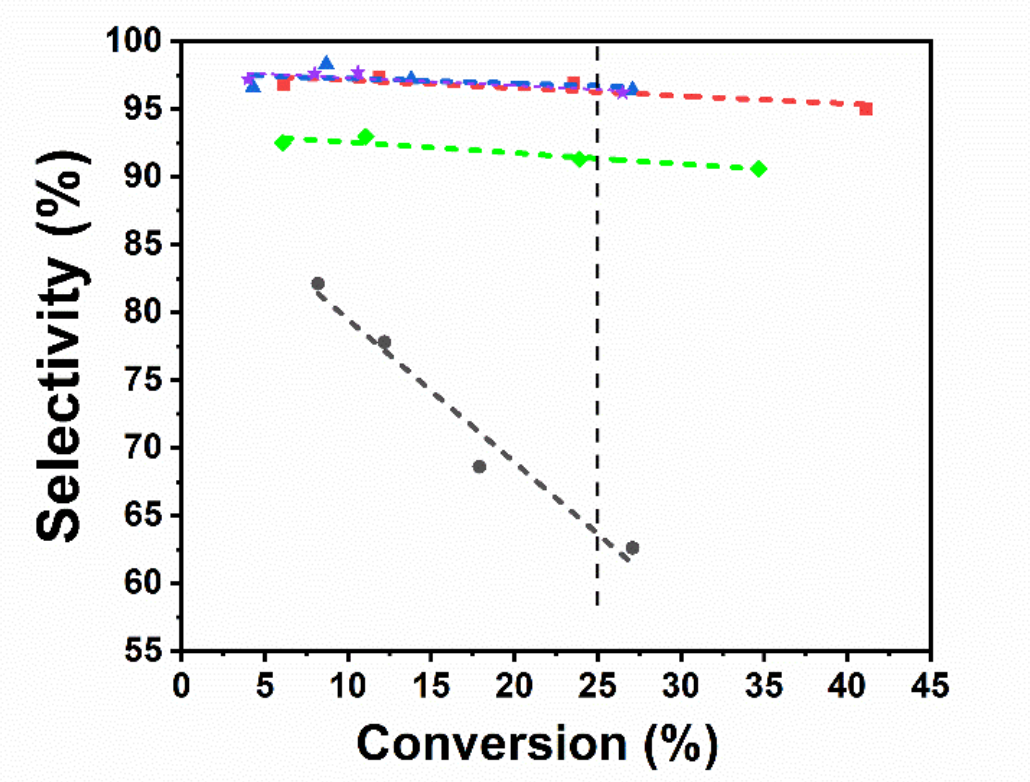

Fig. 5.10. Initial selectivity vs conversion in PDH after reduction at 550 °C in 5% C_3H_8, 5% H_2 balance with N2 for Pt/SiO_2 (black), Pt-P-1(green), Pt-P-4 (red), Pt-P-20 (purple) and Pt-P-50 (blue).

Since Pt is the only active site, to compare the PDH activities of these catalysts, the rates per mole of Pt (based on all 2 wt% Pt), and turnover rate (TOR) based on CO chemisorption were calculated and are listed in Table 5.3. The propane conversion rate of Pt/SiO_2 is 0.087 mol/(s*mol catalyst), and the TORCO is 0.19 s^{-1}. The TORs of Pt-P-1 and Pt-P-2 are 0.32 s^{-1} and are similar to that of Pt NPs (Pt/SiO_2). With

Table 5.3.
Propane dehydrogenation performed at 550°C in 5% C_3H_8, 5% H_2 balance with N_2

Catalyst	% S_{25}^a	Rate (mol/(s*mol catalyst))	% Dispersion	TOR (s^{-1})
$2Pt/SiO_2$	64	0.088	45	0.20
Pt-P-1	91	0.10	31	0.32
Pt-P-2	93	0.086	27	0.32
Pt-P-4	96	0.042	23	0.18
Pt-P-20	96	0.007	3.0	0.23
Pt-P-50	97	0.012	4.9	0.24

[a]S_{25}: propylene selectivity at 25% conversion of propane

the increasing P loadings, both rate and metal dispersion decrease. For Pt-P-4, the rate/mole Pt and metal dispersion are almost half of Pt/SiO_2; however, the TORCO of 0.18 s^{-1} is again similar to Pt NPs. Both Pt-P-20 and Pt-P-50, which contain a large excess of P, show much lower rates/mole Pt than that of Pt/SiO_2. The former also have lower metal dispersions, thus, also have the similar TORs.

5.4.9 NP surface characterization

These catalysts differ in selectivity, rate per g Pt, CO chemisorption capacity, etc. Each of these is determined by the NP surface composition. To better understand these differences, the surface structure of the NPs was determined by *in situ* XAS. [35,38,63] The surface of the NPs is determined by taking the difference in the EXAFS of the reduced minus the surface oxidized catalyst, which results from air exposure at room temperature. Since the subsurface atoms remain unchanged, the difference spectrum is due to the loss of surface Pt-X neighbor atoms plus the formation of Pt-O bonds. The spectra of reduced and oxidized Pt-P-20 and Pt-P-1 are shown in Figure 5.11. In Figure 5.11a, there is no difference in these spectra for Pt-P-20 indicating that there is little surface Pt, consistent with the CO chemisorption and low rates per gram Pt. Similar results were obtained for Pt-P-50. For Pt-P-1, however, upon

exposure to air at RT, there are loss of Pt-Pt and Pt-P surface atoms with formation of Pt-O bonds. Because of the overlaps of these peaks and the uncertainty in the fits, it is difficult to quantify the changes in the surface of the NPs from direct fits of the total spectra. However, since the interior atoms of particles are not oxidized, the difference spectrum represents only the changes of the surface bonds. Figure 5.11c shows the difference EXAFS spectrum of Pt-P-1, where the changes in the surface composition is better resolved and can be more reliably fit. The fits of difference spectra with Pt-Pt, Pt-P and Pt-O scatting pairs were necessary to quantify the surface composition, as shown in Table 5.4. Note that due to the subtraction of the oxidized sample, the phase of the Pt-O scattering pair is π-radians out of phase compared to a standard spectrum.

For oxidized Pt-P-1 catalyst (Figure 5.11b), the first peak is located between 1.5 Å and 2 Å, which is the region where Pt-O and Pt-P scattering overlap. The metallic peaks between 2 Å and 3 Å in the oxidized catalyst indicate the presence of interior Pt particles which are not oxidized, and their lower magnitude likely suggests the loss of surface Pt-Pt bonds. The fit of the difference spectrum gives a CN_{Pt-Pt} of 1.22 at 2.76 Å, CNPt-P of 0.27 at 2.35 Å, and CN_{Pt-O} of 0.44 at 1.98 Å. The difference EXAFS of Pt-P-1 is consistent with surface Pt-P and Pt (Table 5.4); however, there are more Pt-Pt bonds than Pt-P bonds.

Similarly, for Pt-P-4 catalyst, a good fit of difference EXAFS was obtained with a CN_{Pt-Pt} of 0.74 at 2.76 Å, CN_{Pt-P} of 0.86 at 2.32 Å, and CN_{Pt-O} of 0.28 at 2.03 Å. For Pt-P-4, the surface still consists of Pt-Pt and Pt-P bonds; however, the number of surface Pt-P is greater than the number of Pt-Pt bonds.

As indicated in the surface XAS results, the fraction of surface Pt-Pt bonds decreased, and that of Pt-P bonds increases with increasing the P loading. From the reduced EXAFS, there are no Pt-Pt bonds when there is enough P to form a full PtP_2 phase as in Pt-P-20 and Pt-P-50. The identical EXAFS of the reduced and oxidized catalyst suggest that there is little exposed Pt in these samples, perhaps due to covering by excess P.

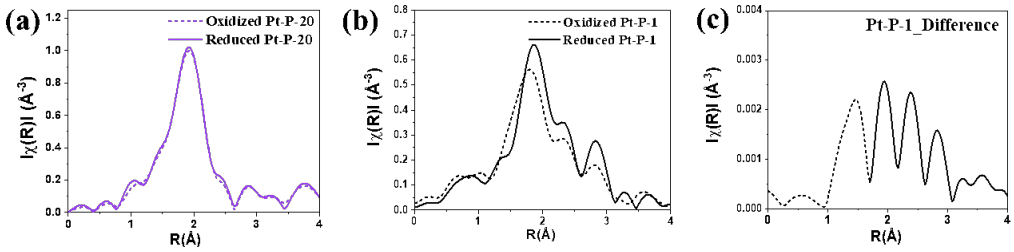

Fig. 5.11. FT magnitudes of the EXAFS spectra for: (a) Reduced and oxidized Pt-P-20, (b) Reduced and oxidized Pt-P-1 and (c) Difference EXAFS of Pt-P-1 with Pt-O peaks (dashed line) and Pt-P and Pt-Pt peaks (solid line).

Table 5.4.
Difference XAS fitting parameters for the surface composition

Name	Scattering Path	R(Å)	CN (s^{-1})
Pt-P-1	Pt-Pt	2.76	1.22
	Pt-P	2.35	0.27
	Pt-O	1.98	0.44
Pt-P-4	Pt-Pt	2.76	0.74
	Pt-P	2.32	0.86
	Pt-O	2.03	0.28
Pt-P-20	Pt-Pt, Pt-P, Pt-O	nd[a]	nd

[a]nd: not detected.

5.5 Discussion

In this study, supported Pt-P catalysts were prepared with different loadings of P and by two different synthesis methods. These procedures are similar to industrial synthesis methods and are suitable for larger scale preparations. In the first method, catalysts Pt-P-(1-4), small Pt NPs were first prepared. The method of preparation of the initial Pt/SiO_2 generally gives NPs of about 1-3 nm. [143] This was followed by addition of H3PO4 and a second reduction. From XRD only Pt NPs were detected; however, the EXAFS indicated that there were both Pt-Pt and Pt-P bonds. In addition, the surface EXAFS indicates that there are also Pt-Pt and Pt-P bonds.

The number of Pt-P bonds increases with the increasing content of H_3PO_4 in the synthesis.

The structure of PtP_2 has a cubic structure with Pt-P bonds at 2.36 Å and a Pt-Pt distance of 4.02 Å, as shown in Figure 5.4b. From the HRSTEM images, the structures of Pt-P-2 and Pt-P-4 are consistent with a PtP_2 shell, or partial shell, with Pt core (Figure 5.5). The XPS are also consistent with a mixture of these two phases (Pt and PtP_2). The presence of surface Pt-Pt bonds at 2.76 Å in Pt-P-(1-4) as well as the shorter Pt-P bonds (2.31-2.32 Å) due to the surface contraction suggest partial coverage of Pt NPs by PtP_2 with small areas of exposed monometallic Pt.

The second method of synthesis of Pt phosphide catalysts was prepared by sequential impregnation of $Pt(NH_3)_4^{2+}$, drying and then addition of a large excess of H3PO4. Calcination at 600 °C followed by reduction leads to a PtP_2 phase as confirmed by *in situ* synchrotron XRD (Figure 5.4), HRSTEM (Figure 5.5c) and EXAFS (Figure 5.3b). In this structure, the Pt atoms are isolated from other Pt atoms by P atoms (Figure 5.4b). While the isolated Pt atoms in this structure are highly selective, the rate per g Pt, CO chemisorption and reactivity of surface Pt to air, all suggest that the excess P in these catalyst blocks most of the surface Pt sites. While most of the surface Pt is not accessible, the sites that are exposed have a TOR comparable to that of other Pt catalysts.

Bimetallic Pt catalysts (Pt_1Zn_1 [2], Pt_1Sb_1 [64], Pt_3Co8_8, Pt_3Bi [99], Pt_3Cr [35], Pt_3Mn [62] and Pt_3V [88]) normally form cubic intermetallic alloys, often Au_3Cu and AuCu structure types. The high olefin selectivity for alkane dehydrogenation obtained with bimetallic Pt NPs is due to small Pt ensembles, or isolated Pt atoms caused by the addition of a non-catalytic promoter. [89,121] In addition, in alloy catalysts there is often a decrease in the binding energy of adsorbates and reaction intermediates, which decreases surface coverage, increases selectivity, rates and reduces the deactivation rate. Similarly, once the PtP_2 ordered structures covers the catalysts surface, the Pt atoms are geometrically isolated by P_2, where the Pt-Pt bonds distance of 4.02 Å is much longer than that in metallic Pt NPs of 2.78 Å. These isolated Pt sites inhibit

the structure sensitive hydrogenolysis, while maintaining the sites for the structured insensitive dehydrogenation, thus display high olefin selectivity for PDH. While the selectivity is high and the PtP_2 NP size prepared by this method is small, the rate is too low to be an effective catalyst. Thus, there is an opportunity to develop an alternative synthesis method that could give excellent activity as well as selectivity, perhaps, by limiting the amount of excess P in the NPs.

While the PtP_2 has a nearly ideal geometric structure to catalyze structure insensitive and inhibit structure sensitive reactions, these catalysts also show a large change in the energy of the Pt valence orbitals. Since XANES and RIXS are bulk techniques, these methods measure every atom in the sample. However, catalysis is determined by the composition of the NP surface. Thus, in order to determine the effect of P on the electronic properties, which affect catalysis, one has to prepare a pure phase structure where the catalytic surface is identical to that of the bulk. [88] Thus, the electronic modification to the filled and unfilled Pt 5d orbitals was determined for Pt-P-50 with a full PtP_2 structure. As shown in Figure 5.2, the formation of PtP_2 particles significantly increases the energy of the XANES spectrum by 1.5 eV. RIXS also indicate the energy of filled 5d orbitals decreased by about 1.5 eV. Thus, the increase in the XANES energy is nearly the same as the decrease in the energy of the filled orbitals. The effect of P on the energy of the Pt valence orbitals is similar to that in previously studied bimetallic Pt catalysts. [35, 38, 42, 69, 88] This decrease in the energy of the filled 5d orbitals, as shown in Figure 5.8, would be expected to lead to weaker Pt-adsorbate and reaction intermediate bond energies compared to metallic Pt. For comparison the decrease in energy of the filled 5d orbitals in PtP_2 NPs are larger than those observed for many bimetallic Pt catalysts, including 0.7 eV shift in Pt_3Co [38], 0.6 eV shift in Pt_3Cr [35], 0.9 eV shift in Pt_1Zn_1 [2], 0.4 eV shift in Pt_3V [88] and 1.1 eV shift in Pt_3In [69] catalysts. These large changes in the energy of the Pt 5d orbitals is especially surprising since one would not expect strong bonding with P 3p orbitals due to the orthogonal orbital symmetries. The theoretical

justification for these large changes in the energy of the Pt 5d orbitals remains to be explained.

5.6 Conclusion

Two synthesis methods suitable for large scale synthesis of 2-3 nm supported metal phosphide catalysts was presented. The addition of P to supported Pt catalysts leads to the formation of PtP_2 ordered structure. As the P loading increased, the catalysts changed from partial surface PtP_2 to Pt@PtP_2 core-shell structure and then to full PtP_2 structure. All show high olefin selectivity for propane dehydrogenation. Compared with bimetallic Pt catalysts, although P is not a metal, Pt atoms are geometrically isolated by P_2 atoms in PtP_2 structure. Meanwhile, P addition leads to wider energy gap between filled and unfilled Pt 5d orbitals in comparison with bimetallic Pt catalysts. These electronic effects are suggested to decrease in bond strength of adsorbates and reaction intermediates. These findings suggest that the other (supported) noble metal phosphides, like Ru-P, Ir-P and Pd-P might be selective for alkane dehydrogenation and potentially other catalytic reactions.

5.7 Acknowledgement

Use of the Advanced Photon Source was supported by the U.S. Department of Energy Office of Basic Energy Sciences under contract no. DE-AC02-06CH11357. MRCAT operations, beamlines 10-BM and 10-ID, are supported by the Department of Energy and the MRCAT member institutions. The authors also acknowledge the use of beamline 11-ID-C.

6. SUMMARY

This research in this thesis focused on ordered noble metal catalyst including intermetallic alloys and metal phosphides, for example, Pt-Bi, Pt-P, and SMSI oxide catalysts of Pt-NbOx, Pt-TiOx, Pt-CeOx. Synthesis of 2-3 nm nanoparticles (NPs) were achieved by impregnation methods by using appropriate precursor, support and pH to maximize the dispersion of the nanoparticles. The NP size was determined by transmission electron microscopy, CO chemisorption and olefin hydrogenation rates. The structure is characterized by in situ synchrotron X-ray diffraction and *in situ* X-ray absorption spectroscopy, which provided information about the crystal phase and spatial distribution over the nanoparticles. Electronic properties were also studied by *in situ* spectroscopies like X-ray photoelectron spectroscopy (XPS), X-ray absorption near edge structure (XANES) and resonant inelastic X-ray scattering (RIXS), which measures the 5d valance electronic structure, which is directly correlated to the bonding and catalytic properties.

Pt_3Bi was shown in chapter 2 to catalyze NOCM at relative low temperatures with 5% conversion to C_2; while, previous studies showed that Pt_3Sn is also stable for NOCM [11], but much less active (0.1% conversion) than the catalysts in this thesis. Therefore, it was concluded that intermetallic alloys could be active for NOCM. It was shown that requires high reaction temperatures since this reaction is thermodynamically unfavorable at low temperatures. For example, equilibrium calculations are shown in Figure 6.1 (A) and indicates that the equilibrium conversion at 800 K is ¡1%, while at 1200 K the equilibrium conversion to ethylene is about 20%. On the other hand, at higher pressure of methane leads to higher reaction rates; however, the equilibrium conversion to ethylene, as shown in Figure 6.1 (B), decreases as the partial pressure of methane increases. Equilibrium conversion to ethylene at 5 atm and 1200 K is 12%. Thus, temperatures above 1200 K would be needed for the re-

action. Pt-Bi/SiO_2 is not a stable catalyst at these high temperatures due to the reduction of Bi_2O_3, which covers the surface of the Pt nanoparticles deactivating the catalyst. With early transitional metal promoters for alloys with Pt such as Cr [35], Mn [63], Fe [97], the oxides are much harder to reduce leading to higher stability at high temperatures; therefore, these alloys may be good catalysts for NOCM at high temperatures, and should be further studied.

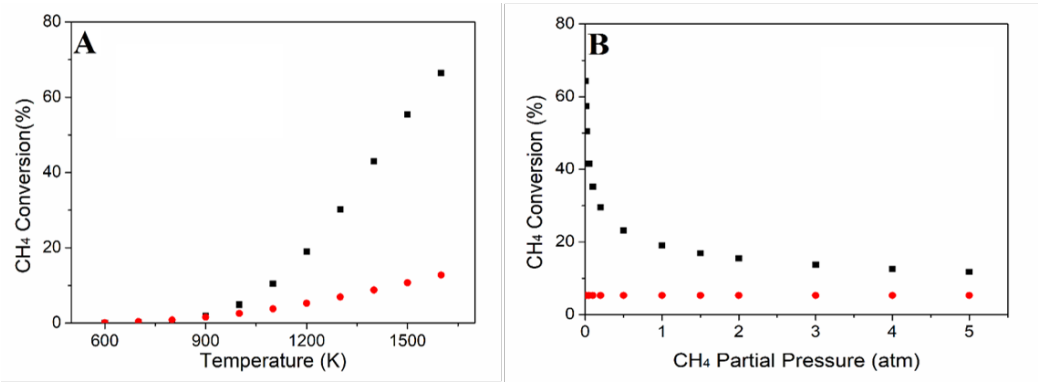

Fig. 6.1. Equilibrium methane conversion to ethane (red) and ethylene (black) as an effect of A) Temperature on at 1 atm methane partial pressure, B) Pressure at 1200 K.

Previous studies by Xie et al. used Pt/CeO2 at 900-1000 (1173-1273 K) for NOCM to obtain conversions as high as 20% with high C_2+ selectivity. The catalysts were thought to be single site Pt^{2+} sites, i.e., non-metallic Pt, which are stabilized by CeO_2. An *in situ* structural determination of this catalyst, however, showed that Pt NPs were formed. In addition, at these high temperature, the Pt NPs are partially covered by the CeO_2 support, i.e., strong metal support interaction (SMSI). The SMSI Pt/CeO_2 catalyst was also shown to be have a different olefin selectivity for propane dehydrogenation than non-SMSI supported Pt NPs, for example, Pt/SiO_2. Although the Pt/CeO_2 had a small fraction of exposed metallic Pt sites, it was shown that these are not the origin of the reported NOCM catalytic performance of Pt/CeO_2. Rather, thermal cracking and supports like silica (without catalytic metals) had similar performance of the Pt/CeO_2. These results suggest that at very high reaction

temperatures that are required for higher CH_4 conversions, thermal reactions dominate the product selectivity. It is recommended that further studies be conducted to understand non-catalytic, thermal NOCM.

For the SMSI Pt/CeO_2 it was difficult to utilize state of the art characterizations to determine the fundamental nature of the role of the support for modification of Pt catalysis, for example, for propane dehydrogenation at much lower temperature than NOCM. Thus, Pt catalysts with SMSI oxides (TiO_2 and Nb_2O_5) were synthesized, which were much more olefin selective than non-SMSI Pt NPs, similar to the changes in catalytic properties of Pt NPs on CeO_2. For the former, *in situ* characterizations showed identical structure and electronic properties to non-SMSI Pt/SiO_2 catalysts despite the differences in catalytic performance. It was concluded that the SMSI catalytic performance was due to partial coverage of the Pt NPs from the SMSI oxide leading to small ensembles, which inhibit hydrogenlysis by-products. Despite these new insights, there is still much that is unknown. For example, do the SMSI oxides selectively cover certain sites (e.g., corners, edges), or are randomly distributed? In addition, since the oxide has to migrate from the support to cover the NPs, will the fraction of surface that is covered be dependent on the NP size and/or SMSI oxide loading? In order to further understand the catalytic sites in SMSI catalysts, further studies with Pd-SMSI catalysts should be studied. CO adsorption on Pd NPs has linear, bridging and 3-fold surface bonding, which can be observed by infrared spectroscopy. For example, Wu *et al.* used CO infrared to show isolated Pd sites in the Pd-In catalysts [62]; while the IR spectrum of Pd NPs was primarily 3-fold adsorbed CO. Therefore, similar techniques could be used to understand the coverage of Pd NPs in SMSI catalysts. The changes in IR spectra can be used to determine if there are corners, i.e., linear CO, bridged sites (NP edges) or 3 fold sites indicating flat surfaces are exposed. Based on the remaining exposed sites, the location of the SMSI oxide could be determined. Alternatively, if the IR spectra before and after SMSI that are identical, this would indicate random SMSI deposition. Also, is the fraction of NP coverage the same for all sizes of Pd NPs, or is it higher for smaller

sizes? Both changes in coverage and types of remaining exposed surface sites would provide additional insight into the SMSI process and changes in catalyst surface sites. Catalytic properties, chemisorption capacities and IR spectroscopy can potentially answer these questions. The ultimate goal of this research would be to further improve the catalytic performance and stability by incorporation of oxide/support promoters beyond what is possible with alloys.

During this research good progress has been made in the understanding of structure of the active metal, promoters and support for NOCM and alkane dehydrogenation. In addition, new ideas have been develop which hold promise for further progress and eventually commercial production of fuels from light shale gas alkanes.

REFERENCES

REFERENCES

[1] B. Hu, N. M. Schweitzer, G. Zhang, S. J. Kraft, D. J. Childers, M. P. Lanci, J. T. Miller, and A. S. Hock, "Isolated feii on silica as a selective propane dehydrogenation catalyst," *Acs Catalysis*, vol. 5, no. 6, pp. 3494–3503, 2015.

[2] V. J. Cybulskis, S. U. Pradhan, J. J. Lovón-Quintana, A. S. Hock, B. Hu, G. Zhang, W. N. Delgass, F. H. Ribeiro, and J. T. Miller, "The nature of the isolated gallium active center for propane dehydrogenation on ga/sio 2," *Catalysis Letters*, vol. 147, no. 5, pp. 1252–1262, 2017.

[3] J. J. Siirola, "The impact of shale gas in the chemical industry," *AIChE Journal*, vol. 60, no. 3, pp. 810–819, 2014.

[4] K. A. Bullin and P. E. Krouskop, "Compositional nal variety complicates processing plans for us shale gas," *Oil & Gas Journal*, vol. 107, no. 10, pp. 50–55, 2009.

[5] J. J. Sattler, J. Ruiz-Martinez, E. Santillan-Jimenez, and B. M. Weckhuysen, "Catalytic dehydrogenation of light alkanes on metals and metal oxides," *Chemical reviews*, vol. 114, no. 20, pp. 10 613–10 653, 2014.

[6] D. W. Rankin, "Crc handbook of chemistry and physics, edited by david r. lide," 2009.

[7] C. Karakaya and R. J. Kee, "Progress in the direct catalytic conversion of methane to fuels and chemicals," *Progress in Energy and Combustion Science*, vol. 55, pp. 60–97, 2016.

[8] T. Ito and J. H. Lunsford, "Synthesis of ethylene and ethane by partial oxidation of methane over lithium-doped magnesium oxide," *Nature*, vol. 314, no. 6013, pp. 721–722, 1985.

[9] S. Arndt, G. Laugel, S. Levchenko, R. Horn, M. Baerns, M. Scheffler, R. Schlögl, and R. Schomäcker, "A critical assessment of li/mgo-based catalysts for the oxidative coupling of methane," *Catalysis Reviews*, vol. 53, no. 4, pp. 424–514, 2011.

[10] R. Ghose, H. T. Hwang, and A. Varma, "Oxidative coupling of methane using catalysts synthesized by solution combustion method: Catalyst optimization and kinetic studies," *Applied Catalysis A: General*, vol. 472, pp. 39–46, 2014.

[11] D. Gerceker, A. H. Motagamwala, K. R. Rivera-Dones, J. B. Miller, G. W. Huber, M. Mavrikakis, and J. A. Dumesic, "Methane conversion to ethylene and aromatics on ptsn catalysts," *ACS Catalysis*, vol. 7, no. 3, pp. 2088–2100, 2017.

[12] L. Wang, L. Tao, M. Xie, G. Xu, J. Huang, and Y. Xu, "Dehydrogenation and aromatization of methane under non-oxidizing conditions," *Catalysis Letters*, vol. 21, no. 1-2, pp. 35–41, 1993.

[13] Y. Zhang, M. Kidder, R. E. Ruther, J. Nanda, G. S. Foo, Z. Wu, and C. K. Narula, "Promotional effects of in on non-oxidative methane transformation over mo-zsm-5," *Catalysis Letters*, vol. 146, no. 10, pp. 1903–1909, 2016.

[14] C. H. Tempelman and E. J. Hensen, "On the deactivation of mo/hzsm-5 in the methane dehydroaromatization reaction," *Applied Catalysis B: Environmental*, vol. 176, pp. 731–739, 2015.

[15] L. Chen, L. Lin, Z. Xu, T. Zhang, and X. Li, "Promotional effect of pt on non-oxidative methane transformation over mo-hzsm-5 catalyst," *Catalysis letters*, vol. 39, no. 3-4, pp. 169–172, 1996.

[16] F. Solymosi, J. Cserényi, A. Szőke, T. Bánsági, and A. Z. Oszkó, "Aromatization of methane over supported and unsupported mo-based catalysts," *Journal of Catalysis*, vol. 165, no. 2, pp. 150–161, 1997.

[17] N. Kosinov, F. J. Coumans, E. A. Uslamin, A. S. Wijpkema, B. Mezari, and E. J. Hensen, "Methane dehydroaromatization by mo/hzsm-5: mono-or bifunctional catalysis?" *ACS Catalysis*, vol. 7, no. 1, pp. 520–529, 2017.

[18] C. Karakaya, H. Zhu, and R. J. Kee, "Kinetic modeling of methane dehydroaromatization chemistry on mo/zeolite catalysts in packed-bed reactors," *Chemical Engineering Science*, vol. 123, pp. 474–486, 2015.

[19] I. Lezcano-González, R. Oord, M. Rovezzi, P. Glatzel, S. W. Botchway, B. M. Weckhuysen, and A. M. Beale, "Molybdenum speciation and its impact on catalytic activity during methane dehydroaromatization in zeolite zsm-5 as revealed by operando x-ray methods," *Angewandte Chemie International Edition*, vol. 55, no. 17, pp. 5215–5219, 2016.

[20] S.-T. Wong, Y. Xu, L. Wang, S. Liu, G. Li, M. Xie, and X. Guo, "Methane and ethane activation without adding oxygen: promotional effect of w in mo-w/hzsm-5," *Catalysis letters*, vol. 38, no. 1-2, pp. 39–43, 1996.

[21] Y. Shu, Y. Xu, S.-T. Wong, L. Wang, and X. Guo, "Promotional effect of ru on the dehydrogenation and aromatization of methane in the absence of oxygen over mo/hzsm-5 catalysts," *Journal of Catalysis*, vol. 170, no. 1, pp. 11–19, 1997.

[22] R. Kojima, S. Kikuchi, H. Ma, J. Bai, and M. Ichikawa, "Promotion effects of pt and rh on catalytic performances of mo/hzsm-5 and mo/hmcm-22 in selective methane-to-benzene reaction," *Catalysis letters*, vol. 110, no. 1-2, pp. 15–21, 2006.

[23] Y. Xu, J. Wang, Y. Suzuki, and Z.-G. Zhang, "Improving effect of fe additive on the catalytic stability of mo/hzsm-5 in the methane dehydroaromatization," *Catalysis today*, vol. 185, no. 1, pp. 41–46, 2012.

[24] A. K. Aboul-Gheit, A. E. Awadallah, A. A. Aboul-Enein, and A.-L. H. Mahmoud, "Molybdenum substitution by copper or zinc in h-zsm-5 zeolite for catalyzing the direct conversion of natural gas to petrochemicals under non-oxidative conditions," *Fuel*, vol. 90, no. 10, pp. 3040–3046, 2011.

[25] M. Belgued, P. Pareja, A. Amariglio, and H. Amariglio, "Conversion of methane into higher hydrocarbons on platinum," *Nature*, vol. 352, no. 6338, pp. 789–790, 1991.

[26] F. Viñes, Y. Lykhach, T. Staudt, M. P. Lorenz, C. Papp, H.-P. Steinrück, J. Libuda, K. M. Neyman, and A. Görling, "Methane activation by platinum: Critical role of edge and corner sites of metal nanoparticles," *Chemistry–A European Journal*, vol. 16, no. 22, pp. 6530–6539, 2010.

[27] C. Yang, Z. Wu, G. Zhang, H. Sheng, J. Tian, Z. Duan, H. Sohn, A. J. Kropf, T. Wu, T. R. Krause *et al.*, "Promotion of pd nanoparticles by fe and formation of a pd3fe intermetallic alloy for propane dehydrogenation," *Catalysis Today*, vol. 323, pp. 123–128, 2019.

[28] M. Sankar, N. Dimitratos, P. J. Miedziak, P. P. Wells, C. J. Kiely, and G. J. Hutchings, "Designing bimetallic catalysts for a green and sustainable future," *Chemical Society Reviews*, vol. 41, no. 24, pp. 8099–8139, 2012.

[29] S. Furukawa and T. Komatsu, "Intermetallic compounds: promising inorganic materials for well-structured and electronically modified reaction environments for efficient catalysis," *ACS Catalysis*, vol. 7, no. 1, pp. 735–765, 2017.

[30] J. Sattler, I. Gonzalez-Jimenez, A. Mens, M. Arias, T. Visser, and B. Weckhuysen, "Operando uv-vis spectroscopy of a catalytic solid in a pilot-scale reactor: deactivation of a cro x/al 2 o 3 propane dehydrogenation catalyst," *Chemical Communications*, vol. 49, no. 15, pp. 1518–1520, 2013.

[31] P. Sun, G. Siddiqi, W. C. Vining, M. Chi, and A. T. Bell, "Novel pt/mg (in)(al) o catalysts for ethane and propane dehydrogenation," *Journal of catalysis*, vol. 282, no. 1, pp. 165–174, 2011.

[32] J. Clarke and J. Rooney, "Stereochemical approaches to mechanisms of hydrocarbon reactions on metal catalysts," *Adv. Catal*, vol. 25, p. 125, 1976.

[33] B. V. Vora, "Development of dehydrogenation catalysts and processes," *Topics in Catalysis*, vol. 55, no. 19-20, pp. 1297–1308, 2012.

[34] L. Shi, G.-M. Deng, W.-C. Li, S. Miao, Q.-N. Wang, W.-P. Zhang, and A.-H. Lu, "Al2o3 nanosheets rich in pentacoordinate al3+ ions stabilize pt-sn clusters for propane dehydrogenation," *Angewandte Chemie International Edition*, vol. 54, no. 47, pp. 13 994–13 998, 2015.

[35] N. J. LiBretto, C. Yang, Y. Ren, G. Zhang, and J. T. Miller, "Identification of surface structures in pt3cr intermetallic nanocatalysts," *Chemistry of Materials*, vol. 31, no. 5, pp. 1597–1609, 2019.

[36] G. Siddiqi, P. Sun, V. Galvita, and A. T. Bell, "Catalyst performance of novel pt/mg (ga)(al) o catalysts for alkane dehydrogenation," *Journal of Catalysis*, vol. 274, no. 2, pp. 200–206, 2010.

[37] Z. Ma, Z. Wu, and J. T. Miller, "Effect of cu content on the bimetallic pt–cu catalysts for propane dehydrogenation," *Catalysis, Structure & Reactivity*, vol. 3, no. 1-2, pp. 43–53, 2017.

[38] L. G. Cesar, C. Yang, Z. Lu, Y. Ren, G. Zhang, and J. T. Miller, "Identification of a pt3co surface intermetallic alloy in pt–co propane dehydrogenation catalysts," *ACS Catalysis*, vol. 9, no. 6, pp. 5231–5244, 2019.

[39] H. N. Pham, J. J. Sattler, B. M. Weckhuysen, and A. K. Datye, "Role of sn in the regeneration of pt/γ-al2o3 light alkane dehydrogenation catalysts," *ACS catalysis*, vol. 6, no. 4, pp. 2257–2264, 2016.

[40] E. Jimenez-Izal, H. Zhai, J.-Y. Liu, and A. N. Alexandrova, "Nanoalloying mgo-deposited pt clusters with si to control the selectivity of alkane dehydrogenation," *ACS Catalysis*, vol. 8, no. 9, pp. 8346–8356, 2018.

[41] J. Zhang, Y. Deng, X. Cai, Y. Chen, M. Peng, Z. Jia, Z. Jiang, P. Ren, S. Yao, J. Xie *et al.*, "Tin-assisted fully exposed platinum clusters stabilized on defect-rich graphene for dehydrogenation reaction," *ACS Catalysis*, vol. 9, no. 7, pp. 5998–6005, 2019.

[42] V. J. Cybulskis, B. C. Bukowski, H.-T. Tseng, J. R. Gallagher, Z. Wu, E. Wegener, A. J. Kropf, B. Ravel, F. H. Ribeiro, J. Greeley *et al.*, "Zinc promotion of platinum for catalytic light alkane dehydrogenation: insights into geometric and electronic effects," *ACS Catalysis*, vol. 7, no. 6, pp. 4173–4181, 2017.

[43] J. Jones, H. Xiong, A. T. DeLaRiva, E. J. Peterson, H. Pham, S. R. Challa, G. Qi, S. Oh, M. H. Wiebenga, X. I. P. Hernández *et al.*, "Thermally stable single-atom platinum-on-ceria catalysts via atom trapping," *Science*, vol. 353, no. 6295, pp. 150–154, 2016.

[44] P. Xie, T. Pu, A. Nie, S. Hwang, S. C. Purdy, W. Yu, D. Su, J. T. Miller, and C. Wang, "Nanoceria-supported single-atom platinum catalysts for direct methane conversion," *ACS Catalysis*, vol. 8, no. 5, pp. 4044–4048, 2018.

[45] P. Schwach, X. Pan, and X. Bao, "Direct conversion of methane to value-added chemicals over heterogeneous catalysts: challenges and prospects," *Chemical reviews*, vol. 117, no. 13, pp. 8497–8520, 2017.

[46] T. Ito, J. Wang, C. H. Lin, and J. H. Lunsford, "Oxidative dimerization of methane over a lithium-promoted magnesium oxide catalyst," *Journal of the American Chemical Society*, vol. 107, no. 18, pp. 5062–5068, 1985.

[47] B. Yingli, Z. Kaiji, J. Yutao, T. Chiwen, and Y. Xiangguong, "Catalytic oxidative coupling of methane over alkali, alkaline earth and rare earth metal oxides," *Applied catalysis*, vol. 39, pp. 185–190, 1988.

[48] Y. Xu, Y. Song, Y. Suzuki, and Z.-G. Zhang, "Mechanism of fe additive improving the activity stability of microzeolite-based mo/hzsm-5 catalyst in non-oxidative methane dehydroaromatization at 1073 k under periodic ch 4–h 2 switching modes," *Catalysis Science & Technology*, vol. 4, no. 10, pp. 3644–3656, 2014.

[49] S. Majhi and K. Pant, "Direct conversion of methane with methanol toward higher hydrocarbon over ga modified mo/h-zsm-5 catalyst," *Journal of Industrial and Engineering Chemistry*, vol. 20, no. 4, pp. 2364–2369, 2014.

[50] L. Nykanen and K. Honkala, "Selectivity in propene dehydrogenation on pt and pt3sn surfaces from first principles," *ACS Catalysis*, vol. 3, no. 12, pp. 3026–3030, 2013.

[51] X. Guo, G. Fang, G. Li, H. Ma, H. Fan, L. Yu, C. Ma, X. Wu, D. Deng, M. Wei *et al.*, "Direct, nonoxidative conversion of methane to ethylene, aromatics, and hydrogen," *Science*, vol. 344, no. 6184, pp. 616–619, 2014.

[52] Y. Xiao and A. Varma, "Highly selective nonoxidative coupling of methane over pt-bi bimetallic catalysts," *ACS Catalysis*, vol. 8, no. 4, pp. 2735–2740, 2018.

[53] E. Owen and E. Yates, "Xli. precision measurements of crystal parameters," *The London, Edinburgh, and Dublin Philosophical Magazine and Journal of Science*, vol. 15, no. 98, pp. 472–488, 1933.

[54] R. Wyckoff, "Interscience publishers, new york, new york rocksalt structure," *Crystal structures*, vol. 1, pp. 85–237, 1963.

[55] N. E. Brese and H. G. von Schnering, "Bonding trends in pyrites and a reinvestigation of the structures of pdas2, pdsb2, ptsb2 and ptbi2," *Zeitschrift für anorganische und allgemeine Chemie*, vol. 620, no. 3, pp. 393–404, 1994.

[56] P. Cucka and C. Barrett, "The crystal structure of bi and of solid solutions of pb, sn, sb and te in bi," *Acta Crystallographica*, vol. 15, no. 9, pp. 865–872, 1962.

[57] P. Weisz and C. Prater, "Interpretation of measurements in experimental catalysis," *Adv. Catal*, vol. 6, no. 143, pp. 60 390–9, 1954.

[58] D. E. Mears, "Diagnostic criteria for heat transport limitations in fixed bed reactors," *Journal of Catalysis*, vol. 20, no. 2, pp. 127–131, 1971.

[59] J. C. Slater, "Atomic radii in crystals," *The Journal of Chemical Physics*, vol. 41, no. 10, pp. 3199–3204, 1964.

[60] H. Okamoto, "The bi-pt (bismuth-platinum) system," *Journal of phase equilibria*, vol. 12, no. 2, pp. 207–210, 1991.

[61] W. Hume-Rothery and H. M. Powell, "On the theory of super-lattice structures in alloys," *Zeitschrift für Kristallographie-Crystalline Materials*, vol. 91, no. 1-6, pp. 23–47, 1935.

[62] Z. Wu, E. C. Wegener, H.-T. Tseng, J. R. Gallagher, J. W. Harris, R. E. Diaz, Y. Ren, F. H. Ribeiro, and J. T. Miller, "Pd–in intermetallic alloy nanoparticles: highly selective ethane dehydrogenation catalysts," *Catalysis Science & Technology*, vol. 6, no. 18, pp. 6965–6976, 2016.

[63] Z. Wu, B. C. Bukowski, Z. Li, C. Milligan, L. Zhou, T. Ma, Y. Wu, Y. Ren, F. H. Ribeiro, W. N. Delgass *et al.*, "Changes in catalytic and adsorptive properties of 2 nm pt3mn nanoparticles by subsurface atoms," *Journal of the American Chemical Society*, vol. 140, no. 44, pp. 14 870–14 877, 2018.

[64] C. Ye, Z. Wu, W. Liu, Y. Ren, G. Zhang, and J. T. Miller, "Structure determination of a surface tetragonal pt1sb1 phase on pt nanoparticles," *Chemistry of Materials*, vol. 30, no. 14, pp. 4503–4507, 2018.

[65] J. R. Gallagher, D. J. Childers, H. Zhao, R. E. Winans, R. J. Meyer, and J. T. Miller, "Structural evolution of an intermetallic pd–zn catalyst selective for propane dehydrogenation," *Physical Chemistry Chemical Physics*, vol. 17, no. 42, pp. 28 144–28 153, 2015.

[66] L. Deng, H. Miura, T. Shishido, S. Hosokawa, K. Teramura, and T. Tanaka, "Dehydrogenation of propane over silica-supported platinum–tin catalysts prepared by direct reduction: Effects of tin/platinum ratio and reduction temperature," *ChemCatChem*, vol. 6, no. 9, pp. 2680–2691, 2014.

[67] J. Llorca, N. Homs, J.-L. G. Fierro, J. Sales, and P. R. de la Piscina, "Platinum–tin catalysts supported on silica highly selective forn-hexane dehydrogenation," *Journal of catalysis*, vol. 166, no. 1, pp. 44–52, 1997.

[68] B. K. Vu, M. B. Song, I. Y. Ahn, Y.-W. Suh, D. J. Suh, W.-I. Kim, H.-L. Koh, Y. G. Choi, and E. W. Shin, "Propane dehydrogenation over pt–sn/rare-earth-doped al2o3: Influence of la, ce, or y on the formation and stability of pt–sn alloys," *Catalysis today*, vol. 164, no. 1, pp. 214–220, 2011.

[69] E. C. Wegener, Z. Wu, H.-T. Tseng, J. R. Gallagher, Y. Ren, R. E. Diaz, F. H. Ribeiro, and J. T. Miller, "Structure and reactivity of pt–in intermetallic alloy nanoparticles: Highly selective catalysts for ethane dehydrogenation," *Catalysis Today*, vol. 299, pp. 146–153, 2018.

[70] W. Klement Jr, A. Jayaraman, and G. Kennedy, "Phase diagrams of arsenic, antimony, and bismuth at pressures up to 70 kbars," *Physical Review*, vol. 131, no. 2, p. 632, 1963.

[71] G. L. Haller, "Metal–support interaction: Group vill," *Advances in catalysis*, p. 173, 1989.

[72] K. Tanabe, "Application of niobium oxides as catalysts," *Catalysis Today*, vol. 8, no. 1, pp. 1–11, 1990.

[73] A. Caballero, J. P. Holgado, V. M. Gonzalez-delaCruz, S. E. Habas, T. Herranz, and M. Salmeron, "In situ spectroscopic detection of smsi effect in a ni/ceo 2 system: hydrogen-induced burial and dig out of metallic nickel," *Chemical Communications*, vol. 46, no. 7, pp. 1097–1099, 2010.

[74] L. Liu, F. Zhou, L. Wang, X. Qi, F. Shi, and Y. Deng, "Low-temperature co oxidation over supported pt, pd catalysts: Particular role of feox support for oxygen supply during reactions," *Journal of Catalysis*, vol. 274, no. 1, pp. 1–10, 2010.

[75] S. Tauster, S. Fung, R. Baker, and J. Horsley, "Strong interactions in supported-metal catalysts," *Science*, vol. 211, no. 4487, pp. 1121–1125, 1981.

[76] T. Ekou, L. Ekou, A. Vicente, G. Lafaye, S. Pronier, C. Especel, and P. Marécot, "Citral hydrogenation over rh and pt catalysts supported on tio2: Influence of the preparation and activation protocols of the catalysts," *Journal of Molecular Catalysis A: Chemical*, vol. 337, no. 1-2, pp. 82–88, 2011.

[77] I. McManus, H. Daly, J. Thompson, E. Connor, C. Hardacre, S. Wilkinson, N. S. Bonab, J. Ten Dam, M. Simmons, E. H. Stitt *et al.*, "Effect of solvent on the hydrogenation of 4-phenyl-2-butanone over pt based catalysts," *Journal of Catalysis*, vol. 330, pp. 344–353, 2015.

[78] J. H. Kang, E. W. Shin, W. J. Kim, J. D. Park, and S. H. Moon, "Selective hydrogenation of acetylene on tio2-added pd catalysts," *Journal of catalysis*, vol. 208, no. 2, pp. 310–320, 2002.

[79] D. Goodman, ""catalytically active au on titania:" yet another example of a strong metal support interaction (smsi)?" *Catalysis Letters*, vol. 99, no. 1-2, pp. 1–4, 2005.

[80] M. Chen and D. Goodman, "Interaction of au with titania: the role of reduced ti," *Topics in Catalysis*, vol. 44, no. 1-2, pp. 41–47, 2007.

[81] M. Chen, Y. Cai, Z. Yan, and D. W. Goodman, "On the origin of the unique properties of supported au nanoparticles," *Journal of the American Chemical Society*, vol. 128, no. 19, pp. 6341–6346, 2006.

[82] T. Komaya, A. T. Bell, Z. Wengsieh, R. Gronsky, F. Engelke, T. S. King, and M. Pruski, "The influence of metal-support interactions on the accurate determination of ru dispersion for ru/tio2," *Journal of Catalysis*, vol. 149, no. 1, pp. 142–148, 1994.

[83] M. Lewandowski, Y.-N. Sun, Z.-H. Qin, S. Shaikhutdinov, and H.-J. Freund, "Promotional effect of metal encapsulation on reactivity of iron oxide supported pt catalysts," *Applied Catalysis A: General*, vol. 391, no. 1-2, pp. 407–410, 2011.

[84] D. R. Rainer, C. Xu, and D. W. Goodman, "Characterization and catalysis studies of small metal particles on planar model oxide supports," *Journal of Molecular Catalysis A: Chemical*, vol. 119, no. 1-3, pp. 307–325, 1997.

[85] T. B. Bolin, T. Wu, N. Schweitzer, R. Lobo-Lapidus, A. J. Kropf, H. Wang, Y. Hu, J. T. Miller, and S. M. Heald, "In situ intermediate-energy x-ray catalysis research at the advanced photon source beamline 9-bm," *Catalysis today*, vol. 205, pp. 141–147, 2013.

[86] P. Panagiotopoulou and D. I. Kondarides, "Effects of alkali additives on the physicochemical characteristics and chemisorptive properties of pt/tio2 catalysts," *Journal of Catalysis*, vol. 260, no. 1, pp. 141–149, 2008.

[87] J. Miller, A. Kropf, Y. Zha, J. Regalbuto, L. Delannoy, C. Louis, E. Bus, and J. A. van Bokhoven, "The effect of gold particle size on auau bond length and reactivity toward oxygen in supported catalysts," *Journal of Catalysis*, vol. 240, no. 2, pp. 222–234, 2006.

[88] S. Purdy, P. Ghanekar, G. M. Mitchell, A. J. Kropf, D. Y. Zemlyanov, Y. Ren, F. H. Ribeiro, W. N. Delgass, J. P. Greeley, and J. T. Miller, "The origin of electronic modification of platinum in a pt3v alloy and their consequences for propane dehydrogenation catalysis," *ACS Applied Energy Materials*, 2020.

[89] R. D. Cortright, S. A. Goddard, J. E. Rekoske, and J. Dumesic, "Kinetic study of ethylene hydrogenation," *Journal of catalysis*, vol. 127, no. 1, pp. 342–353, 1991.

[90] J. Schlatter and M. Boudart, "Hydrogenation of ethylene on supported platinum," *Journal of Catalysis*, vol. 24, no. 3, pp. 482–492, 1972.

[91] T. Dorling, M. Eastlake, and R. Moss, "The structure and activity of supported metal catalysts: Iv. ethylene hydrogenation on platinum/silica catalysts," *Journal of Catalysis*, vol. 14, no. 1, pp. 23–33, 1969.

[92] M. Bahl, S. Tsai, and Y.-W. Chung, "Auger and photoemission investigations of the platinum-srti o 3 (100) interface: Relaxation and chemical-shift effects," *Physical Review B*, vol. 21, no. 4, p. 1344, 1980.

[93] J. Ohyama, A. Yamamoto, K. Teramura, T. Shishido, and T. Tanaka, "Modification of metal nanoparticles with tio2 and metal- support interaction in photodeposition," *ACS Catalysis*, vol. 1, no. 3, pp. 187–192, 2011.

[94] A. Ruppert and T. Paryjczak, "Pt/zro2/tio2 catalysts for selective hydrogenation of crotonaldehyde: Tuning the smsi effect for optimum performance," *Applied Catalysis A: General*, vol. 320, pp. 80–90, 2007.

[95] D. E. Resasco, R. S. Weber, S. Sakellson, M. McMillan, and G. L. Haller, "X-ray absorption near-edge structure evidence for direct metal-metal bonding and electron transfer in reduced rhodium/titania catalysts," *The Journal of Physical Chemistry*, vol. 92, no. 1, pp. 189–193, 1988.

[96] S. Sakellson, M. McMillan, and G. L. Haller, "Exafs evidence for direct metal-metal bonding in reduced rhodium/titania catalysts," *The Journal of Physical Chemistry*, vol. 90, no. 9, pp. 1733–1736, 1986.

[97] E. C. Wegener, B. C. Bukowski, D. Yang, Z. Wu, A. J. Kropf, W. Delgass, J. Greeley, G. Zhang, and J. T. Miller, "Intermetallic compounds as an alternative to single-atom alloy catalysts: geometric and electronic structures from advanced x-ray spectroscopies and computational studies," *ChemCatChem*, 2020.

[98] M. Boudart, "Heterogeneous catalysis by metals," *Journal of molecular catalysis*, vol. 30, no. 1-2, pp. 27–38, 1985.

[99] J. Z. Chen, Z. Wu, X. Zhang, S. Choi, Y. Xiao, A. Varma, W. Liu, G. Zhang, and J. T. Miller, "Identification of the structure of the bi promoted pt nonoxidative coupling of methane catalyst: a nanoscale pt 3 bi intermetallic alloy," *Catalysis Science & Technology*, vol. 9, no. 6, pp. 1349–1356, 2019.

[100] J. Bracey and R. Burch, "Enhanced activity of pdtio2 catalysts for the coh2 reaction in the absence of strong metal-support interactions (smsi)," *Journal of Catalysis*, vol. 86, no. 2, pp. 384–391, 1984.

[101] J. C. Matsubu, S. Zhang, L. DeRita, N. S. Marinkovic, J. G. Chen, G. W. Graham, X. Pan, and P. Christopher, "Adsorbate-mediated strong metal–support interactions in oxide-supported rh catalysts," *Nature chemistry*, vol. 9, no. 2, pp. 120–127, 2017.

[102] P. Christopher and S. Linic, "Engineering selectivity in heterogeneous catalysis: Ag nanowires as selective ethylene epoxidation catalysts," *Journal of the American Chemical Society*, vol. 130, no. 34, pp. 11 264–11 265, 2008.

[103] F. Calle-Vallejo, J. Tymoczko, V. Colic, Q. H. Vu, M. D. Pohl, K. Morgenstern, D. Loffreda, P. Sautet, W. Schuhmann, and A. S. Bandarenka, "Finding optimal surface sites on heterogeneous catalysts by counting nearest neighbors," *Science*, vol. 350, no. 6257, pp. 185–189, 2015.

[104] A. Holewinski, J.-C. Idrobo, and S. Linic, "High-performance ag–co alloy catalysts for electrochemical oxygen reduction," *Nature chemistry*, vol. 6, no. 9, p. 828, 2014.

[105] S. Tauster, S. Fung, and R. L. Garten, "Strong metal-support interactions. group 8 noble metals supported on titanium dioxide," *Journal of the American Chemical Society*, vol. 100, no. 1, pp. 170–175, 1978.

[106] A. S. Wörz, U. Heiz, F. Cinquini, and G. Pacchioni, "Charging of au atoms on tio2 thin films from co vibrational spectroscopy and dft calculations," *The Journal of Physical Chemistry B*, vol. 109, no. 39, pp. 18 418–18 426, 2005.

[107] C. Deleitenburg and A. Trovarelli, "Metal-support interactions in rh/ceo2, rh/tio2, and rh/nb2o5 catalysts as inferred from co2 methanation activity," *Journal of Catalysis*, vol. 156, no. 1, pp. 171–174, 1995.

[108] H. Xiong, S. Lin, J. Goetze, P. Pletcher, H. Guo, L. Kovarik, K. Artyushkova, B. M. Weckhuysen, and A. K. Datye, "Thermally stable and regenerable platinum–tin clusters for propane dehydrogenation prepared by atom trapping on ceria," *Angewandte Chemie International Edition*, vol. 56, no. 31, pp. 8986–8991, 2017.

[109] D. Kunwar, S. Zhou, A. DeLaRiva, E. J. Peterson, H. Xiong, X. I. Pereira-Hernández, S. C. Purdy, R. ter Veen, H. H. Brongersma, J. T. Miller *et al.*, "Stabilizing high metal loadings of thermally stable platinum single atoms on an industrial catalyst support," *ACS Catalysis*, vol. 9, no. 5, pp. 3978–3990, 2019.

[110] S. Penner, G. Rupprechter, H. Sauer, D. S. Su, R. Tessadri, R. Podloucky, R. Schlögl, and K. Hayek, "Pt/ceria thin film model catalysts after high-temperature reduction: a (hr) tem study," *Vacuum*, vol. 71, no. 1-2, pp. 71–76, 2003.

[111] S. Bernal, J. Calvino, M. Cauqui, J. Gatica, C. Larese, J. P. Omil, and J. Pintado, "Some recent results on metal/support interaction effects in nm/ceo2 (nm: noble metal) catalysts," *Catalysis Today*, vol. 50, no. 2, pp. 175–206, 1999.

[112] F. H. RIBEIRO, A. E. SCHACH VON WITTENAU, C. H. BARTHOLOMEW, and G. A. SOMORJAI, "Reproducibility of turnover rates in heterogeneous metal catalysis: compilation of data and guidelines for data analysis," *Catalysis Reviews*, vol. 39, no. 1-2, pp. 49–76, 1997.

[113] F. Zaera and G. Somorjai, "Hydrogenation of ethylene over platinum (111) single-crystal surfaces," *Journal of the American Chemical Society*, vol. 106, no. 8, pp. 2288–2293, 1984.

[114] S. Bernal, J. Calvino, M. Cauqui, G. Cifredo, A. Jobacho, and J. Rodriguez-Izquierdo, "Metal-support interaction phenomena in rhodium/ceria and rhodium/titania catalysts: Comparative study by high-resolution transmission electron spectroscopy," *Applied Catalysis A: General*, vol. 99, no. 1, pp. 1–8, 1993.

[115] J. M. Cíes, E. del Río, M. López-Haro, J. J. Delgado, G. Blanco, S. Collins, J. J. Calvino, and S. Bernal, "Fully reversible metal deactivation effects in gold/ceria–zirconia catalysts: Role of the redox state of the support," *Angewandte Chemie International Edition*, vol. 49, no. 50, pp. 9744–9748, 2010.

[116] D. Kalakkad, A. K. Datye, and H. Robota, "Interaction of platinum and ceria probed by transmission electron microscopy and catalytic reactivity," *Applied Catalysis B: Environmental*, vol. 1, no. 3, pp. 191–219, 1992.

[117] J. Cunningham, S. O'Brien, J. Sanz, J. Rojo, J. Soria, and J. Fierro, "Exceptional susceptibility of ceria-supported rhodium catalyst to inhibitory smsi effects including acetone hydrogenation," *Journal of molecular catalysis*, vol. 57, no. 3, pp. 379–396, 1990.

[118] L. Liotta, A. Longo, A. Macaluso, A. Martorana, G. Pantaleo, A. Venezia, and G. Deganello, "Influence of the smsi effect on the catalytic activity of a pt (1%)/ce0. 6zr0. 4o2 catalyst: Saxs, xrd, xps and tpr investigations," *Applied Catalysis B: Environmental*, vol. 48, no. 2, pp. 133–149, 2004.

[119] A. Borodziński and M. Bonarowska, "Relation between crystallite size and dispersion on supported metal catalysts," *Langmuir*, vol. 13, no. 21, pp. 5613–5620, 1997.

[120] F. Yang, N. J. Libretto, M. R. Komarneni, W. Zhou, J. T. Miller, X. Zhu, and D. E. Resasco, "Enhancement of m-cresol hydrodeoxygenation selectivity on ni catalysts by surface decoration of moo x species," *ACS Catalysis*, vol. 9, no. 9, pp. 7791–7800, 2019.

[121] Y. Zhang, Y. Zhou, A. Qiu, Y. Wang, Y. Xu, and P. Wu, "Propane dehydrogenation on ptsn/zsm-5 catalyst: Effect of tin as a promoter," *Catalysis Communications*, vol. 7, no. 11, pp. 860–866, 2006.

[122] H. Zhu, D. H. Anjum, Q. Wang, E. Abou-Hamad, L. Emsley, H. Dong, P. Laveille, L. Li, A. K. Samal, and J.-M. Basset, "Sn surface-enriched pt–sn bimetallic nanoparticles as a selective and stable catalyst for propane dehydrogenation," *Journal of catalysis*, vol. 320, pp. 52–62, 2014.

[123] S. T. Oyama, T. Gott, H. Zhao, and Y.-K. Lee, "Transition metal phosphide hydroprocessing catalysts: A review," *Catalysis Today*, vol. 143, no. 1-2, pp. 94–107, 2009.

[124] R. Prins and M. E. Bussell, "Metal phosphides: preparation, characterization and catalytic reactivity," *Catalysis letters*, vol. 142, no. 12, pp. 1413–1436, 2012.

[125] Y. Pei, Y. Cheng, J. Chen, W. Smith, P. Dong, P. M. Ajayan, M. Ye, and J. Shen, "Recent developments of transition metal phosphides as catalysts in the energy conversion field," *Journal of materials chemistry A*, vol. 6, no. 46, pp. 23 220–23 243, 2018.

[126] S. Tan, B. Hu, W.-G. Kim, S. H. Pang, J. S. Moore, Y. Liu, R. S. Dixit, J. G. Pendergast, D. S. Sholl, S. Nair *et al.*, "Propane dehydrogenation over alumina-supported iron/phosphorus catalysts: Structural evolution of iron species leading to high activity and propylene selectivity," *ACS Catalysis*, vol. 6, no. 9, pp. 5673–5683, 2016.

[127] Y. Kanda, C. Temma, K. Nakata, T. Kobayashi, M. Sugioka, and Y. Uemichi, "Preparation and performance of noble metal phosphides supported on silica as new hydrodesulfurization catalysts," *Applied Catalysis A: General*, vol. 386, no. 1-2, pp. 171–178, 2010.

[128] Y. Kanda, K. Kawanishi, T. Tsujino, A. M. Al-Otaibi, and Y. Uemichi, "Catalytic activities of noble metal phosphides for hydrogenation and hydrodesulfurization reactions," *Catalysts*, vol. 8, no. 4, p. 160, 2018.

[129] R. H. Bowker, M. C. Smith, B. A. Carrillo, and M. E. Bussell, "Synthesis and hydrodesulfurization properties of noble metal phosphides: ruthenium and palladium," *Topics in Catalysis*, vol. 55, no. 14-15, pp. 999–1009, 2012.

[130] Q. Guan, C. Sun, R. Li, and W. Li, "The synthesis and investigation of ruthenium phosphide catalysts," *Catalysis Communications*, vol. 14, no. 1, pp. 114–117, 2011.

[131] K. Liu, C. Zhang, Y. Sun, G. Zhang, X. Shen, F. Zou, H. Zhang, Z. Wu, E. C. Wegener, C. J. Taubert *et al.*, "High-performance transition metal phosphide alloy catalyst for oxygen evolution reaction," *ACS nano*, vol. 12, no. 1, pp. 158–167, 2018.

[132] F. Hu, H. Wang, Y. Zhang, X. Shen, G. Zhang, Y. Pan, J. T. Miller, K. Wang, S. Zhu, X. Yang *et al.*, "Designing highly efficient and long-term durable electrocatalyst for oxygen evolution by coupling b and p into amorphous porous nife-based material," *Small*, vol. 15, no. 28, p. 1901020, 2019.

[133] S. Suzuki, Y. Ohbu, T. Mizukami, Y. Takamori, M. Morishima, H. Daimon, and M. Hiratani, "Platinum–phosphorus nanoparticles on carbon supports for oxygen-reduction catalysts," *Journal of The Electrochemical Society*, vol. 156, no. 1, pp. B27–B31, 2009.

[134] L. Zhang, M. Wei, S. Wang, Z. Li, L.-X. Ding, and H. Wang, "Highly stable ptp alloy nanotube arrays as a catalyst for the oxygen reduction reaction in acidic medium," *Chemical science*, vol. 6, no. 5, pp. 3211–3216, 2015.

[135] Y. Ma, H. Wang, H. Li, J. Key, S. Ji, and R. Wang, "Synthesis of ultrafine amorphous ptp nanoparticles and the effect of ptp crystallinity on methanol oxidation," *RSC advances*, vol. 4, no. 40, pp. 20 722–20 728, 2014.

[136] B. Ravel and M. Newville, "Athena, artemis, hephaestus: data analysis for x-ray absorption spectroscopy using ifeffit," *Journal of synchrotron radiation*, vol. 12, no. 4, pp. 537–541, 2005.

[137] A. Hammersley, S. Svensson, M. Hanfland, A. Fitch, and D. Hausermann, "Two-dimensional detector software: from real detector to idealised image or two-theta scan," *International Journal of High Pressure Research*, vol. 14, no. 4-6, pp. 235–248, 1996.

[138] L. Lutterotti, S. Matthies, H.-R. Wenk, A. Schultz, and J. Richardson Jr, "Combined texture and structure analysis of deformed limestone from time-of-flight neutron diffraction spectra," *Journal of Applied Physics*, vol. 81, no. 2, pp. 594–600, 1997.

[139] S. C. Fung, "Xps studies of strong metal-support interactions (smsi)-pt/tio/sub 2," *J. Catal.;(United States)*, vol. 76, no. 1, 1982.

[140] K. Ding, A. Gulec, A. M. Johnson, N. M. Schweitzer, G. D. Stucky, L. D. Marks, and P. C. Stair, "Identification of active sites in co oxidation and water-gas shift over supported pt catalysts," *science*, vol. 350, no. 6257, pp. 189–192, 2015.

[141] P. Bazin, O. Saur, J. Lavalley, M. Daturi, and G. Blanchard, "Ft-ir study of co adsorption on pt/ceo 2: characterisation and structural rearrangement of small pt particles," *Physical Chemistry Chemical Physics*, vol. 7, no. 1, pp. 187–194, 2005.

[142] P. Hollins, "The influence of surface defects on the infrared spectra of adsorbed species," *Surface Science Reports*, vol. 16, no. 2, pp. 51–94, 1992.

[143] J. T. Miller, M. Schreier, A. J. Kropf, and J. R. Regalbuto, "A fundamental study of platinum tetraammine impregnation of silica: 2. the effect of method of preparation, loading, and calcination temperature on (reduced) particle size," *Journal of Catalysis*, vol. 225, no. 1, pp. 203–212, 2004.

VITA

VITA

Johnny Zhu Chen was born to Xiaobing Zhu and Chingching Chen Chou in 1995. He grew up in Madrid, Spain. He went to China to continue his studies when he was 10. In 2012, he finished high school and began his study on Chemical Engineering in Tsinghua. He joined the lab of Dr. Wei Du as an undergraduate researcher in 2014 and published 2 papers in the group. In the summer of 2014, he traveled oversea and worked as a research intern at Johns Hopkins University under the advisory of Dr. Michael J. Betenbaugh. Back to Tsinghua, Johnny finished his undergraduate thesis. After graduating from Tsinghua University, he went to graduate school in August 2016 and joined Davidson School School of Chemical Engineering at Purdue University, West Lafayette, IN. He worked under the guidance of Dr. Jeffrey T. Miller and did dissertation research on intermetallic and strong metal-support nanoparticle catalysts for shale gas conversion. He applied synchrotron X-ray techniques to interrogate the catalysts structure, from which he proposed rules controlling the materials formation and several structure-function relations. He graduated with a Ph.D. degree in chemical engineering in 2020.

PUBLICATIONS

J. Zhu Chen, A. Talpade, G. Canning, J. Gao, P. R. Probus, F. H. Ribeiro, A. K. Datye, and J. T. Miller. Strong Metal-Support Interaction (SMSI) of Pt/CeO2 under extreme conditions. *submitted to Catalysis Today*

J. Kou, J. Zhu Chen, J. Gao, W. Liu, J. Zhu, X. Zhang, A. J. Kropf, D. Zemlyanov, G. Zhang, L. Guo and J. T. miller. Tuning geometric and electronic structure of platinum catalysts for propane dehydrogenation by phosphorous promotion. *submitted to ACS Catalysis*

R. Ma, T. Yang, J. Gao, J. Kou, J. Zhu Chen, Y. He, J. T. Miller, and D. Li, Composition tuning of Ru-based phosphide for enhanced propane selective dehydrogenation. *submitted to ACS Catalysis*

J. Zhu Chen, J. Gao, P. R. Probus, W. Liu, X. Wu, E. C. Wegener, A. J. Kropf, D. Zemlyanov, G. Zhang, X. Yang, and J. T. Miller. The effect of strong metal-support interaction (SMSI) on Pt-Ti/SiO2 and Pt-Nb/SiO2 catalysts for propane dehydrogenation. *submitted to Catalysis Science and Technology*

Z. Li, Y. Xiao, Z. Wu, P. He, J. Zhu Chen, T. Ma, L. Zhou, J. T. Miller, A. Varma, and Y. Wu. Direct methane activation by platinum nanolayers on two-dimensional metal carbide. *submitted to Science*

Y. Cui, J. Zhu Chen, B. Peng, L. Kovarik, A. Devaraj, Z. Li, T. Ma, Y. Wang, J. Szanyi, J. T. Miller, Yong Wang, Feng Gao. Onset of high methane combustion rates over supported palladium catalysts: from isolated Pd cations to PdO nanoparticles. *submitted to Nature Catalysis*

J. Zhu Chen, Z. Wu, X. Zhang, S. Choi, Y. Xiao, A. Varma, W. Liu, G. Zhang and J. T. Miller. Identification of the structure of the Bi promoted Pt non-oxidative coupling of methane catalyst: a nanoscale Pt3Bi intermetallic alloy. *Catalysis Science and Technology*, 2019, 9, 1349-1356.

G. Zhang, C. Ye, W. Liu, X. Zhang, D. Su, X. Yang, J. Zhu Chen, Z. Wu, J. T. Miller. Diffusion-limited formation of nonequilibrium intermetallic nanophase for selective dehydrogenation. *Nano Letters*, 2019, 19, 4380-4383.